Radio beam steering in indoor fibre-wireless networks

Radio Beam Steering in Indoor Fibre-Wireless Networks

PROEFSCHRIFT

ter verkrijging van de graad van doctor aan de
Technische Universiteit Eindhoven, op gezag van de
rector magnificus, prof.dr.ir. C.J. van Duijn, voor een
commissie aangewezen door het College voor
Promoties in het openbaar te verdedigen
op dinsdag 21 april 2015 om 14.00 uur

door

Zizheng Cao

geboren te Leiyang, China

Dit proefschrift is goedgekeurd door de promotoren en de samenstelling van de promotiecommissie is als volgt:

voorzitter:	prof.dr.ir. A.C.P.M. Backx
1e promotor:	prof.ir. A.M.J. Koonen
copromotor:	dr.ir. E. Tangdiongga
leden:	prof. H. Wu (Peking University)
	prof.dr. J. Capmany (Universitat Politècnica de València)
	prof.dr.ir. A.B. Smolders
	prof.dr.ir. M.K. Smit
	dr. N. Gomes (University of Kent)

The research reported in this thesis was performed in the Dutch project Smart Optical Wireless Indoor Communication Infrastructure (SOWICI), which was part of the Smart Energy Systems programme funded by the Dutch Organization for Scientific Research (NWO).

A catalogue record is available from the Eindhoven University of Technology Library.

Title: Radio Beam Steering in Indoor Fibre-Wireless Networks

Author: Zizheng Cao
Eindhoven University of Technology, 2015
ISBN: 978-94-6259-664-1
NUR 959

Keywords: Optical fibre communication / Fiber-Wireless networks / Radio-over-Fiber / Optical beam steering

Communication links us.

Qiaoqi (Sharon) Zhang (2015)

Summary

Radio Beam Steering in Indoor Fibre-Wireless Networks

The research reported in this thesis was done in the Dutch project Smart Optical Wireless Indoor Communication Infrastructure (SOWICI), which was part of the Smart Energy Systems program funded by the Dutch Organization for Scientific Research (NWO). The data volumes transported in indoor networks are growing fast. In particular for wireless connectivity, the data volumes may exceed those on the home access line, due to heavy home-internal traffic. SOWICI's goal is to conceive a novel indoor broadband communication infrastructure which provides communication services in the most reliable, cost-effective and energy-efficient way. The infrastructure proposed is a heterogeneous network consisting of a fibre backbone network flexibly feeding many radio antenna stations in the building. Within each room of the building, there are one or more radio antenna stations, which convert the optical signal into a radio wave (radio-over-fibre technique) covering the room. Such a pico-cell approach offers a much higher throughput and lower energy consumption than the conventional macro-cell approach where the whole building is covered by a single (or just a few) radio stations. To go even beyond this improvement, in the SOWICI project radio beam steering has been investigated. Within every room multiple radio pencil beams will be active, which each can be steered dynamically upon demand in order to only cover a selected part of the room. The beam steering has to be aided by techniques for localizing the users' devices. By this dynamic beam steering, the energy efficiency and data throughput can be improved even further. The research described in the thesis aims to provide solutions for a broadband as well as energy-efficient hybrid wireless indoor network, and addresses four interrelated aspects:

1) **Gateway functions for indoor fibre-wireless networks.** The gateway based on a semiconductor optical amplifier is proposed to interconnect the access network with the indoor network, which simultaneously provides remote

(radio frequency) up-conversion and dynamic capacity allocation (indoor exchange function). Another advanced gateway with up-conversion and indoor exchange based on heterodyne with a free-run laser is proposed and experimentally studied. An advanced DSP algorithm to eliminate the laser phase noise is proposed and studied as well.

2) **Optical delay techniques for radio beam steering.** Optical true time delay techniques for squint-free broadband beam steering by means of phased array antennas are studied. A new cyclic additional optical true-time-delay (CAO-TTD) scheme is proposed to providing simultaneous beam steering and spectral filtering. Further, a novel integrated step-wise wavelength-tunable true-time-delay scheme based on AWG feedback loops are proposed. Designed with interleaved row-and column-wise arranged TTD elements, this device enables optically-controlled 2-D radio beam steering. Two photonic integrated circuits based on 1-D version are realized on both silicon and indium phosphide platforms and have been successfully been characterized.

3) **Optical localization of radio devices.** A novel parallel optical phase detector based on parallel MZM is proposed and experimentally verified for measuring the angle-of-arrival of radio signals. A further simplified scheme based on a dual-drive MZM is proposed and experimentally investigated.

4) **Control channel**. Simple synchronized control signaling delivery schemes for indoor fibre-wireless networks are 1) proposed with low frequency detection of high speed baseband data from optical access networks; and 2) proposed with baseband detection of 60GHz optical mm-wave signal by a low bandwidth (~500MHz) photodiode. Experimental results verified both schemes.

5) **System demonstrations**. Optical radio beam-steered radio-over-fibre systems using optical true time delays are proposed for squint-free broadband beam steering based on phased array antennas. The proof-of-concept ORBS-RoF systems based on bulk optical tunable delay lines are demonstrated. Further a 40GHz ORBS-RoF system is studied experimentally based on an integrated optical tunable delay line.

Contents

Chapter 1 Introduction

The research reported in this thesis was done in the Dutch project Smart Optical Wireless Indoor Communication Infrastructure (SOWICI), which was part of the Smart Energy Systems program funded by the Dutch Organization for Scientific Research (NWO) since 2011. The introduction is mainly extended from the proposal of SOWICI with four years Ph. D considerations through project implementations. After four years, I am surprised to find that most features about future in-home networks are predicted well in our project proposal which may allow a high application value of all scientific contributions of this thesis. Now let us start to find out what the proposal predicted and what are our solutions!

1.1 Evolution of wireless services

Telecom techniques provide unsurpassed benefits to the development of society ranging from human well-being to new efficient industrial production. As the most flexible telecom approach, wireless communication systems encountered a 1000-fold capacity boosting from 2000 to 2010 [1] and are expected to increase another 1000-fold in the next decade. Currently the capacity increase is driven by bandwidth-hungry media services such as full high definition (Full HD) video, which is also heavily shared over social media websites (e.g., Facebook and Youtube). As indicated in [2], about 79% of the IP traffic will be used for video content delivery in 2018, up from 66% in 2013. In this thesis, we define the 'wireless devices' as the devices connected via wireless local area networks (WLAN) such as WiFi, and the 'mobile devices' as the ones connected via cellular networks. However, such definition is not strict since currently most 'mobile devices' can also be connected via WLAN. Driven by the explosive emerging of mobile devices such like smart phones and tablets, the IP traffic of wireless and mobile devices will exceed traffic of wired devices in 2018. In 2013, wireless and mobile devices accounted for 44% of the IP traffic.

A series of ongoing research is being carried out to boost the current wireless capacity in order to meet future demand. We will summarize the major trends in wireless cellular networks and wireless local area networks.

1.1.1 The 5G wireless cellular networks

During the past several years, both industry and academic communities have already made huge investigations for the fourth generation communication technique, which is also referred as Long Term Evolution (LTE) to support higher capacity to terminal users. Usually, the increased capacity is achieved by implementing smaller cells with more base stations, improving spectral efficiency, and spectrum acquisition. Although there is no incumbent 5G standards made by any standardization body yet, there is a widely accepted vision that the peak data rate of 5G should be tens of giga-bits per second and provide a few gigabits per second connection to terminal users. To search for innovative solutions to boost the capacity, many activities have started globally. In 2013, the European Commission started an investigation of €50 million for 5G research in multiple projects. Soon thereafter the Chinese government initiated the IMT-2020 Promotion Group and later the Korean government started the 5G Forum in May 2013. There are many techniques proposed for 5G. Some of the LTE enhancements are investigated, including heterogeneous networks (HetNets), small-cell networks, advanced multiple-input multiple-output (MIMO) techniques including massive MIMO and beam-forming/-steering, coordinated multipoint (CoMP), and carrier aggregation (CA). Among these techniques, the methods to increase capacity by multiple spatial channels are attractive, including small-cell networks and massive MIMO. Another effective solution is to use the large chunks of underutilized spectrum at very high frequencies such as the millimeter-wave (mm-wave) [3, 4]. Finally, radio beam steering is also considered as a key energy-efficient method to boost spatial capacity.

1.1.2 The upcoming wireless local area networks

In the last decade, the popular Wi-Fi family based on the IEEE 802.11 standards has become huge success in the world. Today, a lot of consumer electronic devices and most mobile devices support Wi-Fi due to its mobility, ease of use and low cost. The IEEE 802.11 standards exploit the 2.4 or the 5 GHz unlicensed band for local area networks. However, as indicated in Table 1, the unlicensed band is usually less than 500 MHz.

Due to the flourishing usage of Wi-Fi, the unlicensed bands are heavily saturated, and even fully occupied in public places like shopping mall, schools, and airports. To make good use of the spectrum resource, in IEEE 802.11n, the

Table 1 The two unlicensed frequency bands used by the Wi-Fi systems.

Band	Frequency (GHz)	Band name
2.4	2.400-2.4835	Industrial Scientific Medical (ISM)
5	5.150-5.350 and 5.470-5.725	Unlicensed National Information Infrastructure (U-NII)

system will optimize the allocation of resources depending on the nearby operating Wi-Fi systems to efficiently reduce the interferences. To further improve the capacity of the Wi-Fi systems, given the limited spectrum, the spatial channel capacity is extended based on massive MIMO and beam steering, which can find cues in the latest Wi-Fi standard IEEE 802.11ac. This is a new member of the Wi-Fi family which can provide very high throughput (VHT) wireless local area networks (WLANs) on the 5 GHz band. Its standardization began in 2011 and has been ratified in January 2014. In IEEE 802.11ac, up to eight antennas can be utilized to boost the capacity to at least 1Gb/s throughput of a multi-station WLAN. With high-density modulation (e.g. 256QAM), its capacity can even go up to 6.7 Gb/s. However, due to the bandwidth limitation, such capacity seems to be the ceiling of practical applications. To boost the next generation WLAN, mm-wave and beam steering techniques are proposed in standard bodies in order to use the huge chunk of spectrum at 60 GHz ISM band.

These days, due to the tremendous unlicensed bandwidth (>7 GHz), the 60GHz band receives much attention from academic community and industrial community. Currently there are two kinds of 60 GHz standards. The early one, focusing on WPAN applications (especially for wireless connection for high definition video), is presented by the IEEE 802.15.3c and ECMA-387 standards; both are heavily linked to the WirelessHD consortium. The latter one is proposed most recently for both WPAN and WLAN applications, which can be considered as the continuation of existing Wi-Fi standards. A representative example is the IEEE 802.11ad standard, which is initially from the WiGig consortium and merged into the Wi-Fi Alliance. The IEEE 802.11ad standard aims to provide the terminal user the similar experience of the IEEE 802.11 family and also the flexibility of network management, but with more than multi-Gb/s capacity.

1.1.3 Key enabling technologies for upcoming wireless networks

In the following, we will discuss in detail the concrete techniques we mentioned in both 5G wireless cellular networks and up-coming wireless local area networks. The implementation challenges regarding to these techniques will be discussed as well.

Small cells

For wireless local area networks, their cell radiuses are usually small due to the limited radiation power in the unlicensed band. For the coming IEEE802.11ad, due to the weak wall penetration of 60 GHz mm-wave, the small-cell concept is natively adopted. For the wireless cellular networks, 4G already introduced small-cell networks and it seems the small cells are dominant for 5G with coordinated macro-cells. The energy saving can be benefited by small cells as indicated in[5]. These days rooftop base stations are used for 3G networks. Due to the small size of LTE cells, more and more rooftop spaces have been occupied. However the rooftop base stations can not satisfy the bandwidth hungry customers, especially in some urban areas such as an airport. For 3G, operators can install base stations on rooftops due to its relatively large cell size. For 4G (LTE), the cells are becoming smaller; therefore more than ten times more base stations are needed to cover the same area. For the coming 5G, more and more network architectures based on small cells are proposed and discussed [4, 6] to find a suitable solution to combine small-cells and macro-cells. To accelerate the deployment of new small cells, the FCC (Federal Communications Commission) voted to approve new rules for distributed antenna systems and other network equipment in October 2014. The FCC approved amendments to the federal environmental review process to make it easier to deploy small cells as well as collocated equipment. More and more evidence is given indicating that small-cell networks are a powerful technique for future wireless networks. However, a major challenge for small cells is capital expenditure (CAPEX) and operating expense (OPEX) regarding the huge number of new emerging small-cell base stations.

Advanced MIMO techniques

Recently massive MIMO and its special case beam-steering (-forming) techniques are proposed frequently for their ability to focus radio signals into smaller patches of space with resulting huge improvements of capacity and efficiency of radiated power. In this thesis, the term 'massive MIMO' refers to a general MIMO architecture which can be configured to different cases by precoding. The beam-steering (-forming) can be viewed as special case of massive MIMO, with simple phase/amplitude precoding and the collocated phase antenna array with short separations (half-wavelength) between each element antennas.

Massive MIMO is a form of multiuser MIMO in which the number of antennas at the base station is much larger than the one of devices per signaling resource. In particular, the number of antennas is supposed to be ten times larger than the total number of data streams connected to terminal users. In this MIMO configuration, the beam-forming gains become significant with improved signal focusing and at the same time more terminals can be connected via separated channels [7]. The larger number of base station antennas introduces another advantage of massive MIMO, namely that the channels of different devices are quasi-orthogonal and very simple spatial multiplexing/de-multiplexing procedures can provide quasi-optimal performance. Different from the traditional MIMO, massive MIMO brings totally new problems as indicated in [7]: "...the challenge of making many low-cost low-precision components that work effectively together, acquisition and synchronization for newly joined terminals, the exploitation of extra degrees of freedom provided by the excess of service antennas, reducing internal power consumption to achieve total energy efficiency reductions, and finding new deployment scenarios."

As a simple and strained case of massive MIMO, beam-steering(-forming) is a technique to focus and steer the radio signal beam (or signal power) to the desired directions. For beam-steering and -forming, phased array antennas (PAAs) are widely considered as the best candidate for microwave beam-steering due to their fast steering and compactness. Apart from other precoding methods, the beam-steering/-forming is based on phase/amplitude precoding without any complex algebra processing. The idea behind is, by control of the phases/amplitudes of transmitted radio signals from the antenna array, to allow constructive combination at desired directions and destructive ones at other directions. Given N element of a PAA, the antenna gain and received signal-to-noise ratio (SNR) improvement can be achieved by a factor of N. The focusing of transmitted and/or received signal in a desired direction can largely compensate the unfavorable path loss, which makes it a key technique for cellular networks at high-frequency bands. The small wavelengths of high frequencies facilitate the compactness of a large-size phased antenna array with large array gains as the PAA elements are separated at less than half the wavelength of the radio signal. Recently, a beam-steering/-forming communication system with 8-by-4 phase antenna array at 28GHz mm-wave band is demonstrated by Samsung, which exhibits its powerful ability to largely overcome the path loss of mm-wave propagation [4]. The operational bandwidth of a conventional PAA is limited. Specifically, a severe limitation is often caused by the use of phase shifters to steer the beam, which results in beam deformations ("squint") in the measured antenna pattern.

Mm-wave techniques

Mm-wave band is defined from 30 GHz to 300 GHz, which can provide more than 100 GHz available bandwidth. Historically, because of the relatively high propagation loss and expensive components, the mm-wave bands are mostly used for outdoor point-to-point backhaul links. Very recently, the wireless communication community started to pay attention to the millimeter wavelength spectrum [4, 8]. The idea behind this is to take advantage of the huge and unexploited bandwidth to fulfill the hungry capacity appetite of future wireless networks. It can be used for mm-wave small cells, broadband wireless local area networks broadband access, low-cost mm-wave mobile backhauls, uncompressed high-definition video delivery, and wireless access to the cloud. For wireless local area networks, the coverage is natively limited to the room-size cells due to its application scenario. To practically utilize this undeveloped spectrum for future wireless cellular networks, [4] experimentally verified the mm-wave (28 GHz) can provide large enough coverage and support for mobility even in non-line-of-sight (NLoS) environments. It further reveals that at both 28 GHz and 38 GHz bands the key parameters such as the path loss exponent, are comparable to those of typical cellular frequency bands with phased array antennas used to produce beam-forming gains at either transmitter and receiver sides. Currently the CMOS platform can already operate well in mm-wave bands, and high-gain, steerable antennas at mobile and base stations, strengthen viability of mm-wave wireless communications [9]. For mm-wave wireless networks, a major challenge is how to efficiently manage the huge number of cells.

1.2 Future indoor/-building networks

Indoor networks are likely to evolve to provide mainly wireless delivery of services, in particular high-throughput wireless services. We will first discuss the role of future indoor networks and their significance in context of existing and coming wireless services (WLAN and 5G) in 1.2.1. Then the current status and challenges for next-generation indoor networks are discussed in 1.2.2. Later, we evaluate the opportunities of fibre-wireless system for future indoor/-building networks.

1.2.1 The role of indoor/-building networks

Indoor networks are expected to provide connections to the access network (e.g. fibre to the home) for services like telephony, internet, and cable TV; and also to provide internal connections for services like wireless LAN, wireless high definition video, and blue tooth. Currently home networks are formed with different network technologies, which are each intentionally designed for specific communication services. Coaxial cable networks were used to connect television sets, twisted-pair copper lines to connect telephone sets, and Cat-5 twisted pair cables to link desktop PCs and servers. The wireless LAN of famous IEEE802.11 family are so popular as they serve laptop computers, tablets, and smartphones with dynamic flexibility.

Among these existing services, the wired services conveyed over copper pairs (1000Base-T), powerline (IEEE 1901 Broadband Powerline standard), phoneline (ITU-T G.hn) and coaxial cables (MoCA) are usually with up to 1.5Gb/s physical layer throughputs announced in their standards. Depending on the medium (copper pair, powerline...), their practical throughputs are usually less than the maximum speeds (1.5 Gb/s). It is difficult to increase the throughput if the legacy narrow-band medium like a copper pair is not replaced by its new counterparts. It is clear that the traditional wired services based on the legacy medium meet the challenge for scalable bandwidth. Another consideration from the terminal users view is: the wireless links are usually preferred links for services delivery because of their flexibility and convenience. As we discussed in section 1.1.2, the WLAN trend is moving from current 300 Mb/s (802.11n) bitrate up to more than 1Gb/s bitrate in 802.11ad, and even 7 Gb/s in 802.11ac. The very successful prevalence of WLAN introduces very comfortable user experiences to terminals and thus it is seemingly impossible to return customers back to wired terminal devices with low bit rates. Thus here our discussions are mainly focusing on wireless services.

Indoor/in-building networks are expected to play a significant role for communications since the major data traffic volume are delivered in the indoor environment. According to the evaluation conducted by Mischa Dohler [10] about 80% users' data is delivered wirelessly in the office or at home, and thus an efficient indoor network could provide the main traffic volume to terminal users with good user experience. Currently, such data traffic volume is partially conveyed by an indoor network by means of wired access networks plus wireless local area networks. And the other part is conveyed by wireless cellular networks. However, in the context of coming 5G, it is visible that the indoor/-building networks should provide small cells in the high density area for 5G as we discussed in 1.2.3.

We believe that future indoor networks are expected to serve as a key platform for future communications, especially for wireless communications. Their success depends on whether the multiple services are compatible within it.

1.2.2 The opportunities and challenges of indoor networks

The current indoor/-building networks are not fully developed or standardized for wireless services. There are several challenges to overcome before its successful deployment.

• *Challenge-1: High-speed access interface versus low-speed indoor networks*

The fast increased data traffic is driven by increasing bandwidth-hungry applications such as video streaming. On the other hand, the optical access networks in terms of fibre-to-the-home (FTTH) largely extend the bandwidth provision up to the door-step. Thus a high-speed indoor network to provide the equivalent or higher throughput is demanded. Another consideration is that the bandwidth requirement for the internal data exchange of an indoor network already exceeds the speed of the FTTH access line in order to transfer data between the terminal users and its servers. For instance, a Wireless HD link requires an up to 7Gb/s link to stream an uncompressed HD movie. Thus an inherent broadband link medium is a key factor to break bottlenecks between high-speed interfaces from access networks and indoor devices.

• *Challenge-2: One-time-off construction versus multiple upcoming services*

Inside an indoor network, many different kinds of services (IP-based and non-IP based), in different frequency bands constitute the total data traffic. For wired services, the data traffic not only consists of IP data over copper pair cables but also other signals like RF signals for broadcast TV over coaxial cables and specific formats such as HDMI signals over specific cables. For wireless signals, the frequency bands of 2.4 GHz, 5 GHz, 60 GHz, and even future 28/38 GHz are operating simultaneously. The householders (owners of indoor networks) usually prefer one-time-off construction of indoor networks for the sake of convenience. Subsequently, an inherent broadband future-proof system is required to transport all incumbent services and upcoming services. It is important that such system should fully support the upcoming core wireless techniques.

• *Challenge-3: low-cost architecture versus multiple distributed access points*

One inherent feature of indoor networks is that many access points are required due to the spatial isolation induced by rooms and walls. This is a significant difference from the cellular networks in public places. Its consequence is that many transceivers are required for the indoor networks. Another issue of indoor networks is that the network itself should be very cost-efficient. Unlike the access network constructed by operators, the indoor networks are privately owned and its installation cost should be borne by the terminal users. Thus the conflict between the low-cost architecture and multiple access points should be solved with the novel techniques.

Currently, indoor networks are seemingly the final bottleneck for good user experience with high-speed applications. Users will soon demand very high throughput inside their home or office. The indoor networks need to evolve rapidly to satisfy such demand. And we believe the evolution of indoor networks should well address the three challenges mentioned above.

1.2.3 Converged indoor networks based on fibre-wireless system

To fully meet the three challenges above, researchers have started to investigate many different solutions. Actually the starting point is to find a broadband medium and then think about how to build up a system based on such medium with future-proof features and low cost architecture [11].

Fibre network as a backbone of future indoor networks

It is widely recognized that an optical fibre link is the most eminent network medium to integrate a full range of various services into a uniform single network due to its advantages of broadband, low loss, relatively small size and electromagnetic interference (EMI) free features. Optical fibre is also not electrically conducting generally and it can be deployed together with power line to share the same ducts, which can give major savings in installation costs. In contrast, it is impossible to put copper pairs or coaxial cables together with power line due to safety considerations. There are several types of fibres for indoor applications: silica single-mode fiber (SMF), silica multimode fiber (MMF), and plastic optical fiber (POF). In general large-core POF is very interesting because of its ease of connectorizing and splicing, which suites the low-cost “do-it-yourself” installation. Silica SMF and MMF require professional dealing with delicate skills and tools for installation which increases the total cost. If we further consider the operation expense, the power consumption over the lifetime of an indoor network should be taken into account as well. For an SMF indoor network, fully-passive optical power splitting or wavelength routing devices can be used to form the add/drop nodes and the splitter nodes in the point-to-multiple point topologies due to the single mode waveguiding of SMF. The only power consumption is the opto-electronic (O/E) conversion devices at the end sides of networks. Moreover, such SMF links are fully transparent for all types of signal formats, and they can deploy a wide range of wavelength channels for multiplexing many different kinds of services.

An SMF-based indoor network with passive optical nodes is therefore the most power consumption-lean solution and also the most future-proof solution as it is robust to upgrade to any new signal format. Thus we can see that the SMF is mostly preferred medium to well address challenge-1/-2.

Fibre-wireless system enables energy-efficient and cost-efficient indoor networks

The rapidly increasing amount of wireless devices is congesting the industrial, scientific, and medical (ISM) radio spectrum, and their mutual interference seriously hinders reliable communication. This situation is becoming very severe in public places like train station, airport and shopping mall. As we discussed in section 1.1.3, the incumbent radio cells need to be transformed into small cells with reduced coverage to reduce the interference and the congestion. Unlike these large-area places, the indoor networks inherently support small cells due to their spatial isolation feature enabled by the high attenuation of walls, especially for high-frequency mm-wave bands. However, as indicated in challenge-3, how can we efficiently connect the different small cells? And even more challenging, how can we obtain an affordable cost level for multiple transceiver modules? As we discussed above, optical fibres can provide the broadband wired connectivity, but we still miss a solution to control the cost of transceivers. A revolutionary system approach named fibre-wireless integration technique or radio-over-fibre (RoF) technique can provide an answer by using a centralized network architecture. The core idea is to move signal processing units in remote access points (RAPs) of a link (at its network edges) to a central site. These signal processing units include the frequency up-conversion block, and baseband signal processing block. A RAP more or less serves as a simple active antenna site and does not need to contain signal processing functions anymore. The whole system can be considered as a distributed antenna system. By doing so, the power consumption, installation and maintenance will be largely reduced. Moreover, upgrading to new radio standards require only changes of the central site and not at the many RAPs, which is much more convenient.

Main consideration of indoor fibre-wireless systems

Now, the advantages of indoor fibre-wireless networks are clear and three challenges can be well addressed. However, to pave the way for future applications of indoor fibre-wireless networks, there are two main considerations as mentioned below.

- Concern-1: How to well design the suitable gateway and corresponding indoor network topology. To well address all the virtues of the fibre-wireless network, practically, a versatile and cost-effective gateway is demanded for radio frequency up-conversion and indoor indoor exchange functions. Such gateway is expected to deal with various services with different signal format. In a broadband fibre-wireless network, the cost, flexibility (e.g. flexibility for module upgrading) and simple architecture are the main factors for the gateway and the indoor fibre topology design.
- Concern-2: How to support upcoming wireless services in terms of its network function and its upcoming core techniques. The support for upcoming wireless core techniques in a fibre-wireless network is considered in two folds. The first level is to examine whether a fibre-wireless network can provide a simplified and efficient signal link to realize the wireless core techniques. The

second is to examine, investigate whether a fibre-wireless network can provide possibilities to optically realize the wireless core techniques thus offering topological and operational advantages.

1.3 Technical road map of SOWICI and the scope of this thesis

The research results in this thesis are inspired and financially supported by the NWO project Smart Optical Wireless In-home Communication Infrastructure (SOWICI) in the NWO/STW Smart Energy System program. SOWICI investigates the future indoor networks in context of upcoming wireless services like 5G cellular service with a step ahead. The research inside SOWICI aims of a versatile solution to fulfill the requirement of future indoor networks by means of fibre-wireless systems. The two concerns mentioned in Section 1.2.3 are then well answered by the investigations of SOWICI. In the proposal of SOWICI project, Prof. A.M.J. Koonen proposed an efficient IFiWiN architecture empowered by optical radio beam steering as shown in Figure 1.1. A fibre network connects all radio access points and the optical beam steering is controlled remotely by optical wavelength tuning in a home control center. All reconfiguration nodes can be passive wavelength-selective devices which can further allow a simple and stable IFiWiN system. The home control center can provide flexible switching and routing functions via wavelength tuning as well. To accommodate this efficient architecture, SOWICI

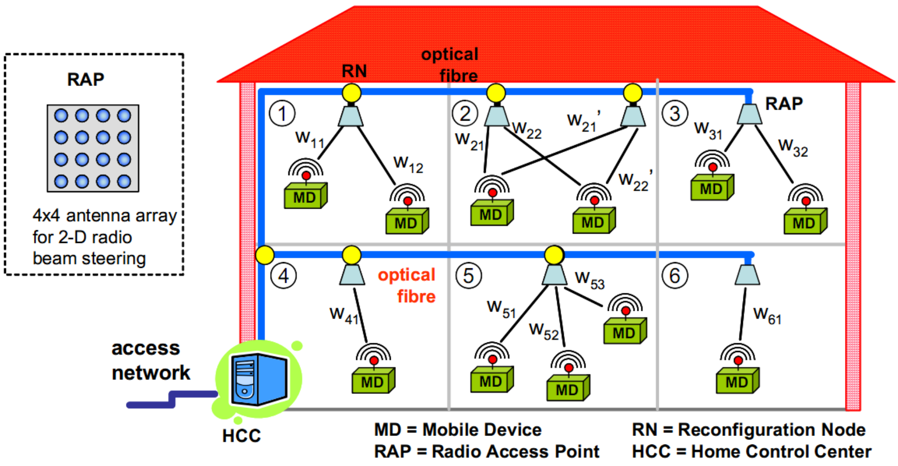

Figure 1.1 An efficient IFiWiN architecture empowered by optical radio beam steering proposed by Prof. A.M.J. Koonen in SOWICI project.

defines its scopes as follows.

1.3.1 The scope of SOWICI

SOWICI is carried out by three Ph.D students from TU/e, TUD and UT, respectively. Inside SOWICI, we propose a novel hybrid fibre-wireless network architecture that integrates the home automation network with the high bit-rate indoor network in a very energy-efficient way. The scientific research objectives (SROs) of the SOWICI project are:

- SRO-1: Broadband and future-proof communication infrastructure for fixed and mobile wireless electronic devices for data and multimedia services, and for sensors and actuators for domotic services,
- SRO-2: Energy-efficient wireless pencil radio beam-steering in mm-wave bands, using phased antenna arrays with tunable beam steering in two dimensions by novel fibre-optic phase shifter techniques,
- SRO-3: Accurate localization and tracking of wireless (mobile) devices in rooms,
- SRO-4: Intelligent control and energy management with a centralized home controller, and
- SRO-5: Scalable and energy-efficient implementation of signal processing algorithms on centralized energy-lean hardware platforms for adaptive radio beam-shaping, –steering, device localization and -tracking.

On the side of TU/e, we mainly focus on SRO-1/-2, partially on SRO-3. And our research in physical layer and the prototype system can provide support for SRO-4 and SRO-5.

1.3.2 The contents of this thesis

The research regarding the scientific research objectives indicated in Section 1.3.1 is carried out in the context of the future fibre-wireless networks discussed in Section 1.2. Here we introduce the research carried out on the TU/e side, which resulted in the contents of this thesis. The investigation of SRO-1 produced a series of results for the efficient gateway and the corresponding network architecture of indoor fibre-wireless networks, which will be detailed in Chapter 2. These results also show the good support for two core technologies, small cells and mm-wave communications. As a necessary auxiliary part for the gateway, a novel and simple control signaling delivery system related to SRO-4 and -5 is proposed and investigated in Chapter 5. Another core technique, radio beam steering (a case of advanced MIMO) related to SRO-2 is investigated in Chapter 3. The fibre-wireless networks are not only compatible with radio beam steering techniques, but also enable many advanced features such as independent steering of multiple radio beams by a single PAA (by using multiple independent wavelength channels) offered by the optical approach. As an assistant part for radio beam steering, the localization of radio devices related to SRO-3 is needed. To explore the advanced features of an optical approach for radio device localization, the optical localization of radio devices is studied in Chapter 4. Based on the proposed optical radio beam steering techniques, the beam steered fibre-wireless (RoF) systems are demonstrated and experimentally evaluated in Chapter 6. In Chapter 7, the thesis is concluded with remarks about the achieved results and an outlook on future research activities to expand this promising field of fibre-wireless networks.

Chapter 2 Gateway Functions for Indoor Fibre-Wireless Networks

The gateway functions and architecture design of indoor fibre-wireless networks (IFiWiNs) is the key to well address all network functions. In this chapter, the signals to be delivered in IFiWiNs are discussed in Section 2.1. Two main categories of signals are addressed in this chapter. To efficiently deal with these two types of signals, three main functions of IFiWiN gateways are described in Section 2.2, namely flexible-reach data delivery, convenient frequency up-conversion, and versatile indoor exchange (IE) functions. To realize these functions, the current radio-over-fibre (RoF) techniques are also discussed in Section 2.2 with emphasis on the operating bands of millimeter-wave and methods to achieve high throughput. Three IFiWiN gateways are designed for three different application scenarios. A simplified remote up-conversion (RUC) scheme for the low residential density IFiWiNs is investigated in Section 2.3. In Section 2.4, the gateway for versatile indoor exchange functions with flexible-reach is studied. And in Section 2.5, a gateway of ultra-broadband data delivery for dense indoor networks is proposed.

2.1 Signals delivered over IFiWiNs

The generic network architecture of an IFiWiN is shown in Figure 2.1. Usually there are three categories of signals delivered to the IFiWiN gateway. The gateway is designated to deal with these incoming signals, and also to process the data exchange functions inside. These signals may come from the optical access networks (OANs) such as fibre-to-the-home (FTTH) or from the up-level indoor/-building networks. There are three main categories of signal processing to be dealt with in the gateway, which can be described as follows:

- Category-1: Converting baseband digital signals in OAN to/from indoor RF signals. For the digital signal, the gateway acts as an optical network unit

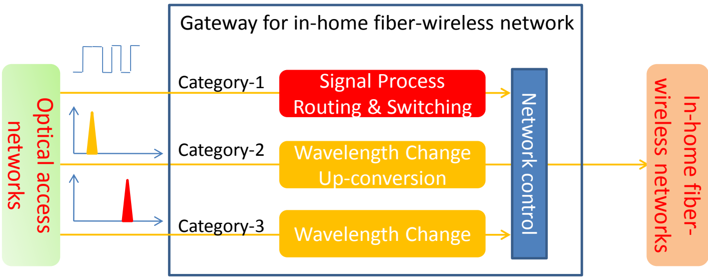

Figure 2.1 Data categories for IFiWiN.

(ONU). The functions of indoor network management, routing, switching, modulation and up-conversion (frequency up-conversion from baseband signal to RF signal with high-frequency carrier) are included in a gateway. Taking WiFi internet services for example, when the baseband data is delivered to an IFiWiN, the routing, switching, signal modulation and other network functions are realized in the gateway. In this case, the OAN only sends and receives the digital signal to/from gateway and it does not care what happens after the gateway. The gateway provides baseband digital signal processing (DSP), up-conversion and indoor exchange functions to the category-1 signals.

• Category-2: Converting IF data signals in OAN to/from indoor RF signals. As in Figure 2.1, the OAN sends the high capacity and low carrier frequency signals to the gateway and the gateway only up converts the IF signals into high-frequency RF signals and does not make any change of the protocol or signal format. The IFiWiN can be configured to allow dynamic bandwidth allocation. After up-conversion, the signals can be transmitted to one room or to a set of rooms. The gateway provides the up-conversion and indoor exchange functions for category-2 signals. The complexity of baseband DSP is moved from the indoor gateway to the OAN.

• Category-3: Transparent handovers of RF data signals from OAN to/from indoor network, without conversion. As shown in Figure 2.1, the OAN sends the large capacity RF signals (usually at millimeter-wave frequency) to the gateway. The gateway does not make any change of the carried data to allow a transparent delivery which is energy efficient and scalable for future services. The gateway is somehow transparent for the OAN and it only provides the indoor exchange functions to category-3 signals. The complexity is mainly kept in the OAN.

Among these signals, the category-1 and -2 from the OAN are the main concerns in this chapter since category-3 would introduce considerable complexity and architecture changing in the OAN. The OAN is usually pre-deployed and thus any amendment of its architecture should be avoided. However, the involved techniques can be extended for category-3 signals easily since their complexity is lower than the other two.

2.2 Gateway functions and suitable designs

As discussed in Section 2.1, there are three functions in the gateway. First is the baseband DSP, which should be dealt with signal modulation and other communication DSP functions by electrical integrated circuits. Second is the frequency up-conversion, which up-converts baseband data onto mm-wave carrier frequency. Third is indoor exchange functions, which allow data switching and routing inside IFiWiNs. In Section 2.2.1, the requirements for up-conversion techniques are discussed in terms of technical demands and cost considerations. Then two suitable up-conversion techniques are proposed to satisfy the system requirements (flexible reach data delivery, convenient frequency up-conversion, and versatile indoor exchange). The design of IFiWiN gateways should consider both indoor networks requirements/limitations and the interface with OANs. Usually the interface requirement for OANs should be relaxed, and the gateway system should be simple. In Section 2.3, a gateway design for low residential density IFiWiN applications is investigated. Further, in Section 2.4, a gateway for high density IFiWiN with indoor exchange functions is studied. In Section 2.5, a gateway with full radio frequency agility and indoor exchange functions is investigated for high density IFiWiN with very high throughput.

2.2.1 Up-conversion techniques

As discussed in the introduction section, future indoor wireless networks are required to deliver high-speed services scaling from the 100 Mb/s level at low frequency bands (2.4/5.8 GHz) up to the 10 Gb/s level in mm-wave bands.

Regarding the physical aspect, the higher frequency mm-wave bands are preferred due to their large bandwidth. Therefore, mm-wave communications are viewed as an interesting solution for future wireless networks. However, mm-waves are prone to high atmospheric loss, which, thereby, limits its delivery flexibility, especially for indoor scenarios. Consequently, fibre-wireless networks are sought-after due to the ultra-low loss and the huge bandwidth of optical fibres [12-41]. In such networks, the mm-wave signal is generated at a central station (CS) and modulated onto an optical carrier. At an base station (BS), the optical signal is converted to the electrical signal via a photodiode (PD) and then, its amplitude is fed to the antennas by cascaded electrical amplifiers. Therefore, the complexity of BSs can be reduced. As the major solution, many mm-wave fibre-wireless systems based on external modulation (EM) have been proposed due to their low phase noise, optical frequency multiplexing capability and commercial supply of external modulators[13, 42].

The most dominant schemes are based on two-stage modulation. The first stage is for optical mm-wave generation, whereby multiple lightwave channels can share one modulator. Consecutively, multi-channel data are modulated on separate channels in the second stage. To allow a simple and stable structure, intensity modulation with double sideband is employed. However, its applications are limited by several issues. First, the wireless operating bands are limited by electrical oscillators and bandwidths of external modulators. Second, the frequency agility of wireless signal is a trade-off against the system complexity. Usually the frequency of the wireless carrier should be flexible to avoid collisions in cell networks, however, in many EM systems [15, 16, 30, 32, 38], the optical mm-waves (optical carriers modulated with electrical LO) are shared by many different wireless services in order to reduce the overall cost. Thus, the frequency agility is difficult to be guaranteed. Third, in most double sideband modulation systems the bandwidth of modulated wireless signals and its transmission distance are intrinsically limited by the dispersion-induced frequency selective fading [43]. Even for short reach (~5 km), due to the high frequency (>30 GHz) of optical mm-waves and broad bandwidth of modulated data, fibre dispersion will introduce considerable frequency selective fading, which will cause a severe power penalty. Optical single sideband modulation schemes (OSSB) based on external modulation can overcome the distortion-induced frequency selective fading [13, 44]. However, most of such OSSB schemes require complicated structure with accurate phase control circuits, which limits its implementations. Moreover, electrical mixers are usually involved and their imperfect features such as bandwidth limitation, nonlinearity and conversion loss largely decrease system performance.

In this chapter, two techniques suitable for IFiWiNs are proposed. One is the all-optical remote up-conversion (RUC) technique, and the other is free-running laser-based optical heterodyne technique (OH). All-optical RUC technique sends both optical baseband data and optical mm-wave frequency to a gateway with up-conversion realized in a remote site. In this way, the dispersion induced walk-off effect or frequency selective fading can be significantly avoided. For OH, baseband data is modulated on one wavelength and the other wavelength is used for optical beating to up convert the baseband data. Similar to RUC, OH can relieve dispersion induced walk-off effect or frequency selective fading.

With no electrical local oscillator involved, OH generates mm-wave only depending on the spectral separation of two optical wavelengths. Thus it can provide a flexible generation of mm-wave at different frequencies. In Section 2.3, a simplified RUC system is proposed and studied. The all-optical RUC with optical indoor exchange functions is demonstrated in Section 2.4. In Section 2.5, a very high throughput indoor fibre-wireless network enabled by OH and polarization multiplexing (PolMux) is investigated.

2.2.2 Optical indoor exchange functions

The traffic-load profiles attributed to wireless services are different from fixed networks, because of the mobility of the users. Therefore an IFiWiN ought to provide dynamic bandwidth allocation (DBA) in order to adapt to the varying local traffic load in its gateway. Moreover, internal data processing is also required for IFiWiN, especially for high definition video streaming. Thus routing (indoor exchange function) inside IFiWiN is demanded and should be controlled by the gateway. To avoid intricate electrical signal processing, optical indoor exchanges enabled by gateway functions are studied in Section 2.4 and 2.5. In such schemes, an IFiWiN is static with fixed wavelength router such as an arrayed waveguide router. The IE functions are realized by tuning optical carrier wavelengths, and the active part can be kept at a gateway while leaving the other parts passive. In this way, the complexity of IFiWiNs can be reduced.

To further simplify IFiWiNs, it is necessary to implement IE functions in an efficient way. In Section 2.4, the IE function is combined with the RUC in one-step procedure, while in Section 2.5, the IE function is accomplished with the OH.

2.3 Simplified remote up-conversion scheme

RUC can reduce the dispersion induced walk-off effect by generating the optical mm-wave in a remote site. The RUC mixes (or modulates) the data signal on optical mm-wave in the remote access point or remote gateway (GW) after fibre transmission. Thus the dispersion induced walk-off effect can be avoided. In such scheme, two laser sources and two MZMs are individually used for baseband (BB) data modulation and blank optical mm-wave generation (without data modulation). Note such optical mm-wave may still suffer from power-fading and some advanced schemes are proposed in [13]. In this section, a simple RUC scheme based on electrical tones injection has been proposed to address both issues discussed above. Thanks to electrical tones injection, BB data modulation and blank optical mm-wave generation can share the same

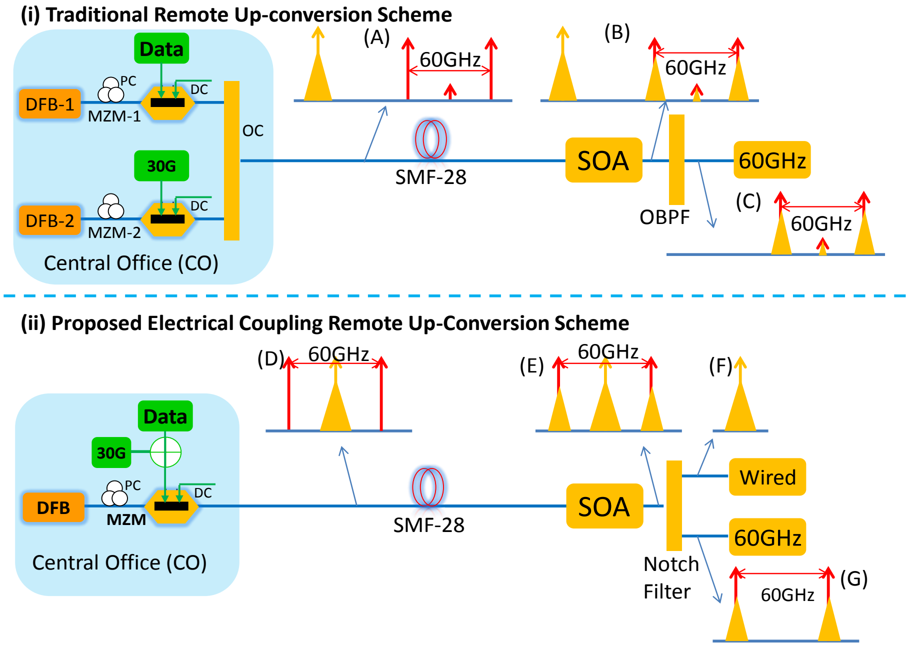

Figure 2.2 The schematic of the remote up-conversion based on electrical tone injection (RUC-ETI). DFB: distributed feedback laser; MZM: Mach-Zehnder modulator; PC: polarization controller; 30G: 30 GHz local oscillator; DC: direct current bias; SMF-28: single mode fibre; SOA: semiconductor optical amplifier; Wired: wired service; 60GHz: 60 GHz wireless service.

laser source and MZM. Moreover, such scheme can simultaneously provide wired service and 60 GHz wireless service for seamless convergence, which is beneficial for wireless service upgrading of existing passive optical networks (PON). In Section 2.3.1, the operation principle is studied. The experimental results are discussed in Section 2.3.2.

2.3.1 Operation principle and theoretical analysis

In this part, the operation principle of proposed RUC-ETI is described comparing with traditional RUC scheme. The traditional scheme is depicted in Figure 2.2(i). The laser at 1st wavelength (DFB-1) is for BB data modulation and the laser at 2nd wavelength (DFB-2) is for blank 60 GHz optical mm-wave generation. The MZM-2 is biased at its null point to allow optical carrier suppression (OCS) for optical frequency doubling. Then, two wavelengths are coupled before fibre transmission with spectrum shown in Figure 2.2(A). After fibre transmission, two wavelengths are fed into a semiconductor optical amplifier (SOA) for cross gain modulation (XGM) process. BB data is then copied to blank optical mm-wave. The optical mm-wave with copied BB data is then filtered by an OBPF with central wavelength at the 2nd wavelength to generate wireless signal after O/E conversion.

The operation principle of RUC-ETI scheme is shown in Figure 2.2(ii). The optical mm-wave is generated by electrical tones injection based on electrical coupling. The BB data and 30 GHz local oscillator (LO) are electrically coupled and then amplified to drive a MZM biased at the linear region of its power transfer curve. The optical spectrum after the MZM is illustrated in Figure 2.2(B). After been transmitted over fibre, the optical signal is fed into a SOA for XGM. After the SOA, BB data carried by the optical central carrier is copied to two tones (optical mm-wave) to realize remote up-conversion with optical spectrum shown in Figure 2.2(E). The optical central carrier and sideband are then separated for wired and wireless services by an optical notch filter (ONF) with optical spectrum show in Figure 2.2 (F) and (G). Thus it is clear that the core idea of RUC-ETI is to use electrical coupling of BB data and LO signal to generate optical mm-wave sharing the same wavelength. By doing so, the laser source and MZM can be shared and only one WDM channel is occupied.

The general mathematical model for RUC is described in the following. The comparison of RUC-ETI and traditional RUC will be discussed based on this model. The optical carrier at the angular frequency ω_c with E_I amplitude can be expressed as:

$$E(t) = E_I \cos(\omega_c t) \tag{2.1}$$

The electrical data is modulated on the optical carrier via a push-pull operating MZM and thus the optical data wavelength (ODW) signal can be expressed as:

$$\begin{aligned} E_m(t,z) &= \frac{E_I}{2}[\cos(\omega_c t + \pi\frac{\sqrt{2}}{2}S_{norm}(t) - \beta(\omega)z) + \cos(\omega_c t - \pi\frac{\sqrt{2}}{2}S_{norm}(t) - \beta(\omega)z)] \\ &= E_I \cos(\omega_c t - \beta(\omega)z)\cos(\pi\frac{\sqrt{2}}{2}S_{norm}(t)) \end{aligned} \tag{2.2}$$

where $\beta(\omega)$ denotes the optical phase delay per unit length of the engaged fibre (propagation constant) for different optical angular frequency components. $S_{norm}(t)$ denotes the normalized presentation of the BB signal and is given by:

$$S_{norm}(t) = S_{base}(t) + S_{bias} = \frac{S_{BB}(t)}{V_{\pi 1}} + \frac{V_{bias-a}}{V_{\pi 1}} \tag{2.3}$$

where $S_{BB}(t)$ is BB signal and $V_{\pi 1}$ is the switching voltage of MZ-a. $V_{bias\text{-}a}$ is the bias voltage applied to MZ-a. Considering the pre-distortion with bias at linear point (V_π) of MZM field curve, so V_{bias}=V_π, and feeding $S_{norm}(t)$ via the pre-distortion function $y=(\sqrt{2}/\pi)\arccos(x)$, the output electrical field can be written as:

$$\begin{aligned} E_m(t) &= E_I S_{norm}(t)\cos(\omega_c t-\beta(\omega_c)z) \\ &\cong E_I[1+S_{base}(t)]\cos(\omega_c t-\beta(\omega_c)z) \end{aligned} \quad (2.4)$$

We replace $\beta(\omega)$ with $\beta(\omega_c)$ because that the dispersion induced distortion is not significant for low data modulation bandwidth (2.5 Gb/s) and short fibre distance (50 km). The E-field of the pure optical mm-wave (without data modulation and without optical carrier, OMW) can be expressed as:

$$E_p(t)=\sqrt{\bar{P}_{LO}}\cos(\omega_o+0.5\omega_{LO})t+\sqrt{\bar{P}_{LO}}\cos[(\omega_o-0.5\omega_{LO})t+\theta] \quad (2.5)$$

where $\bar{P}_{LO}$ is the average power of OMW and $\sqrt{\bar{P}_{LO}}$ presents its amplitude. And $\omega_o \pm 0.5\omega_{LO}$ are the optical frequencies of the upper and lower sidebands of OMW, and θ is the phase difference in between which is induced by dispersion. The XGM process can be then expressed as:

$$\begin{aligned} E_{op}(t) &= G\times E_{em}(t)\times E_p(t) \\ &= G\times E_I[1+S_{base}(t)]\times\sqrt{\bar{P}_{LO}}[\cos(\omega_o t+0.5\omega_{LO}t)+\cos[(\omega_o\text{-}0.5\omega_{LO})t+\theta]] \end{aligned} \quad (2.6)$$

where $E_{em}(t)$ is the envelop of $E_m(t)$. G is the cross conversion gain which will be discussed in following. Here we assume that the amplitude of $E_m(t)$ linearly modulates the gain of the SOA through the XGM process. For Eq. (2.6), we can see the data on ODW will be modulated on the OMW after XGM process. After the photo-detector, the output current can be expressed as:

$$I=\left|E_{op}(\mathrm{t})\right|^2=G^2\times\left|E_{em}\right|^2\times\left|E_p\right|^2=G^2\times\left|E_p\right|^2\times I_m=\eta\times I_m \quad (2.7)$$

where η is the conversion efficiency. We can see that the dispersion-induced phase difference θ will not affect the photo-detected signal as shown in Eq. (2.7). Now we investigate the conversion efficiency η. In [45], this parameter is introduced and discussed for remote up-conversion applications. It can be expressed as:

$$\eta=\left|\frac{G_{LO}a_{LO}\bar{P}_{LO}(G_d-1)}{2\hbar\omega_o A_{eff}(j\omega_d+\gamma_{eff})}\right|^2 \quad (2.8)$$

where G_{LO} and G_d are the SOA optical gains at the wavelengths of OMW and ODW, a_{LO} the transparent carrier density, $\hbar$ the reduced plank constant, A_{eff} the effect mode area, γ_{eff} effective recombination rate, and ω_d the optical angular frequency of ODW. Eq. (2.8) describes the behavior of η based on the single frequency ω_d, however it is still applicable for ODW [45] since the data signal can be consider as a set of frequency components. Based on Eq.(2.8), the conversion efficiency is proportional to the SOA optical gain and the LO light intensity. The conversion efficiency also depends on the OMW and ODW because the optical gain in an SOA is wavelength-dependent. Since the OMW and ODW in the proposed RUC-ETI scheme are close to each other in frequency domain, they can be set to the highest gain area in frequency domain. It means the conversion efficiency in RUC-ETI scheme should be larger than in the traditional RUC scheme.

2.3.2 Experimental setups, results and discussion

The experimental setup of RUC-ETI is depicted in Figure 2.3. The 1543.78 nm optical carrier with 7.2 dBm optical power is generated by a DFB laser. The 2.5 Gb/s OOK pseudorandom binary sequence (PRBS) data is electrically combined with injected 30 GHz LO via an HP electrical coupler. The coupled electrical signal is then modulated on the optical carrier via a MZM after a polarization controller (PC). The OOK data with a word length of 2^{31}-1 is

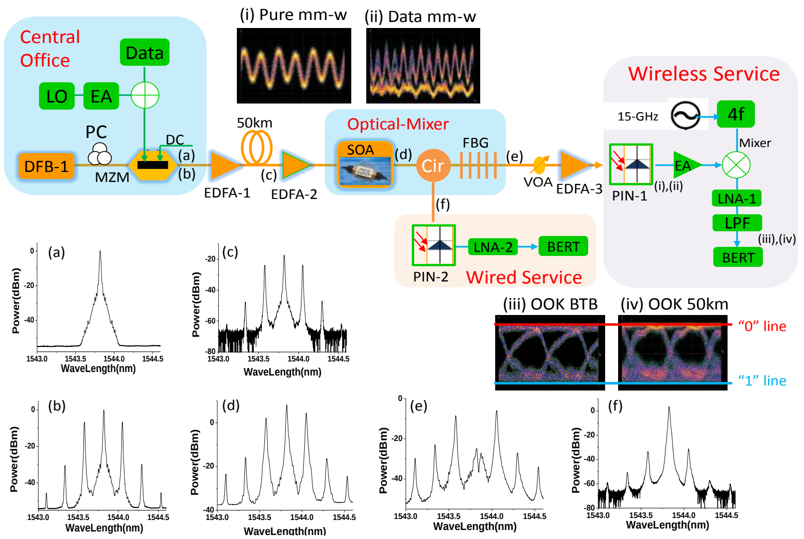

Figure 2.3 The experimental setup of RUC-ETI. DFB: distributed feedback laser; MZM: Mach-Zehnder modulator; PC: polarization controller; LO: 30 GHz local oscillator; EA: electrical amplifier; DC: direct current bias; EDFA-1 and -2: Erbium doped fibre amplifier; SMF-28: single mode fibre; SOA: semiconductor optical amplifier; Cir: optical circulator; FBG: cascaded PIN-1: 75 GHz p-i-n photo-diode; PIN-2: 10 GHz p-i-n photo-diode; LNA-1 and -2: 3 GHz eletrical low noise amplifier; Mixer: electrical mixer; 4f: electrical frequency quadruple multiplier; BERT: bit error rate tester.

generated by the pattern generator (HP70834C) with a 2-V amplitude (peak-to-peak). The LO signal is generated from Agilent 836502 and followed by an electrical power amplifier. Figure 2.3(a) shows its optical spectrum when only the OOK data is modulated. Figure 2.3(b) presents the optical spectra when both OOK data and 30 GHz LO are simultaneously modulated. Next to the optical carrier with OOK data and the two sidebands, two 2^{nd} harmonics of the 30GHz LO signals are observed. The modulated optical signal is amplified by an erbium doped fibre amplifier (EDFA-1) and transmitted over 50 km SMF-28. After been transmitted over fibre, the optical signal is fed into the optical mixer as shown in Figure 2.3. The optical mixer includes an optical pre-amplifier (EDFA-2) and a SOA for purpose of XGM. The optical power after the optical pre-amplifier is 7 dBm. The optical spectra before and after optical-mixer are shown in Figure 2.3(c) and (d). Comparing Figure 2.3(c) and (d), the third order sidebands have increased a little bit due to four wave mixing (FWM) effect in the SOA. After the optical mixer, an optical circulator with two cascaded fibre Bragg gratings (FBGs) are employed to separate optical central carrier and sidebands, which are used for wired service and 60 GHz wireless service, respectively. Both FBGs are centralized around 1543.78 nm with 6 GHz pass-band bandwidth. The optical spectrum of separated optical carrier and sidebands is shown in Figure 2.3(e) and (f), respectively. The optical central carrier is not perfectly suppressed due to central alignment offset between two FBGs. A variable optical attenuator (VOA) is used to control received optical power (ROP) for measurement. Two optical receivers are constructed for both wired and wireless services. The optical receiver for wired service comprises a 10 GHz PD (PIN-2) and a low noise amplifier (LNA-2) with 3 GHz -3 dB pass-band bandwidth. The optical receiver for wireless service is constructed to emulate a remote antenna point (RAP) and terminal users (TU). The RAP contains a preamplifier EDFA (EDFA-3) and 75 GHz PD (PIN-1). The data-modulated 60 GHz optical mm-wave is converted to an electrical 60 GHz wireless signal after RAP. The retrieved mm-wave signal is amplified by a narrow-band amplifier with 8 GHz -3 dB pass-band bandwidth centralized at 60 GHz. The amplified 60 GHz signal is then down converted to BB data using a 60 GHz electrical mixer with 60 GHz LO. The 60 GHz LO is generated from an electrical frequency quadruple multiplier fed by a 15 GHz microwave source. An electrical low-pass filter with 3 GHz -3 dB bandwidth is cascaded with a 3 GHz low noise amplifier (LNA-1) to retrieve the 2.5 Gb/s data for the bit error rate (BER) measurement.

The performance of the proposed RUC-ETI scheme is assessed based on eye-diagrams and bit error ratio (BER) measurements. The pure mm-wave is depicted in Figure 2.3(i), being captured when the OOK data is switched off. The 60GHz optical mm-wave is slightly distorted mainly due to the imperfect

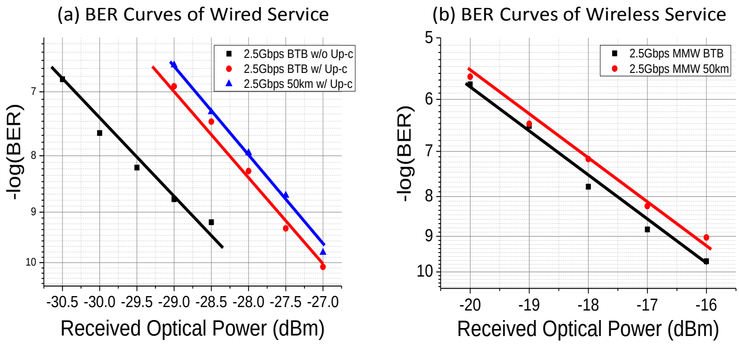

Figure 2.4 The measured BER curves of 2.5 Gbps on-off-keying signal for (a) wired service and 2.5 Gbps on-off-keying signal for (b) wireless service.

suppression of optical carrier. The (mm-wave) eye-diagram of the data modulated 60GHz mm-wave is depicted in Figure 2.3(ii). The down-converted eye-diagrams of the retrieved OOK data is shown in Figure 2.3(iii) and (iv) for optical back-to-back (BTB) and 50 km fibre transmission, respectively. The polarity of digital zero and one is inverted due to XGM. Thus the “0” line is in the top while the “1” line is in the bottom. The blur in the “1” line is caused by the electrical reflection of OOK data during the electrical coupling. This issue can be avoided if an electrical isolator is used. We can see that the rising and falling edges are clear and no obvious ISI is introduced. That means the walk-off effect is successfully eliminated.

As shown in Figure 2.4(a), the received optical power (ROP) of wired service without RUC at BER of 10^{-9} is -28.7 dBm, and the wired service with RUC are -27.6 dBm and -27.4 dBm for BTB and 50 km SMF-28 transmission, respectively. It is clear that the power penalty introduced by RUC is 1.1 dB and the power penalty for 2.5 Gb/s wired service over 50 km is 0.2 dB. The BER curves of 2.5 Gb/s wireless service at 60 GHz are plotted in Figure 2.4(b). Its ROPs are -16.6 dBm and -16.3 dBm for BTB and 50 km SMF-28 transmission respectively and the power penalty is 0.3 dB.

2.3.3 Conclusion

A simple 60 GHz remote up-conversion scheme with electrical tones injection is proposed and experimentally demonstrated for low density IFiWiN. According to our knowledge, the RUC scheme with only one modulator is proposed here for the first time. Such scheme can provide both wired and wireless service without any additional device. Experimental results show that 2.5 Gb/s wired service and 2.5 Gb/s wireless service at 60 GHz are successfully delivered over 50 km SMF with a power penalty less than 0.3 dB. Its features of low cost, stability, and robustness towards fibre dispersion indicate that it is suitable for a cost-efficient low density IFiWiN.

2.4 Remote up-conversion and indoor exchange

Reconfigurable fibre-wireless networks are attractive due to their capability to allocate bandwidth in the physical layer in terms of capacity on-demand and/or user mobility for the last mile [29, 33, 36]. To be compatible with next generation PON (NG-PON) with extended coverage (>100 km) [46], a gateway of IFiWiN capable to deal with flexible-reach (up to 100 km) and high capacity (≥5 Gb/s) with IE functions is needed. The RUC technique discussed in Section 2.3 can avoid the dispersion induced walk-off effect, but it is suitable for simple IFiWiN with a few wavelengths existing in one fiber link because a large WDM grid is occupied by mm-wave wireless channels. More in such system IE functions cannot be realized due to its simplified gateway. To realize reconfigurable operation, networks are expected to provide dynamicity to route different optical signals among different flats/rooms in the GW. Thus, IE functions like routing and multi-casting are demanded. To reduce costs and improve stability, an all-optical IE is preferred to eliminate intricate electrical processes. An all-optical IE can be realized by copying the data from one wavelength to another wavelength by means of cross gain modulation or other optical processes. Therefore, in essence, the RUC and IE functions are realized by copying data to specified wavelengths. The difference is that the RUC copies data to optical millimeter waves, which usually include a pair of two wavelengths but the IE copies data to one wavelength only. This means that we can realize two different functionalities into one combined process. In this case, the system cost (CAPEX) and maintenance cost (OPEX) can be reduced.

In this section, a novel hybrid fibre wireless network with an integrated all-optical RUC and IE system is proposed for a high density IFiWiN. A proof-of-concept experiment has been carried out to investigate the proposed system. In Section 2.4.2, the experimental results show that 5 Gb/s OOK data carried by a 60 GHz hybrid fibre wireless channel over 102 km single mode fibre (SMF) is successfully delivered with a power penalty less than 1.1 dB. The IE functionalities of routing, and optical multi-casting are successfully demonstrated as well.

2.4.1 System architecture

The proposed system is shown in Figure 2.5. The baseband (BB) data is modulated on a wavelength (named as 'BB wavelength') in the central office (CO) and then delivered to a remote node (RN). The distance from RN to destination building gateway (GW) are usually limited to 20 km, and the total distance can reach 100km as expected for NG-PON. In the GW, the wavelength is then split into two paths, one for the down link and the other for the reflected uplink as shown in Figure 2.5. Since time division multiplexing (TDM) is widely used for wireless services, the BB wavelength will be routed to different destinations in different time frames. For instance, in time frame t_1, the data should be sent to room-a (R-a) and, in time frame t_2, the data should be sent to room-b (R-b). The bandwidth allocation depends on the assigned partition of time frames. The destinations also depend on users' locations. To route the BB wavelength, and also to up convert it, the all-optical integrated RUC and IE system is utilized in the GW depicted inside diagram 'GW' of Figure 2.5.

Inside the GW, optical signals are assigned to different flats/rooms in a dynamic way, in order to meet capacity on-demand and user mobility requirements. The dynamic allocation is realized by turning on specified

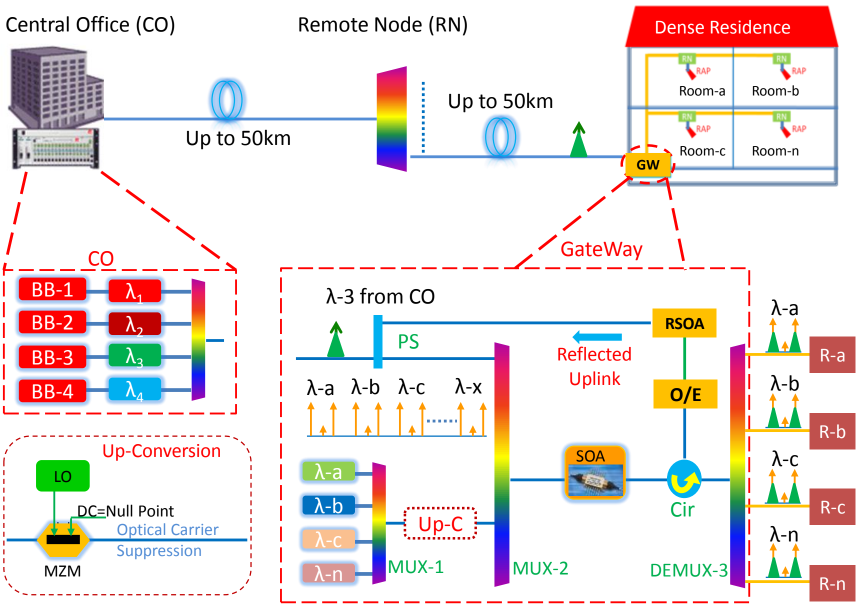

Figure 2.5 The operation principle of all-optical remote up-conversion and indoor exchange. BB: baseband data; LO: local oscillator; MZM: Mach-Zehnder Modulator; MUX: multiplexer; PS: power splitter; RSOA: reflective semiconductor optical amplifier; O/E: optical-electrical convertor; GW: gateway

wavelengths. These wavelengths are multiplexed via an optical multiplexer (MUX-1 shown in Figure 2.5) and modulated using a local MZM biased at its null point with a 30 GHz LO (local oscillator). This process will generate the blank (without data modulation) 60 GHz optical mm-waves at selected wavelengths. These optical mm-waves together with BB wavelength are multiplexed via MUX-2 before being fed into a semiconductor optical amplifier (SOA). The SOA is employed for the cross gain modulation (XGM) process. After XGM, the BB data is optically modulated to the 60 GHz optical mm-waves at the selected wavelengths. The resulting optical mm-waves are separated by a de-multiplexer (DEMUX) and finally distributed to different apartments/rooms over short reach (at most a few kilometers) SMF fibre. The optical routing is realized by switching on one specific local wavelength while switching off the others. The optical multi-casting can be realized by switching on one group of specified wavelengths. The whole IE functionality realization only depends on the local process and local management and therefore it is colorless for the CO.

The uplink to the CO is also illustrated in Figure 2.5. The uplink data from each apartment/room (labeled as ‘R-a’ to ‘R-n’) are detected (labeled as ‘O/E’) and then modulated via a reflective SOA (labeled as ‘RSOA’). The downlink wavelength injected to RSOA is amplified and reflected out of RSOA with data modulation. Thus the uplink wavelength is reused from downlink wavelength with colorless operation [47]. For the proposed system, the multi-wavelength lasers, MZM modulator, AWG and SOA can be integrated into one chip based on an indium phosphide platform. This will largely reduce the system cost and improve the system stability. In the following proof-of-concept experiment, the performances of RUC as well as optical routing and multi-casting will be investigated.

2.4.2 Experimental setups, results and discussion

The proof-of-concept experimental setup is depicted in Figure 2.6. In the CO, a 1547.5 nm (other wavelengths can be chosen since the concept is colorless for CO) optical carrier with 7.2 dBm optical power is generated by using a DFB laser (DFB-1). The optical carrier is, after a polarization controller (PC), then modulated with 5Gb/s NRZ PRBS data via a Sumitomo MZM (MZ-a). The NRZ data with pseudorandom binary word length of 2^{31}-1 is generated by the HP70834C pattern generator with 2V amplitude (peak-to-peak). The modulated optical signal is transmitted over 100 km SMF-28 consisting of two spans of 50 km SMF-28 with an EDFA in-between. The two bundles of fibre are kept inside a closed box to reduce the environment related variation.

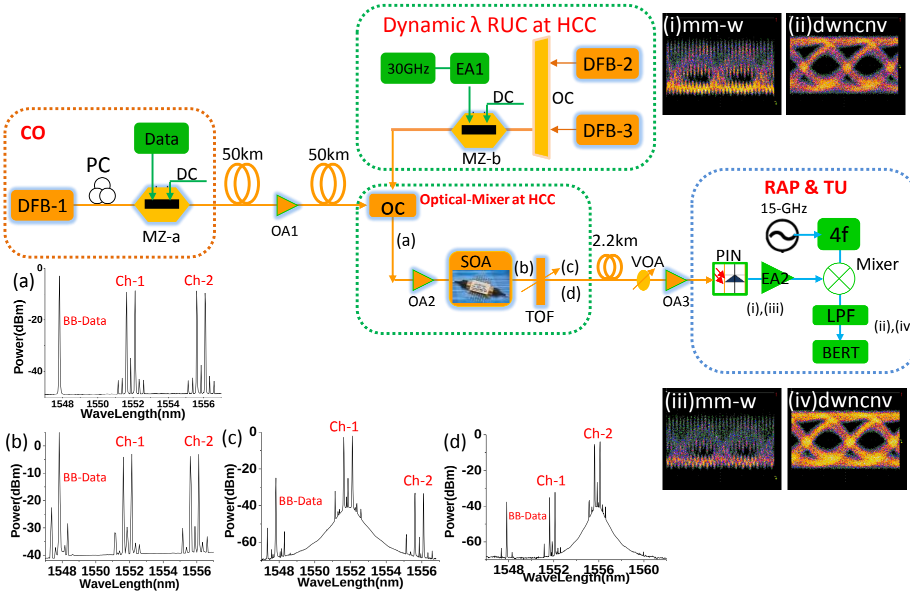

Figure 2.6 The experimental setup of all-optical remote up-conversion and indoor exchange. DFB-1/-2/-3: distributed feedback laser; PC: polarization control; MZ-a/-b:Mach-Zehnder modulators; DC: DC bias; OA1/2/3: Erbium doped fibre amplifiers; OC: optical coupler; EA: electrical amplifiers; SOA: semiconductor optical amplifier; TOF: tunable optical filter; VOA: variable optical attenuator; PIN: p-i-n photo-diode; 4f: electrical quadrupler; LPF: low-pass filter; BERT: bit error rate tester.

Two wavelengths centralized at 1551.8 nm (channel-1) and 1555.7 nm (channel-2) are locally generated from DFB laser sources (DFB-2 and DFB-3). More wavelengths are possible since this architecture is in principle scalable to include more than two destinations. The wavelengths are coupled via an optical coupler (OC) and modulated by a 30 GHz LO signal followed by an electrical amplifier via a MZM (MZ-b) biased at null point. The LO signal is generated from an Agilent 836502 microwave source (noted as MC-1) and amplified by an electrical power amplifier (SHF806E). The power of two probe wavelengths (DFB-2 and DFB-3) is -3 dBm equal to the power of the incoming BB wavelength. The generated 60 GHz optical mm-waves and incoming BB optical signal are coupled and co-propagated to the optical mixer as shown in Figure 2.6. The optical mixer includes an optical pre-amplifier (here it is an EDFA OA2) and a SOA (JDS CQF872) for the purpose of XGM. The SOA has 1.5 mm length with a gain of 17 dB for booster applications and a gain of 22 dB for pre-amplifier applications. The SOA is biased with 420 mA current. Its polarization dependence is within 1 dB. The optical power after the optical pre-amplifier is 7 dBm for both single channel and multi-channel in the following discussion. The optical spectrums before and after optical-mixer are shown in Figure 2.6(a) and (b). Note that a SOA (replacing the EDFA OA2) can be used for optical pre-amplification and therefore the optical mixer can be easily integrated into a single chip. After the optical mixer, a tunable optical band-pass filter with 1nm bandwidth is used to perform the function of DEMUX. The optical spectrum de-multiplexed channel-1 and channel-2 are shown in Figure 2.6(c) and (d). The selected channel is then delivered to the destination room (or apartment) via 2.2 km SMF-28.

An optical receiver is constructed to perform the function of the remote antenna point (RAP) and terminal user (TU). This optical receiver contains a preamplifier OA3 and a tunable optical filter (TOF) with the -3 dB bandwidth of 1 nm to block the ASE. The optical signals are converted to electrical signals by a commercial photo-diode (PIN) with a -3 dB pass-band bandwidth of 75 GHz. The retrieved mm-wave signal is amplified by a narrow band amplifier with -3 dB pass-band bandwidth of 10 GHz centralized at 60 GHz before it is fed into a 60 GHz electrical balanced mixer. The retrieved 60 GHz mm-wave signal is down converted by 60 GHz LO generated from an electrical frequency quadruple multiplier cascaded with a 15 GHz microwave source (noted as MC-2). The MC-2 is phase locked with MC-1 via 10MHz synchronization cable. An electrical low-pass filter with 5 GHz -3 dB bandwidth is employed to filter out the 5 Gb/s data for bit error rate (BER) measurements.

A) Performance of the RUC for a single RoF channel

The performance of the RUC for a single channel (for purpose of routing) is evaluated based on two separate probe wavelengths. The BER for one specified channel is measured while the other channel is turned off. The BER curves of the up-converted channel-1 (1551.8 nm) and channel-2 (1555.7 nm) are plotted in Figure 2.7 for both optical back-to-back (BTB) and over 102km SMF-28 transmission. The received optical powers (ROP) of channel-1 at BER of 10^{-9} are -18.0 dBm and -17.3 dBm for BTB and 102 km SMF-28 transmission, respectively. For channel-2, the ROPs are -18.1dBm and -17.5 dBm for BTB and 102 km SMF-28 transmission, respectively. The power penalties of both channels after 102 km SMF-28 are within 0.6 dB at BER of 10^{-9}. The wavelength dependence between channel-1 and channel-2 is within 0.1 dB for both BTB and 102 km SMF-28 transmission. This suggests that the proposed scheme is suitable for multi-wavelength routing. The power penalty of the incoming BB signal over 102 km SMF-28 is also measured for comparison. The power penalty of the BB signal at BER of 10^{-9} is less than 0.4 dB. Thus the penalty induced by RUC is less than 0.2 dB. The eye-diagrams of the BB signals are presented in Figure 2.6(ii) and (iv). It is clearly shown that the distortion caused by dispersion is slight and no obvious ISI is introduced. The mm-wave and its corresponding baseband eye-diagrams of channel-1 for BTB

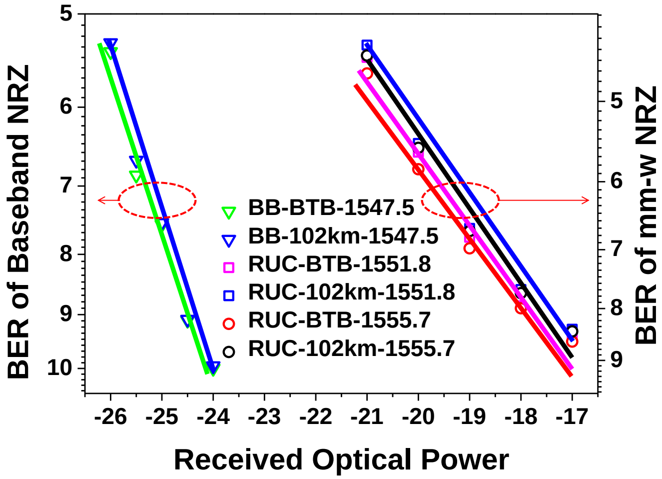

Figure 2.7 BER curves of RUC for single channel and BER curves ($-\log_{10}$(BER)) of BB signal for comparison.

and 102 km transmission are depicted in Figure 2.6(i) and (ii), and Figure 2.6(iii) and (iv), respectively. We can see that the rising and falling edges for 102km transmission are very clear and no evident ISI is observed. The experimental results show that the proposed scheme can work well for RUC and routing.

B) Performance of the RUC for multiple RoF channels

The performance of RUC in case of multiple channels (for the purpose of multi-casting) is evaluated based on two co-existing probe wavelengths. The BER curves of the up-converted channel-1 (1551.7 nm) and channel-2 (1555.8 nm) are plotted in Figure 2.7 (a) and (b) for both BTB and 102 km SMF-28 transmission, respectively. As shown in Figure 2.7 (a), the ROPs of channel-1 at BER of 10^{-9} are -16.9 dBm and -16.4 dBm for BTB and 102 km SMF-28 transmission, respectively. As shown in Figure 2.7 (b), the ROPs of channel-2 are -16.8 dBm and -16.4 dBm for BTB and 102 km SMF-28 transmission, respectively. The power penalties of both channels after 102 km transmission are within 0.5 dB at BER of 10^{-9}. Again the wavelength dependence between channel-1 and channel-2 is within 0.1 dB for both BTB and 102 km SMF-28 transmission. Comparing with the case of single channel, the power penalty induced by the two-channels is within 1.1 dB. All these experimental results suggest that the proposed scheme can perform RUC and multi-casting with acceptable power penalty.

2.4.3 Conclusion

A novel hybrid fibre wireless system with integrated remote up-conversion and indoor exchange functions is proposed and experimentally demonstrated. A 5 Gb/s data signal carried by a 60 GHz mm-wave RoF channel is successfully delivered over 102 km SMF-28 with a power penalty less than 1.1 dB for both single channel (routing) and multiple-channels (multi-casting). Optical routing and multi-casting of 5 Gb/s data carried on a 60 GHz optical mm-wave have been demonstrated as well. All its features indicate that the proposed scheme is suitable for future hybrid fibre wireless networks.

2.5 Broadband up-conversion and routing

In this section, to allow very high throughput IFiWINs with radio frequency agility and IE, a novel IFiWiN gateway is proposed with OH and polarization multiplexing (PolMux). Traditionally, OH systems were proposed with optical phase-locked loop and injection locking to suppress the phase noise [48, 49]. Recently, simplified OH systems are proposed with free running narrow linewidth (low phase noise) lasers and phase noise compensation using digital signal processing (DSP) [23, 50, 51]. These systems can support emergent physical protection for fibre links during disasters. PolMux can further support MIMO services by using two orthogonal polarizations at the same optical wavelength with negligible additional cost. The de-multiplexing of PolMux and MIMO is realized by using DSPs. The contributions of this section are summarized as follows:

a) For the first time, the concept of an IFiWiN gateway and the corresponding architecture addressing the issues discussed above is proposed with a polarization multiplexing and optical heterodyne (PolMux-OH) scheme;

b) A theoretical model of MIMO-OFDM signals in the proposed scheme is established to analyze their properties;

c) The proof-of-concept experiment verifies the concept of the proposed IFiWiN architecture. It comprises a PolMux-OH scheme with a data rate of 61.3Gb/s. In addition, it also demonstrates the effectiveness of adopting DSP for phase noise compensation and de-multiplexing of PolMux and MIMO;

d) Currently the highest spectral efficiency for the PolMux-OH systems with OFDM signals is 3.41 bit/s/Hz [52] to the best of our knowledge. In our work, a new record-breaking spectrum efficiency (6.82 bit/s/Hz) is achieved.

In Section 2.5.1, we describe the network architecture of the proposed hybrid fibre-wireless indoor network, where the PolMux-OH scheme is employed. Then the operation principle of the PolMux-OH scheme is detailed and the corresponding theoretical model is presented in Section 2.5.2. Section 2.5.3

presents the proof-of-concept experimental setup and results for the proposed PolMux-OH scheme. Finally, conclusions are presented in Section 2.5.4.

2.5.1 System architecture

The proposed indoor hybrid fibre-wireless network architecture is shown in Figure 2.8. The baseband data of users are delivered from the central offices (CO) to the gateway (GW) of a densely-populated region (e.g. central business district, or dense residential district). At the GW, the baseband DSP (e.g. OFDM (de)-modulation) for users' data, and the protocol processing are performed. The processed baseband electrical signals are then modulated onto different wavelengths assigned for the respective destinations (e.g. residential or commercial buildings). All functions except for frequency up-conversion are located at the gateway. Since the equipment for such functions is centralized in the gateway, the capital expenditures (CAPEX) and operational expenditure (OPEX) can be significantly reduced. A star topology can be adopted between the gateway and the buildings with dedicated fibre connections due to the short distances (~1 km). Depending on the capacity demand, a set of wavelengths (λ-set) can be allocated to the home communication controllers (HCCs) of different houses. As shown in Figure 2.8, inside the HCC, the set of arrived wavelengths (λ-3, λ-4) pass through an optical circulator (Cir1) and coupled with the optical local oscillator signals (λ-3b, λ-4b) via an optical coupler (OC). λ-3b, λ-4b are generated from two tunable lasers. The coupled optical signal

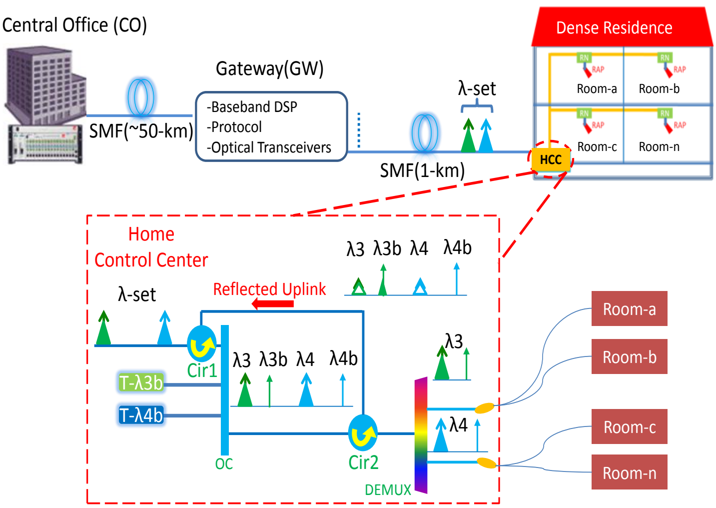

Figure 2.8 Principle of the hybrid fibre wireless indoor networks based on the optical heterodyne techniques.

pairs (λ-3/3b, λ-4/4b) travel toward the second optical circulator (Cir2). Both Cir1 and Cir2 are used to separate the forward and reflected signals for bi-directional operations. Finally, the optical signal pairs are delivered to different destination rooms via a WDM-tree fibre network using a wavelength de-multiplexer (DEMUX). In principle, a point-to-point or even a dynamic network can be employed to provide more capacity. This architecture is scalable and all wavelengths can be used since there are dedicated optical fibre connections from each HCC to the gateway. As shown in Figure 2.8, the sets of λ-3/3b and λ-4/4b are then conveyed to room-a/b, and room-c/d, respectively. The up-conversion of the baseband signal carried on λ-3/4 can be realized through the beatings between λ-3 and λ-3b, or between λ-4 and λ-4b as detailed in Section 2.5.2. By tuning the wavelengths of λ-3b and λ-4b, the frequency of the generated mm-wave can be flexibly adjusted to satisfy the dynamic spectral allocations. In principle, the optical local oscillators can be located in the gateway. Here we place them in the HCC since they can be integrated with polarization beam splitters and PDs in a single chip. The signaling for protocol control between the gateway and the HCC can be distributed by using the low frequency detection methods as we will discusse in 0 in [53, 54].

2.5.2 Operation principle of polarization-multiplexing heterodyne

The operation of polarization division multiplexing optical heterodyne is shown in Figure 2.9. A continuous wave (CW) laser source with single polarization at 45 ° with the polarization beam splitter (PBS1) are separated equally into two optical orthogonal polarization carriers (X-Pol., Y-Pol.) at the same wavelength. Two streams of data (Data-x, Data-y) are modulated onto the two optical carriers via two intensity modulators (IM-x, IM-y). After data modulation, the two optical signals are combined via a polarization beam combiner (PBC). Their optical spectrum is shown in Figure 2.9(c). Over a span of single mode fibre, the two polarizations of the transmitted signals are then separated into two branches via PBS2. The two polarizations of optical local oscillator (OLO) are split into two branches as well. The spectrum of the optical local oscillator before PBS3 is shown in Figure 2.9(d). The separated optical signals are then coupled with the separate OLO via optical couplers (OC1, OC2) for OH process. Due to the fibre transmission induced polarization rotations, crosstalk occurs for both polarizations as shown in Figure 2.9(e)-(f). After the OH process, the generated wireless signal will be broadcasted over a 2-by-2 MIMO antenna subsystem as shown in Figure 2.9. The delivered wireless signals are then retrieved in the mobile device (MD). The operation principle of OH is shown in Figure 2.9(a) and (b). The optical carrier at the frequency of ω_0, with the users data modulated, is shown as the black triangle in

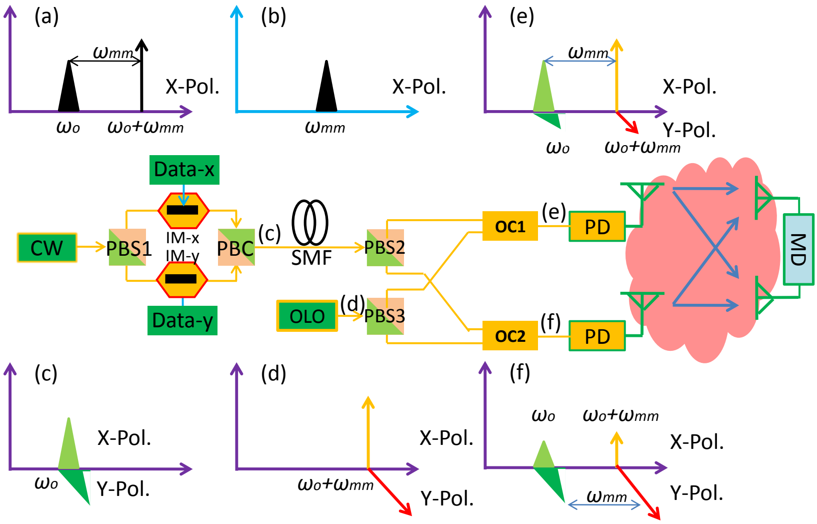

Figure 2.9 Operation principle of optical heterodyne for (a) single polarization and (b) polarization multiplexing; (c) and (d) are spectrum for data modulated optical carrier (DMOC), and optical local oscillator (OLO) with DMOC for single polarization; (e)-(f) are corresponding ones for dual polarizations.

Figure 2.9(a). It can be written as:

$$S_d(t) = E_0 S_e(t) \exp(j\omega_0 t + \rho_0(t)) \tag{2.9}$$

where E_0 is the amplitude of its E-field, $S_e(t)$ the users' data, and $\rho_0(t)$ the phase noise. The OFDM signal (users' data) can be expressed as,

$$S_e(t) = \sum_{k=0}^{N-1} C_k \exp(jk\Omega t) \tag{2.10}$$

where C_k is the complex data modulated on each subcarrier of an OFDM symbol, and Ω is the frequency of the 1st subcarrier. Then, the modulated optical signal can be re-written as,

$$S_d(t) = E_0 \sum_{k=0}^{N-1} C_k \exp(jk\Omega t) \exp(j\omega_0 t + \rho_0(t)) \tag{2.11}$$

In Eq. (2.11), the modulation depth is neglected without loss of generality.

After a span of single mode fibre transmission, the transfer function of the fibre dispersion for L-km length fibre can be expressed as,

$$H(\omega) = \exp\left(j\frac{1}{2}\beta_2 L\omega^2 \right) \tag{2.12}$$

The resulting optical signal can be written as,

$$
\begin{aligned}
S_{d2}(t) &= E_0 S_{e2}\exp(j\omega_0 t + \rho_0(t)) \\
S_{e2} &= \sum_{k=0}^{N-1} C_k \exp(jk\Omega t + j\frac{1}{2}\beta_2 L k^2 \Omega^2)
\end{aligned}
\tag{2.13}
$$

Note that the dispersion only introduces phase rotation to the resulting optical signal as shown in Eq. (2.13). Such phase rotation can be compensated for by using a one-tap equalizer in the frequency domain. The OLO at the frequency of $\omega_0+\omega_m$ can be expressed as:

$$
S_{LO}(t) = E_1 \exp\left[j(\omega_0+\omega_m)t + \rho_1(t)\right] \tag{2.14}
$$

where E_1 is the amplitude of its E-field, $\rho_1(t)$ is the phase noise of OLO. The optical signal and OLO signal are coupled as the spectrum shown in Figure 2.9(a). The coupled signal is then launched into a PD for OH. After that, the users' data will be up converted to a millimeter wave (mm-wave) carrier at frequency of ω_m. The resulting electrical signal can be expressed as:

$$
\begin{aligned}
S_h(t) &= \frac{1}{2}\mu\left[S_{d2}(t)+S_{LO}(t)\right]\times\left[S_{d2}(t)+S_{LO}(t)\right]^* \\
&= \mu\frac{E_0^2 S_{e2}^2(t)+E_1^2}{2} + \mu E_0 E_1 S_{e2}(t)\cos(\omega_m t + \rho_1(t) - \rho_0(t))
\end{aligned}
\tag{2.15}
$$

where μ is the responsivity of the employed PD. The first item in Eq. (2.15) is the baseband subcarrier to subcarrier mixing interference and the DC component, which will be removed before wireless transmission. Then the generated mm-wave wireless signal can be written as:

$$
\begin{aligned}
S_m(t) &= \mu E_0 E_1 S_{e2}(t)\cos(\omega_m t + \rho(t)) \\
\rho(t) &= \rho_1(t) - \rho_0(t)
\end{aligned}
\tag{2.16}
$$

It is clear that the resulting signal is linear for the users' data. The dispersion-induced frequency selective fading is not observed in Eq. (2.16). The phase noise $\rho(t)$ is the sum of $\rho_0(t)$ and $\rho_1(t)$. For the PolMux-OH, we can model the channel by a unitary 2×2 matrix R, and the resulting signals can be written as:

$$
\begin{aligned}
\begin{pmatrix} S_{mx}(t) \\ S_{my}(t) \end{pmatrix} &= \mu E_0 E_1 R \begin{pmatrix} S_{e2x}(t)\cos(\omega_m t + \rho(t)) \\ S_{e2y}(t)\cos(\omega_m t + \rho(t)) \end{pmatrix} \\
R &= \begin{pmatrix} \cos(\theta) & e^{-j\varphi}\sin(\theta) \\ -e^{-j\varphi}\sin(\theta) & \cos(\theta) \end{pmatrix}
\end{aligned}
\tag{2.17}
$$

where $S_{e2x}(t)$ and $S_{e2y}(t)$ denote the two independent data streams, and 2θ and φ are the azimuth and elevation rotation angles of the polarization states, respectively. Over the 2×2 MIMO antenna subsystem, we can model the wireless channel by a 2×2 matrix H, and the signal can be further written as:

$$\begin{pmatrix} S_1(t) \\ S_2(t) \end{pmatrix} = \begin{pmatrix} h_{xx}(t)\otimes S_{mx}(t) + h_{xy}(t)\otimes S_{my}(t) \\ h_{yx}(t)\otimes S_{mx}(t) + h_{yy}(t)\otimes S_{my}(t) \end{pmatrix}$$
$$H = \begin{pmatrix} h_{xx}(t) & h_{xy}(t) \\ h_{yx}(t) & h_{yy}(t) \end{pmatrix} \tag{2.18}$$

Since the impulse response length of H is much larger than R in the indoor scenario, the inter-symbol interference can be eliminated as long as the cyclic prefix of an OFDM symbol is longer than the impulse response length of H. Then, the de-multiplexing of MIMO and PolMux can be performed with a single-tap 2×2 equalizer for each subcarrier after the operation of fast Fourier transform (FFT). PolMux does not introduce any extra computational complexity to the existing process.

2.5.3 Experimental PolMux-OH system and results

Figure 2.10 shows the experimental setup for the proposed hybrid fibre-wireless indoor network system with OH and PolMux. At the optical transmitter, the 14.5 dBm optical carrier at 1557.04 nm, with >100 kHz

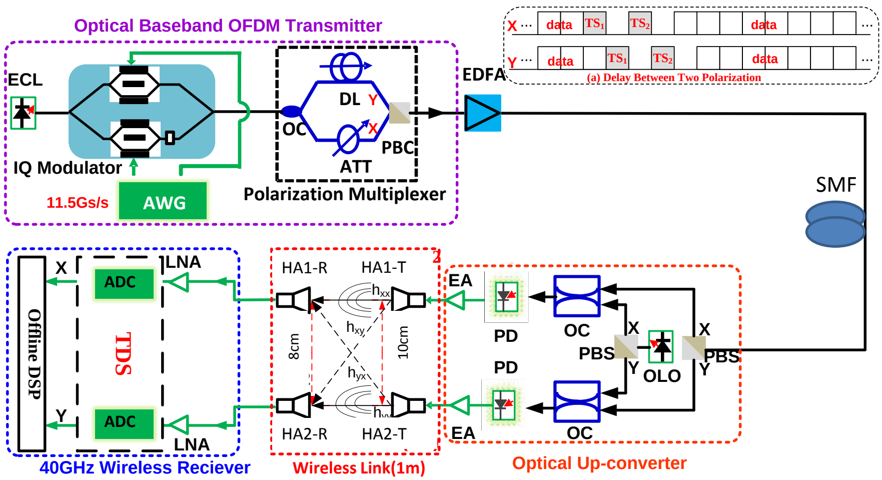

Figure 2.10 The experimental setup of the proposed hybrid fibre wireless indoor network system with 61.3 Gbps MIMO-OFDM signal transmission at 40 GHz. AWG: arbitrary waveform generator; ECL: external cavity laser; OC: optical coupler; ODL: optical delay line; ATT: optical attenuator; PBC: polarization beam combiner; EDFA: erbium doped fibre amplifier; SMF: single mode fibre (100 m); PBS: polarization beam splitter; OLO: optical local oscillator; PD: photo-diode; EA: electrical amplifier; HA1/2-T: transmitter horn antennas at 40 GHz; HA1/2-R: receiver horn antennas at 40 GHz; LNA: low noise amplifier; TDS: real time oscilloscope.

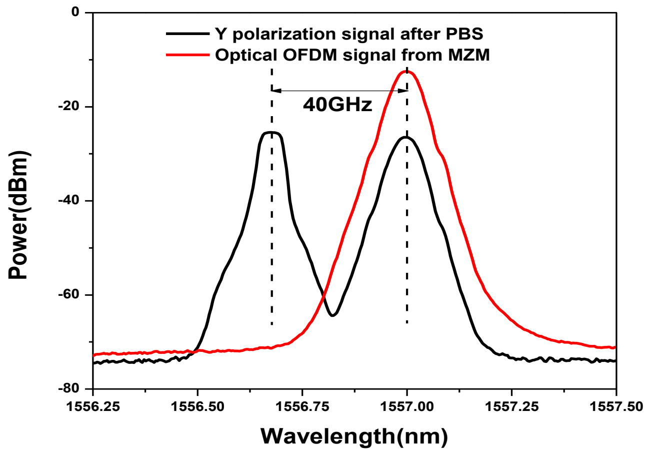

Figure 2.11 Spectrum of received optical signal and optical local oscillator at the y-branch.

linewidth, is emitted from an external cavity laser (ECL). It is modulated by an in-/quadrature- phase (IQ) modulator driven by I and Q branches of a baseband electrical OFDM signal. Such signal is generated by an arbitrary waveform generator (AWG) which serves as a DAC (digital to analog converter). Its sampling rate is set to 11.5 GSa/s. The inverse fast Fourier transform (IFFT) size is 256. Among the 256 subcarriers, 192 subcarriers are allocated for data modulations with QPSK, and 8 subcarriers are used as pilots for phase noise compensation. The 1st subcarrier is set to zero to eliminate the DC component and the 55 highest frequency subcarriers are reserved (not used) for the frequency guard interval. After the IFFT process, the cyclic prefix (1/8 of OFDM IFFT size) is added in front to form a data OFDM symbol. Two types of training sequences (TSs) are added in front of the data OFDM symbols as shown in Figure 2.10. The first type includes only one TS used for the time synchronization and the frequency synchronization (frequency offset compensation). The other one comprises one TS symbol surrounded by two null symbols in order to construct a pair of time interleaved TSs used for MIMO channel estimations. For the optical OFDM modulation, two MZMs of both I and Q branches inside the IQ modulator are biased at the null point of their power transfer curves. The phase difference between the I and Q branches is set to $\pi/2$. The PolMux scheme comprises a polarization beam splitter (PBS) to separate the modulated optical signal into two branches. An optical delay line (ODL) is employed to remove the correlation between the x- and y-polarization by providing one symbol delay (25.04 ns). An optical attenuator is used to

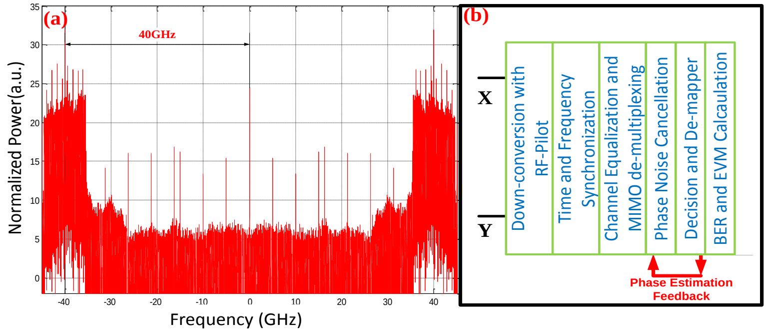

Figure 2.12 Electrical Spectrum of the received 40GHz OFDM signal at HA-1R and (b) detailed offline DSP.

balance the power of the two branches before they are combined via a polarization beam combiner (PBC).The total transmission bit rate is 61.3 Gb/s (11.5 GSaps×192/288×2×4) after PolMux. The bandwidth of the OFDM signal is 8.98 GHz (200/256×11.5≈8.98 GHz), and the corresponding spectral efficiency is 6.82 bit/s/Hz. The generated signal is amplified by an Erbium-doped fibre amplifier (EDFA) to compensate for the insertion loss. The amplified signal with 0-dBm optical power is launched into 1 km SMF-28.

In the optical up-converter, the wavelength of the OLO is set to 1556.72 nm in order to keep the 40 GHz spectral separation from the received optical signal. As shown in Figure 2.11, the red line denotes the optical spectrum after the IQ modulator. The black line denotes the optical spectrum after the polarization beam combiner of y-branch. We can clearly see that the spectral separation between the received optical signal and the OLO signal is 40 GHz. The linewidth of OLO is less than 100 kHz. Two PBSs and two optical couplers (OCs) are applied to realize the polarization diversity for the following OH process. The x- and y-polarizations of both the OLO and the received optical signal are separated into two branches via PBSs. For a convenient notation, we define the branch connected to transmitter antenna HA1-T as x-branch and HA2-T as y-branch as shown in Figure 2.10. Then the x-branch (or y-branch) of the OLO and the received optical signal are coupled before being launched into the following PDs. Both branches comprise the optical components from x- and y-polarizations of the modulated MIMO-OFDM signal due to the polarization rotation. Two PDs with 45 GHz -3 dB bandwidth and 7.5 dBm injected optical input are used for the OH process to directly up-convert the arrived baseband MIMO-OFDM signal onto 40 GHz mm-wave carriers at both x- and y-branch. The up-converted signals, amplified by two 40 GHz narrowband electrical amplifiers (EAs) are fed into a 2×2 MIMO wireless link as shown in Figure 2.10.

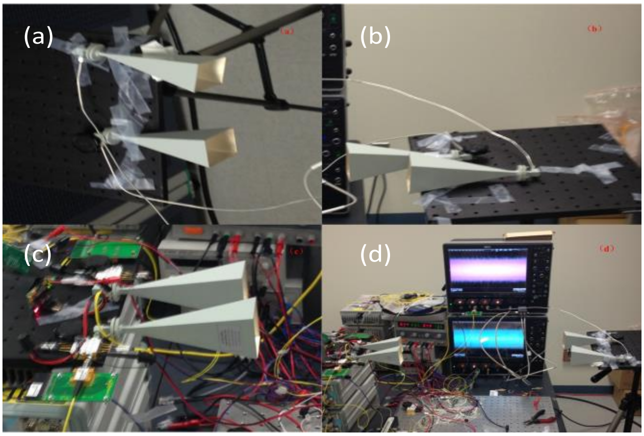

Figure 2.13 Photos of the 40-GHz wireless sub-system, (a)-(b): transmitter antennas (c): receiver antennas; (d): overall of both the transmitter and receiver sides.

The photos of the transmitter horn antennas (HA1-T/-2T) in the MIMO wireless link are shown in Figure 2.13(a) - (b). The receiver antennas are shown in Figure 2.13(c). The overall 2×2 MIMO wireless link is shown in Figure 2.13(d). The four engaged horn antennas are the same, each with 25 dBi gain and >15 GHz bandwidth at 40 GHz. The forward distances between transmitter antennas and receiver antennas (HA1-T to HA1-R, and HA2-T to HA2-R) are both 1 m, as shown in Figure 2.13(d). To emulate the wireless MIMO crosstalk, the 1 cm forward offsets between HA1-T and HA2-T, and between HA1-R and HA2-R are intentionally set as shown in Figure 2.13(a). Similarly, the lateral separations between HA1-T and HA2-T, and that of HA1-R and HA2-R are set to 8 cm and 10 cm, respectively. Two band-pass low noise amplifier (LNA) are used to boost the 40 GHz MIMO-OFDM signal from HA1-R/-2R with a noise figure less than 5 dB. Digital down conversion is employed to retrieve the 61.3 Gb/s MIMO-OFDM signal from the 40 GHz carrier. The RF spectrum of the signal from HA1-R is shown in Figure 2.12(a). The ADC is realized using a real-time oscilloscope with a 120 GSa/s sampling rate and 45 GHz electrical bandwidth. The detailed DSP for the MIMO-OFDM de-multiplexing, demodulation and BER calculation is shown in Figure 2.12(b). First, the mm-wave MIMO-OFDM signals in x- and y-branches are digitally down converted to baseband signals. Second, the time synchronization and the frequency synchronization are realized based on one conjugate symmetric OFDM TS symbol. The MIMO channel response, including the wireless MIMO crosstalk, and the crosstalk induced by the polarization rotation and the polarization mode dispersion is explored from the pair of time interleaved TS symbols. Third, the FFT process is used to transform the received OFDM signal into the frequency

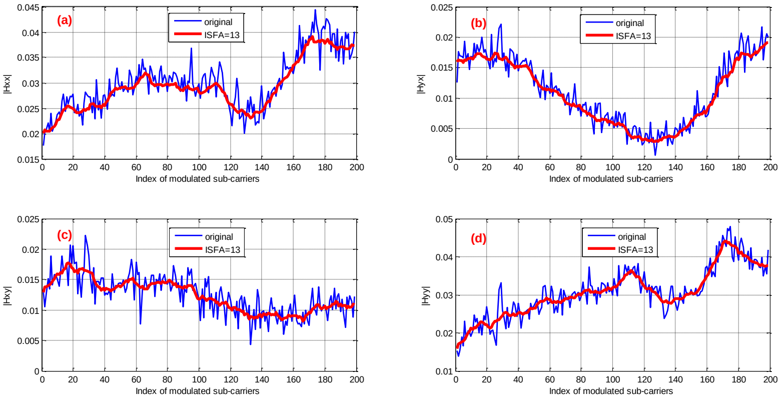

Figure 2.14 Channel estimation of the 2x2 MIMO matrix with ISFA for (a) Hxx, (b) Hyx, (c) Hxy, (d) Hyy.

domain. In the frequency domain, the de-multiplexing is implemented based on a one-tap zero-forcing equalizer defined with the exploited MIMO channel responses. Fourth, the common phase error compensations (phase recovery) in the two branches are realized based on the inserted pilots with a decision feedback algorithm. Finally, the BER (bit error rate) and the EVM (error vector magnitude) are evaluated. BER is calculated by error counting with 1×10^6 bits measured. The EVM is calculated as shown:

$$EVM = \sqrt{\sum_{k=1}^{N}(i_k - I_k)^2 + (q_k - Q_k)^2 \Big/ \sum_{k=1}^{N}(I_k^2 + Q_k^2)} \qquad (2.19)$$

where I_k and Q_k are retrieved I and Q components while Ik and Qk are the reference ones.

The intra-symbol frequency-domain averaging (ISFA) algorithm [55] is employed here to improve the estimation accuracy of the 2×2 MIMO channel matrix. Since only one pair of TSs are used to implement the channel estimation in time domain, the ISFA can efficiently remove the unwanted noise with frequency domain averaging. The original elements of the estimated 2×2 MIMO matrix are displayed in Figure 2.14 as the blue line. The estimated channel coefficient without the ISFA exhibits high-frequency fluctuations due to the presence of Inter Carrier Interference (ICI) introduced by the phase noise, and with ISFA, the ICI-induced high-frequency fluctuations can be removed significantly. In our experiment, the number of the subcarriers used for ISFA is optimized to 13. Figure 2.15 shows constellations of retrieved MIMO-OFDM signals with 1-km fibre transmission and 1-m wireless delivery at 24 dB OSNR (optical signal to noise ratio). The digitally down-converted x- and y-branch OFDM signals before the MIMO de-multiplexing are shown in Figure 2.15(a)

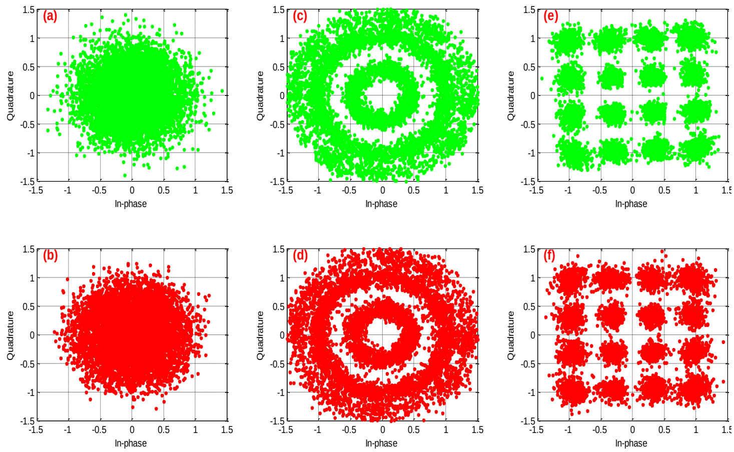

Figure 2.15 Constellations of 61.3Gbps MIMO-OFDM signals at 40GHz mm-wave after 1-km fibre transmission and 1-m wireless delivery with the OSNR at 25-dB. For x-branch: (a) before polarization de-multiplexing, (c) polarization de-multiplexed, (e) phase recovery. For y-branch: (b), (d), and (f), correspondingly.

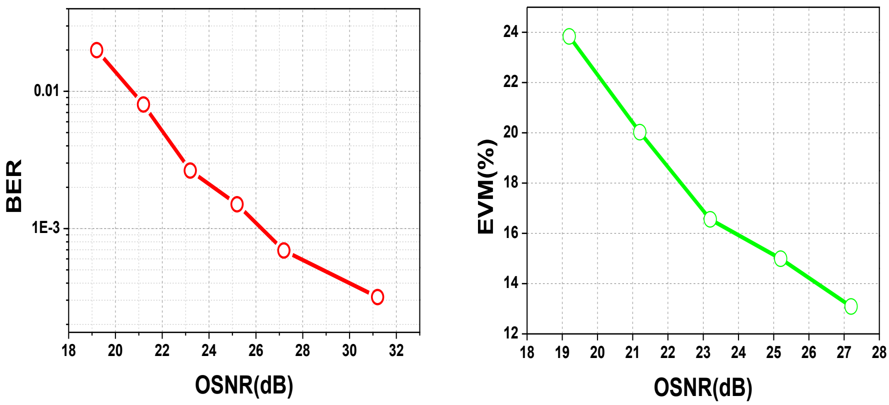

Figure 2.16 The measured BER and EVM versus OSNR.

and (b), respectively. It is obvious that the MIMO crosstalk introduces severe distortions. After MIMO de-multiplexing, the resulting constellations are shown in Figure 2.15(c) and (d). These retrieved vectors are distributed among multiple circles due to the phase noise induced phase ambiguity. After the phase recovery, the retrieved vectors are converged to their corresponding constellations as shown in Figure 2.15(e) and (f). The measured EVM versus

OSNR (0.1 nm resolution) is depicted for the 61.3 Gb/s MIMO-OFDM signal with 1 km fibre transmission and 1 m wireless delivery. Since the performance difference between with and without fibre transmission is observed to be very small, we only present the results of fibre transmission here. Both the BER and the EVM curves are shown in Figure 2.16. They both show that the system performance improves as the OSNR increases. The slope of the system performance decreases as the OSNR increases most likely because the additional Gaussian noise is not predominant when the SNR achieves a certain level. An adequate BER for the outer FEC threshold (less than 3.8×10^{-3}) is achieved at the 22 dB OSNR. The potential factors for the limited BER and the EVM performance are the DAC/ADC, especially the limited effective number of bits, and the imperfect algorithm to compensate the phase noise induced ICI in the experiment. These limitations can be mitigated with the rapid improvement of commercial DAC/ADCs, and with the adoption of powerful phase noise compensation algorithms.

2.5.4 Conclusion

For the first time, a novel hybrid fibre-wireless indoor network has been experimentally demonstrated which can deliver a 61.3 Gb/s MIMO-OFDM signal over 1 km SMF-28 fibre and 1 m wireless link at 40 GHz. A BER at the outer FEC threshold (less than 3.8×10^{-3}) is achieved at the 22 dB OSNR. Thanks to optical heterodyne (OH) and polarization multiplexing (PolMux), the high-speed mm-wave MIMO-OFDM signal can be delivered in a simple hybrid fibre-wireless indoor network with many merits. Based on the achieved experimental results, it is believed that the proposed system is attractive for future high-speed wireless communications in indoor scenarios.

2.6 Summary

In this chapter, two main categories of signals are discussed for which three main functions of the IFiWiN gateway are described, namely flexible-reach data delivery, convenient frequency up-conversion, and versatile indoor exchange functions. Three different IFiWiN gateways are proposed and investigated. The remote up-conversion and indoor exchange functions have been demonstrated.

Chapter 3 Optical Delay Techniques for Radio Beam Steering

As a key enabling technique for future wireless communications, radio beam shaping and steering can be effectively realized by means of a phased array antenna, which deploys a multitude of antenna elements where beam steering/shaping is done by tuning the phase difference between the antenna elements. It keeps a unique status since it is beneficial for increasing channel capacity and for reducing radio radiation power. Due to limited power leaked to other spatial channels, the complexity of digital signal process can be lowered. In this chapter, the background of optical delay techniques for radio beam steering is first reviewed in Section 3.1. The optical radio beam steering is explored in two-fold. In the operation principle level, a new optical true time delay concept named cyclic additional optical true time delay is proposed and studied for flexible beam steering and spectral filtering in Section 3.2. In the implementation level, a compact, fabrication-tolerant photonic integrated circuit design and its realization are studied in Section 3.3 for a silicon-on-insulator and in Section 3.4 for a Indium Phosphide (InP) platform.

3.1 Review of radio beam steering techniques

3.1.1 Beam steering, phased array antenna and true time delay

The current explosion of communication traffic volume is driven by an insatiable appetite for high speed internet connectivity and video-based content delivery to wireless and mobile terminal users, especially for indoor scenarios. A lot of research has been carried out to expand wireless capacity. In the spatial domain, spatial multiplexing (e.g. MIMO), spatial isolation (pico/femto-cells), and spatial filtering (beam-steering) attract lots of attention due to their abilities to boost capacity strongly. Spatial isolation requires many wireless access points and its successful deployment depends on the actual structure of a building. These features limit its applications. Unlike spatial multiplexing which requires complicated digital signal processing, beam steering (BS) directs signals to the desired user with minimum interference. Phased array antennas (PAAs) are widely considered as the best candidate for microwave beam-steering/-shaping due to their fast operation and compactness [56]. The operational bandwidth of a conventional PAA is limited. Specifically, a severe limitation is often caused by the use of phase shifters to scan the beam, which results in beam deformations ("squint") in the measured antenna pattern. The use of true time delay (TTD) technology potentially eliminates such bandwidth restriction, as it provides a theoretically frequency-independent time delay on each channel of the array [57]. Standard TTD technology typically consists of digitally-switched electrical transmission line sections wherein weight, loss and cost increase rapidly with increased operational frequency and/or phase tuning resolution. These issues can be avoided by adopting optical TTD radio beam steering (OTTD-RBS) techniques as reported in [58-61]. Currently, the trend is clear that the OTTD-RBS systems are moving to the integrated solution. In the following, we will review the integrated solutions of OTTD-RBS.

3.1.2 Photonic integrated circuit for Radio beam steering

An integrated optical tunable delay line (OTDL) for OTTD-RBS is a key step towards the practical implementation of beam-steered RoF systems. Historically there are two main approaches to realize the integrated OTDLs, the first kind is based on physical length induced delay [62-64], and the second kind is based on optical filtering induced group delay [65-69].

As a representative example of the first kind, an optical radio beam steering chip with wavelength (de-)multiplexer, discrete delay lines and MZI-switch was proposed by F. Soares et al. in [63]. In this chip, an arrayed waveguide grating (AWG) is used as a (de-)multiplexer for separated wavelength operation. Delays for different antennas are generated on a wavelength basis as a whole and then step-wise tuned by a 3-stage MZI-switch. In general, the first kind of integrated OTDLs can provide broadband but step-wise tunable delays. The angular resolution of radio beam-steering then depends on the number of steps.

Different from the first kind of approach, the second one can provide continuous tuning of the group delay mostly based on the all-pass filter. C. K. Madsen et al. explored the possibility to use optical ring resonators (ORRs) as all-pass filters [68, 69] and an elegant theoretical analysis framework based on a digital filter concept was proposed [70]. Later, L. Zhuang et al. demonstrated a prototype of integrated OTDLs of multiple ORRs [65]. However, the second kind of approach suffers the narrow operation bandwidth limited by the inherent feature of filter resonance. Cascaded ORRs can overcome such limitation to some extent but with the sacrifice of large chip area and later complicated trimming [71].

In subsequent summary, the first kind of integrated OTDLs are suitable for broadband applications with low angular resolution, while the second one matches narrowband applications desiring relatively higher angular resolutions. The indoor communications are usually with very high throughput and limited space (thus the low angular resolution), which makes the first kind of integrated OTDL suitable for such applications. The main study topic for this thesis is the first kind of OTDL.

3.2 Cyclic additional optical true time delay

As discussed in Section 3.1, OTTD-RBS in the RoF can provide spatial filtering (e.g. beam-steering/-shaping) to improve the signal quality and to boost the capacity. Moreover, for indoor networks, there are many different wireless services at different frequency bands. Indoor RoF systems are expected to operate at different frequency bands to support different wireless services, which imply that dynamic spectrum allocation in wireless communications is highly desired. Therefore, both spatial filtering and spectral filtering are required in these systems. Motivated by these facts, a novel broadband radio beam steering scheme with tunable microwave filtering is proposed based on cyclic additional optical true time delay (CAO-TTD). Compared with traditional OTTD, CAO-TTD introduces negligible additional complexity. By including this low loss extra optical delay, spectral filtering of the RF signal can be achieved.

3.2.1 Principle of cyclic additional optical true time delay

The principle of OTTD is depicted in Figure 3.1. An RF signal is generated by mixing a microwave LO and a data signal. The RF signal is modulated onto an optical carrier via an optical intensity modulator ('IM') and then fed to the optical delay network ('ODN'). The optical delay network includes two branches. The left one is delayed by an optical true time delay (OTTD) which can be implemented as an optical waveguide of specific length. The modulated optical signal can be expressed as:

$$S_o(t) = E_o(1+\gamma S_e(t))\exp(j\omega_o t) \qquad (3.1)$$

where E_o is the amplitude of the optical carrier, ω_o its angular frequency, γ the modulation depth, and $S_e(t)$ the microwave signal. The replica of the optical signal passes through the OTTD with negligible dispersion. The delayed signal can be written as:

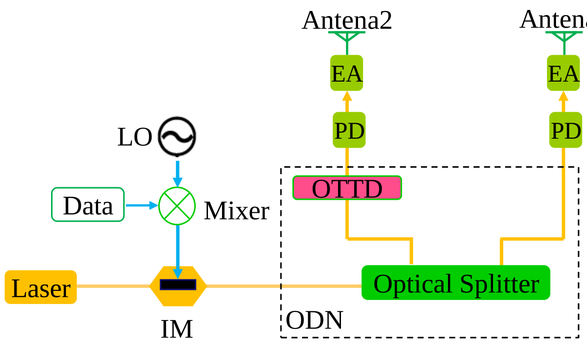

Figure 3.1 Principle of optical true time delay.

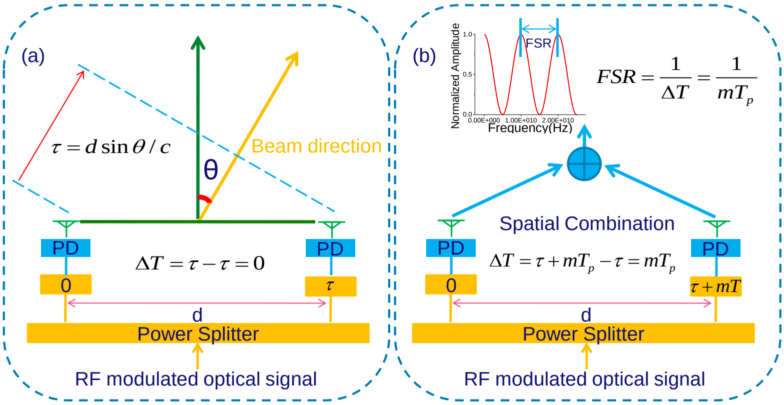

Figure 3.2 Principle of microwave phase antenna array based on cyclic additional optical true time delay (CAO-TTD).

$$S_o(t) = E_o(1+\gamma S_e(t-\tau))\exp(j\omega_o(t-\tau)) \tag{3.2}$$

where τ denotes the delay. The output optical signals are then converted back to the RF signals via photo-diodes (PDs). The detected signal can be written as:

$$S_d(t) = R_d\left|S_o(t)\right|^2 = \underset{DC}{R_d E_o^2} + \underbrace{2R_d\gamma E_o^2 S_e(t-\tau)}_{signal} + \underbrace{R_d\gamma^2 E_o^2 S_e^2(t-\tau)}_{beating} \tag{3.3}$$

where R_d is the responsivity of the engaged PDs. It can be seen that the signal term and the beating noise term both exist in the detected signal. For microwave signals modulated on optical carriers, the frequency of beating component is usually twice as high as the microwave signals, and thus the beatings component can be easily filtered out. The DC component will be blocked by the antennas and electrical amplifiers ('EA'). Thus the signal broadcasted from the antennas can be written as:

$$S_d(t) = \underbrace{2\mu\gamma E_o^2 S_e(t-\tau)}_{signal} \tag{3.4}$$

It is clear that the detected microwave signal has been delayed. This will result in the beam steering in the system. Since the microwave delay is exactly the same as the OTTD, in the following discussion, the OTTD PAA will be analyzed using the traditional PAA theory. The optical delays are transformed into equivalent microwave phase shifts (PSs), which will shape and steer the microwave beam. For a uniform linear array shown in Figure 3.2(a), the array factor (*AF*) with OTTD can be generally expressed as:

$$AF(\theta, f) = \sum_{l=0}^{L-1} A_l \exp\left[j\frac{2\pi fld}{c}(-\sin\theta + \frac{c\tau}{d}) \right] \tag{3.5}$$

where θ is the observing angle as shown in Figure 3.2(a), f is the frequency of the microwave signal, L is the number of element antennas, d and τ are the distance and time delay between the two adjacent antenna elements, and A_l is the amplitude coefficient of element radiator ($A_l = 1$ for a uniform linear array). The array factor can be further optimized if proper amplitude weights are added. As shown in Figure 3.2, τ is the propagation delay between the beams from two adjacent element antennas. According to Eq. (3.5), the maximum value of AF is achieved when the term $(-\sin\theta + c \times \tau/d)$ is equal to zero. In other words, the main lobe of the microwave beam points to the angle θ when τ is equal to $d \times \sin\theta\,/c$.

In the following, the properties of the proposed CAO-TTD are explored. When the delay is introduced with integer multiple periods (mT_p) of the microwave carrier, the AF can be re-written as:

$$AF(\theta, f) = \sum_{l=0}^{L-1} A_l \underbrace{\exp\left[j\frac{2\pi fld}{c}(-\sin\theta + \frac{c\tau}{d}) \right]}_{SpatialFiltering} \times \underbrace{\exp(j2\pi flmT_p)}_{SpectralFiltering} \tag{3.6}$$

where T_p is the period of the microwave carrier, and m is a integer multiple. First we only consider the spatial filtering (m=0). When τ is equal to $d \times \sin(\theta)\,/c$, the first exponential item (spatial filtering item) of Eq. (3.6) obtains its maximum of 1. It means that the main lobe directs to the θ direction for all frequencies. When the spatial filtering item is determined, the value of *AF* is only affected by the second exponential function which is essentially a microwave photonics filter. It is clear that the spectral filtering of the received microwave signal in the θ direction can be controlled by tuning the integer

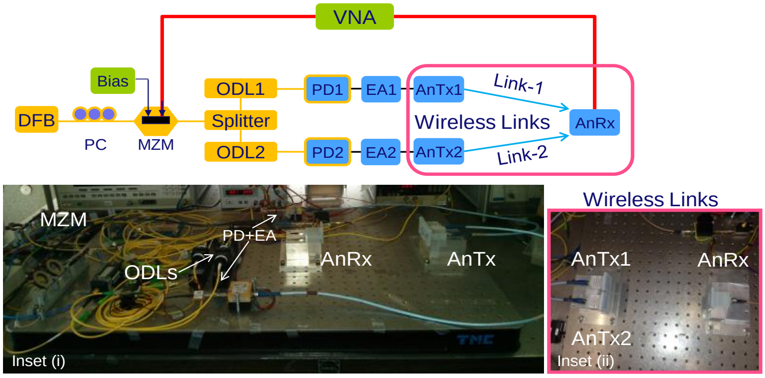

Figure 3.3 The proof-of-concept experimental setup of cyclic additional optical true time delay scheme.

multiple m. The spectral filtering operation is illustrated in Figure 3.2(b). When the main lobe is considered, the RF signals from different element antennas can be combined in the space with $m \times T_p$ difference. The resulting spectral filtering is schematically shown as the Figure 3.2(b), with the free spectral range (FSR) of the microwave filtering equal to $1/(m \times T_p)$. Note that the main lobe of the suppressed frequency (instead of the carrier frequency) directs to other directions rather than θ.

The optical operation of the additional delays introduces negligible power degradation since the optical loss can be very low. The CAO-TTD can be either a path-switch based or dispersion-based scheme and the additional delays for spectral filtering will not add significant complexity.

3.2.2 Experimental setup, results and discussion

The proof-of-concept experimental setup of the CAO-TTD scheme is shown in Figure 3.3. The optical carrier generated from a distributed feed-back (DFB) laser is at 1550.016 nm with 3 dBm power. Via a polarization controller (PC), it is fed into a MZM with 20 GHz -3 dB bandwidth (BW). The MZM is biased at the quadrature point to obtain the maximum linear dynamic range in the case of intensity modulation. The stimulus microwave sinusoidal signal from a vector network analyzer (VNA) is modulated on the optical carrier. The stimulus signal is swept from 7.5 GHz to 12.5 GHz. The modulated optical signal passes through two paths with two tunable optical delay lines (ODL1/2 in Figure 3.3). The ODLs are made by OZ optics (ODL-100) with free space delay and thus the optical length refers to the geometric length. ODL1 is used to compensate the offset delay between the two branches and ODL2 to adjust the optical true time delays for CAO-TTD. The optical signals of the two branches are then

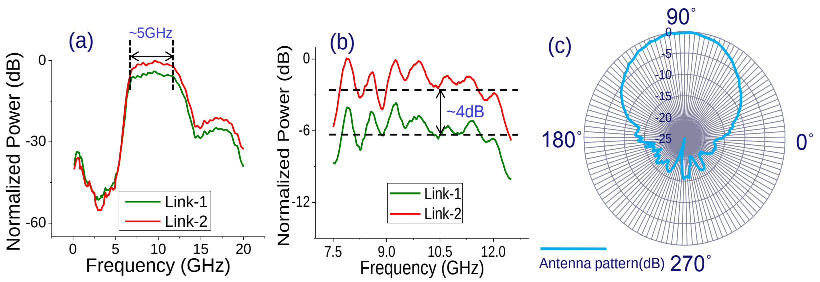

Figure 3.4 The measured transmission curves for (a) 0.13-20 GHz and (b) 7.5-12.5 GHz, respectively; (c) the measured 2-D far field pattern of element antennas.

detected by two 40 GHz -3 dB BW PDs (PD1/2) for the optical to electrical conversion. The detected radio signals are fed into two element antennas (AnTx1/2) of the transmitter PAA via two broadband amplifiers with 12.5 GHz -3 dB BW. AnTx1/2 are identical broadband 10-GHz aperture antennas with 5 GHz -3 dB BW. A photo of the experimental setup is shown in inset (i) of Figure 3.3. The antenna subsystem is shown in inset (ii) of Figure 3.3. AnTx1/2 and AnRx are in a plane (working plane) parallel to the optical table. AnTx1/2 are placed near each other with a 41.5 mm center-to-center distance. The measured mutual coupling between AnTx1 and AnTx2 is less than -20 dB. The microwave beam is steered in the plane parallel to the optical table.

The properties of the antenna subsystem are characterized as shown in Figure 3.4. The transmission curve (S12) of the engaged antennas is measured as shown in Figure 3.4(a). A 5 GHz -3 dB pass-band is observed. The wireless link connecting AnTx1 and AnRx is named ‘Link-1’ as shown in Figure 3.3, and the other is named ‘Link-2’. A 4 dB received power imbalance (PI) of Link-1 and Link-2 is shown in Figure 3.4(b) which will introduce imperfect power suppression ratio (PSR). The PSR can be expressed as:

$$PSR = 10\log_{10}\left(\frac{E_0 + E_1}{E_0 - E_1}\right)^2 = 20\log_{10}\left(\frac{10^{\frac{PI(dB)}{20}} + 1}{10^{\frac{PI(dB)}{20}} - 1}\right) \tag{3.7}$$

The measured 2-D far field pattern (FFA) of the engaged antennas in the working plane is shown in Figure 3.4(c). The -3 dB angle width of the 2-D FFA is 70° (-35° to 35°). The normalized received power of 10 GHz microwave versus optical delays is shown in Figure 3.5(a). Peaks are obtained with 0, 30, 60 mm optical length difference, and two minimum points with 15 and 45 mm optical lengths. It is clear that the received power is periodic versus the optical delay with a 30 mm periodic length (the wavelength of 10 GHz microwave). Therefore the cyclic additional integer multiple of 30 mm optical delay will not affect the beam profile at the carrier frequency. Meanwhile, the 30 mm optical

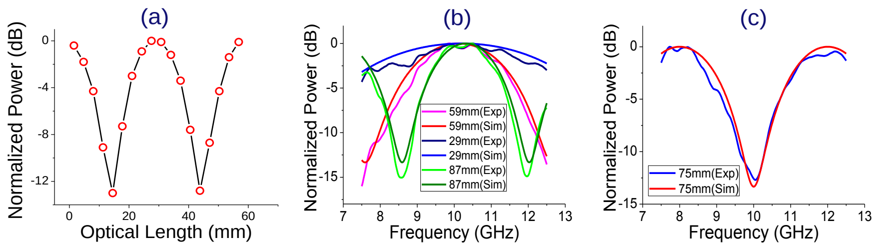

Figure 3.5 (a) Measured RF power vs. optical delays; (b) band-pass filtering at 10 GHz with different optical delays; (c) band-stop filtering at 10 GHz.

delay can cover the whole RBS space. To investigate the spectral filtering phenomenon induced by CAO-TTD, the transmission curves (S12) for different CAO-TTDs are measured and compared with their corresponding simulated results as shown in Figure 3.5(b)-(c). The measured curves have been calibrated to eliminate the frequency ripples of the two wireless links. The measured and simulated curves are then normalized at their max values. Since residual ripples of the measured curves exist, for some comparison sets, the measured curves are a little lower than the simulated ones. In general, good matching between the measured and simulated results is observed. The PSRs for both Figure 3.5(b) and (c) are around -13 dB, which exhibits a very good agreement with Eq. (3.7). The band-pass filtering curves with different optical delays (thus with different FSRs) are shown in Figure 3.5(b). As the optical delay increases, the pass-band and FSR are both suppressed as indicated in Eq. (3.6). This exhibits good configurability for spectral allocations. Three sets of CAO-TTDs with 29, 59, 87 mm optical delay are employed. These delays are chosen close to the integer multiple of the microwave carrier wavelength (30 mm). Therefore, the power of microwave carrier (10 GHz) is not affected by the cyclic additional optical delay as shown in Figure 3.5(b). Such periodic feature is also demonstrated for the band-stop filtering. As shown in Figure 3.5(a), 15-mm optical delay introduces a minimum point at microwave carrier (10 GHz). Then the minimum point is observed at 10 GHz again as shown in Figure 3.5(c) with 60 mm cyclic additional delay.

3.2.3 Conclusion

In Section 3.2, a novel broadband radio beam steering with tunable spectral filtering using cyclic additional optical true time delay (CAO-TTD) is proposed and experimentally investigated. About 13dB spatial and spectral power suppression ratio is achieved in the experiment, which can be further improved given the power balance of two transmitter antennas. With high energy efficiency, and tunable spectral filtering, it is believed that the proposed CAO-TTD is attractive for future wireless communications, especially in the context of RoF networks.

3.3 AWG-loop based optical true time delay line

An arrayed waveguide grating feedback loop (AWG-loop) is generally used as OTDLs. A.M.J. Koonen proposed to use such scheme for remotely-controlled RoF network. To allow advanced features like high resolution operation and interleaved 2-D beam steering, for the first time, he proposed to introduce the spectrally-cyclic AWG-loop (SC-AWG-loop) as the key enabling technique. This make the related research inside this thesis much different from the previous works. These advanced features are detailed in Section 3.3.2 and 3.3.3. The contribution in this thesis is mainly about the realisation and experimental verification of such scheme and the analysis of the measured results.

3.3.1 Concept and benefits of the spectral cyclic AWG-loop

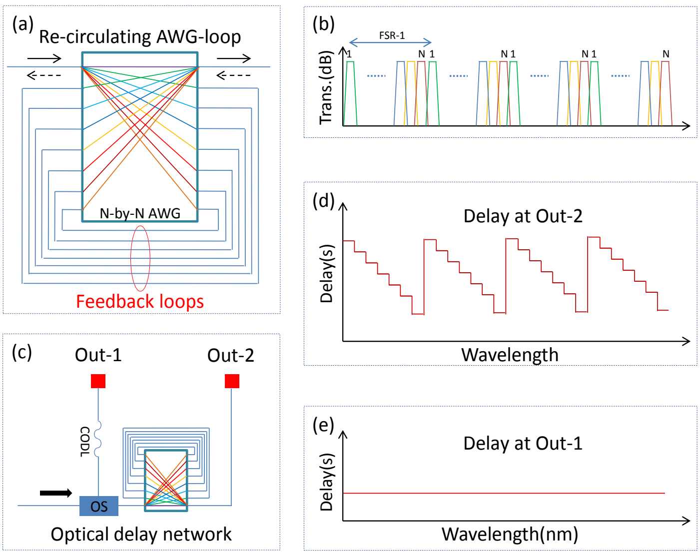

Figure 3.6 The principle of proposed SC-AWG-loop based integrated optical tunable delay line (OTDL), (a) the SC-AWG-loop; (b) the spectral transmission of an N-by-N cyclic AWG; (c) 1-by-2 optical delay network; (d)-(e) the delay at Out-2/-1 of (c). OS: optical splitter.

The proposed integrated SC-AWG-loop is based on a cyclic AWG, which is schematically shown in Figure 3.6. A similar system using a discrete AWG component and fibre delay lines has been demonstrated in [62] for 10-40 MHz operation. Due to its bulky size, such system can only work properly for large delays (and hence for low carrier frequency operation) with low accuracy. There are two main advantages of the proposed integrated SC-AWG-loop towards the previous reported one: the first one is that the integrated SC-AWG-loop with small footprint can yield short delays with high accuracy which suits high-frequency operation like in mm-wave bands; the other one is that the AWG is designed to be cyclic and symmetric which allows flexible interleaved operation and bi-directional operation.

As shown in Figure 3.6(a), the N-by-N symmetric AWG is employed as both wavelength multiplexer (MUX) and de-multiplexer (de-MUX). The AWG is cyclic in optical spectrum with the transmission profiles shown in Figure 3.6(b). The feedback loops (optical waveguides) connect N-1 pairs of inputs and outputs in a symmetric configuration for re-circulating operations and leave one pair of input and output as the input and output of the SC-AWG-loop. This SC-AWG-loop is topologically equivalent to two AWGs in series with different lengths in between, which works as a step-wise OTDL. Figure 3.6(c) shows the implementation of 1-by-2 optical delay array. The optical signal is split into two paths: one directly goes to the first output (Out-1) and the other goes through an SC-AWG-loop unit to the second output (Out-2). As shown in Figure 3.6(d), the delay of Out-2 can be tuned as the signal wavelength changes. The delay of Out-1 is shown in Figure 3.6(e). A compensation optical delay line (CODL) is employed for offsetting the initial delay between Out1/2.

There are some advanced features of the proposed SC-AWG-loop. First, by re-using the same AWG as MUX and de-MUX, its footprint can be significantly reduced (approximately by half). Moreover, its fabrication tolerance is enhanced since the relative spectral mis-alignment between MUXes and de-MUXes does not exist anymore. Third, it can support remote control of optical delays with wavelength tuning, which enables stable and centralized operations by only tuning (or selecting) the wavelength of the optical signals. Fourth, it can simultaneously support bi-directional operation with the symmetric performance. As shown in Figure 3.6(a), the solid and dashed arrows denote west-to-east and the opposite operation respectively. Such operations are highly demanded for systems including up- and down-links. By re-using one device, both the system footprint and its stability can benefit. Finally, the delay resolution of the SC-AWG-loop is scalable because: (a) its spectral cyclic feature allows the interleaved operation of two cascaded SC-AWG-loops with different delay steps; (b) the port count of AWGs can be as many as hundreds.

3.3.2 Cascaded SC-AWG-loop for high resolution delay

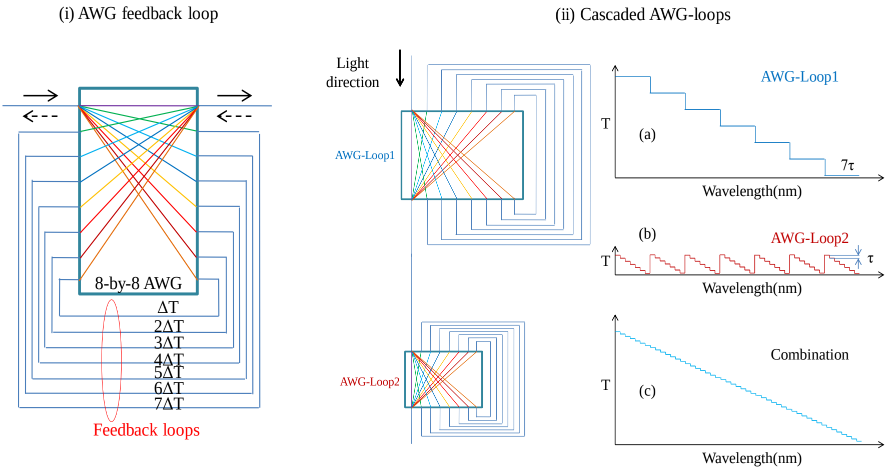

Figure 3.7 Operation principle of cascaded operation of spectral-cyclic arrayed waveguide grating (SC-AWG-loop).

The cascaded operation of SC-AWG-loops can provide high resolution of delays. Figure 3.7 depicts the operation principle of the cascaded operation of SC-AWG-loops. The path selection in a SC-AWG-loop is shown in Figure 3.7(i). For a non-cyclic AWG-loop, its delay resolution can be expressed as: $r_0 = log_2(N-1)$, where N is the number of AWG I/O ports. Its resolution can be as high as 10 since the port count of AWGs can be as many as a thousand [9]. In this case the port count increases exponentially with the resolution. On the other hand, for cyclic AWG-loops, the resolution can be doubled by cascaded configuration. It means that the resolution increases logarithmically with a linear increase of number of AWG I/O ports, which results in a smaller chip footprint. As shown in Figure 3.7(ii), two 7-step cyclic AWG-loops with different delay steps are cascaded. The signal modulated on the optical carrier is delayed first by SC-AWG-loop1 and then by SC-AWG-loop2. Thus the final delay of an optical signal is the addition of the delays in both SC-AWG-loops. The delay step of SC-AWG-loop2 can be written as τ as shown in Figure 3.7(ii). The delay versus wavelength of SC-AWG-loop2 can be found in Figure 3.7(b). Due to the cyclic feature of the SC-AWG-loop2, its delay is periodic in wavelength. To allow the progressive delays, the delay step of SC-AWG-loop1 can be designed as $(N-1)\times\tau$ (here it is 7τ). Its delay versus wavelength is shown in Figure 3.7(a). By combining both SC-AWG-loops, we can obtain the delay curve as a function of wavelength as shown in Figure 3.7(c). We can see

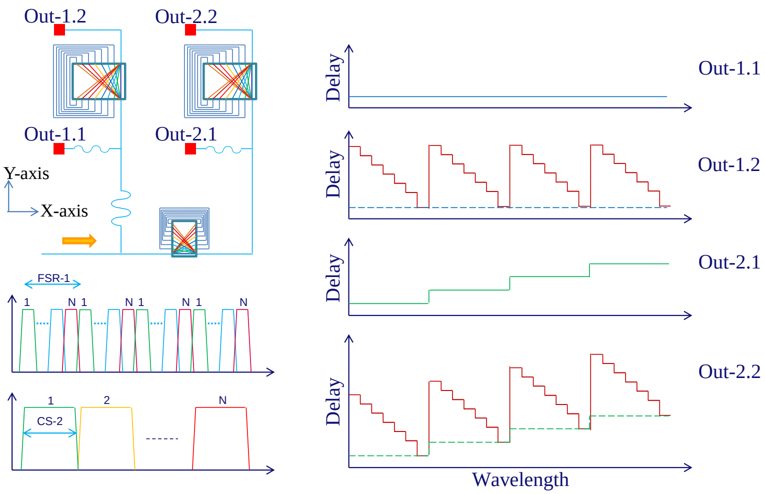

Figure 3.8 Principle of interleaved operation of two types of SC-AWG-loops. PB-2: channel passband of the second type of SC-AWG-loops.

that the combined structure of two SC-AWG-loops can provide $(N-1)^2$ delay steps based on the cascaded configuration. Its resolution can be written as: $r_1 = r_0 + r_0 = 2r_0$, indicating its delay resolution increases linearly with the number of AWG I/O ports.

3.3.3 Interleaved SC-AWG-loop for 2-D beam steering

The interleaved operation of SC-AWG-loops is shown in Figure 3.8. There are two types of SC-AWG-loops (SC-AWG-loop1/2 shown in Figure 3.8) used to form a 2-D OTTD-RBS system. The optical carrier is split into two paths with SC-AWG-loop2 in between. For both paths, two identical SC-AWG-loop1 are used in between. The Out-1.1 and -1.2 are connected to the first path, while the Out-2.1 and -2.2 connected to the second path. The FSR of the first type (FSR-1) is designed equal to the channel passband of the second SC-AWG-loop (PB-2). Thus when the wavelength sweeps inside one FSR-1, the delay difference between Out-1.1 and -2.1 is the same as the one between Out-1.2 and -2.2. This is because the wavelength is within one channel of SC-AWG-loop2, no additional delay is generated before and after SC-AWG-loop2. That means the radio beam is steered in y direction. The x- and y-axes are schematically shown in Figure 3.8. The curves of delay vesus wavelength for different outputs are shown in Figure 3.8. For SC-AWG-loop1, due to the spectral cyclic feature, the delays will be the same after a spectral separation of FSR-1. This will result in the periodic delay values at Out-1.2 as shown in Figure 3.8. When the wavelength jumps one FSR-1 ahead, the delay difference between Out-1.1 and -1.2 is the same as the one between Out-2.1 and -2.2, which results the radio beam steering in x direction. It is clear that when only the wavelength is swept, the radio beam is independently steered in both x and y directions. The x and y directions beam steerings are interleaved as the wavelength increases.

3.4 Silicon-on-Insulator based SC-AWG-loop chip

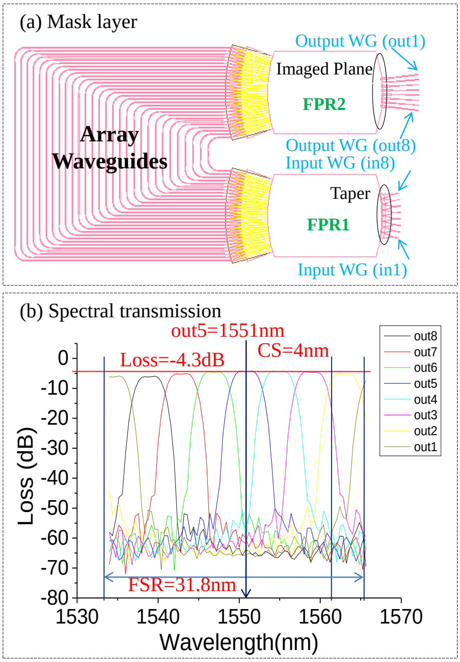

Figure 3.9 The mask layout (a) and simulated spectral transmission of the 8-by-8 cyclic AWG (b).

Silicon photonics technology attracts a lot of attention from both industrial and academic communities due to its low-cost and compatibility to the electronics CMOS platform. Among all silicon photonics techniques, the silicon-on-insulator (SoI) is the predominant one. In this section, the SC-AWG-loop concept realized in the SoI platform is investigated.

3.4.1 Design of Silicon-on-Insulator SC-AWG-loop chip

The device design will be discussed in this section. The device is fabricated on a 200 mm diameter SOI wafer with a 220 nm thick silicon guiding layer on top of a 2000 nm buried oxide layer. To pattern the designs, a 193 nm deep UV lithography and a two-step etch process are utilized. The first etch creates the 220 nm deep trenches for high contrast waveguides and sharp bends. The second 70 nm etch step is for the fibre grating couplers and the shallowly etched waveguides for connecting deeply etched waveguides and free propagation regions (FPRs) of an AWG. Finally, a layer of 1.25 μm planarized oxide cladding is deposited on the top of the fabricated wafer. The fabrication was done through ePIXfab with IMEC technology.

The core component for the SC-AWG-loop is a cyclic 8-by-8 AWG. Its mask layout is shown in Figure 3.9(a). There are five main parts inside the AWG: input waveguides, input FPR, arrayed waveguides (AWs), output FPR and output waveguides. The light beam from one input waveguide aperture propagates through the input FPR and diverges to the aperture of the AWs. The coupled light propagates through the AWs with a constant optical length difference (ΔL) between two adjacent waveguides. ΔL can be expressed as: $\Delta L = m\lambda_c/n_{eff}$, where m is the grating order, λ_c the central wavelength, n_{eff} *th*e effective index of the AWs. λ_c is designed to be 1550 nm and the grating order *m* is designed to be 33. The free spectral range (FSR) is 32 nm (9.6 THz). The channel spacing (CS) is 4 nm (0.5 THz). The propagated light beams from AWs are recombined at the entrance of the output FPR and are then re-focused at the imaging plane to which the output waveguides connect. As shown in Figure 3.9(a), parabolic tapers are designed between the input waveguide and the input FPR to produce a flat-top-like field profile by exciting higher order modes in a controllable way. This will create the flat-top spectral pass-band profile as needed in AWG-loop2, which can reduce the in-band power imbalance (frequency fading). The simulated spectral transmission of the designed AWG is shown in Figure 3.9(b). The inputs and outputs are marked with their corresponding numbers as shown in Figure 3.9(b). In the simulation, the incident light is launched at the input waveguide of in4 and the transmitted light is monitored at different outputs. The wavelength of the incident light is swept from 1535 nm to 1567 nm. The simulated results show that the central wavelength from the 4^{th} input to the 5^{th} output is 1550.8 nm, slightly shifted from the designed central wavelength. The -3 dB bandwidth of the pass-bands of the AWG is 3.2 nm while that of the one without flat-top design is 1.9 nm. A test structure of the AWG is measured with cleaved fibres for vertical coupling. In our measurement, the minimum fibre coupling loss with standard single mode fibres is about 8 dB with a -6 dB bandwidth of 56 nm. The measured insertion loss of the AWG is about 4.8 dB without the loss of fibre grating couplers (FGCs). The measured FSR and CS are 30.3 nm and 3.8 nm, respectively. The central wavelength from the 4^{th} input to the 5^{th} output is measured as 1548.8 nm.

The layout of the SC-AWG-loop is shown in Figure 3.10. There are three FGCs used in the design for one input and two outputs. The optical signal from the input is split into two paths, one to the first output FGC (Out1) with an optical compensation delay in-between. The waveguides connect seven pairs of input and output to form the feedback loops. One pair of input and output (In1 and Out8) of the AWG is used as the input and output of the SC-AWG-loop. The width and height of the feedback waveguides are 450 nm and 220 nm, respectively. For the wavelengths directly travelling from In1 to Out8, the total delay is equal to the cross delay of the AWG (AWG-delay). For other wavelengths going through the feedback loops, the total delay includes twice the AWG-delay plus the delay of the feedback loops (loop-delay). Thus seven progressive delay line values can be obtained by wavelength tuning from the SC-AWG-loop. To design the suitable length of each feedback loop, there are three main steps. First, the optical lengths for the desired delay are calculated. Here the desired delay is 17.14 ps and thus the optical length is 5145 μm. Then it is divided by seven to obtain the optical length step, which is constant between two successive feedback loops. Second, the optical length of the AWG is calculated for further compensation. The AWG-delay roughly includes the optical delay in the FPRs and the array waveguide delay. The group index of the slab mode in the FPRs and the fundamental mode of the arrayed waveguides can be obtained from a full-vector finite difference method (FV-FDM) mode solver. The geometric lengths of different parts are multiplied with their group indexes to obtain their optical lengths. These optical lengths are then summed for the total optical length of the AWG. Third, the geometric lengths of the

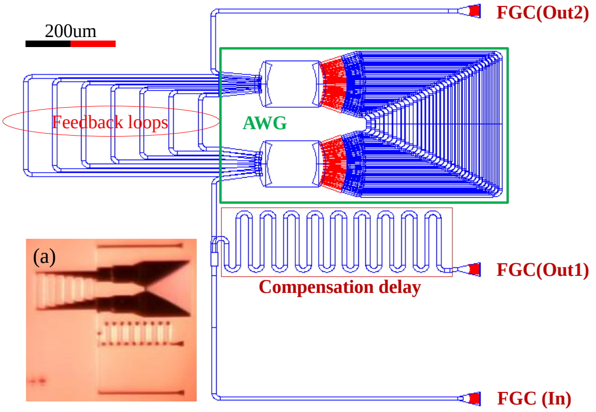

Figure 3.10 The layout of the designed AWG-loop and (a) its photo after fabrication. AWG: arrayed waveguide grating; FGC: fibre grating coupler.

feedback loops are calculated by dividing the demanded optical lengths with the group index of the feedback waveguides. The compensation delay shown in Figure 3.10 is used to compensate the travel delay induced by the connection waveguide, the AWG-delay (twice), and the most inner feedback loop (the minimum optical delay). Therefore the two replicas of the optical signal will arrive at Out1 and Out2 at the same time provided that the minimum one of the progressive optical delays is selected. The microscope photo of the fabricated device is shown in Figure 3.10(a).

3.4.2 Experimental setup, results and discussion

As shown in Figure 3.11, the delay features of the SC-AWG-loop are measured by means of an optical vector network analyzer which includes a linear analog optical link and an electrical vector network analyzer (VNA). The linear analog link basically includes a tunable laser source, a linearly-biased MZM, and a photo-diode (PD). The stimulus microwave signal from the output of the VNA is modulated on the optical carrier via the MZM. The optical signal then passes through the SC-AWG-loop and is launched into the PD which converts the optical signal back to the microwave signal. Such microwave signal is then compared with its local replica to obtain the amplitude/phase responses (versus frequency). The stimulus microwave single frequency signal is swept from 1 GHz to 20 GHz. The channel selection of the feedback loop is achieved by tuning the wavelength of the tunable laser.

Once a wavelength is tuned to a specified value, it remains there until the measurement by the VNA has been done. The wavelengths are fine-tuned to optimize the received power and therefore the spectral separations between two neighboring channels are not uniform. A calibration process is also performed in the VNA to remove the impact of the fibre coupling loss and the waveguide

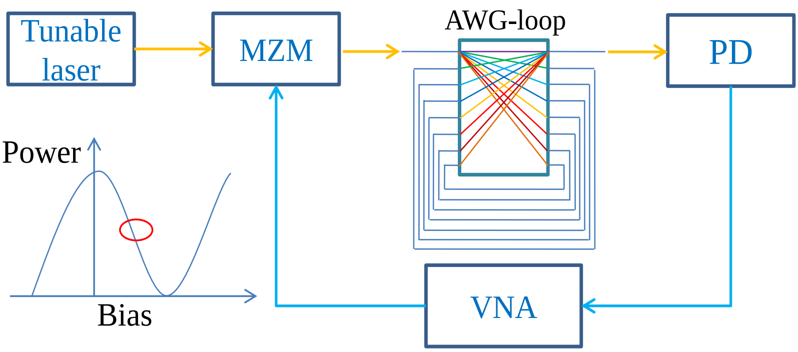

Figure 3.11 The experimental setup for the AWG-loop.

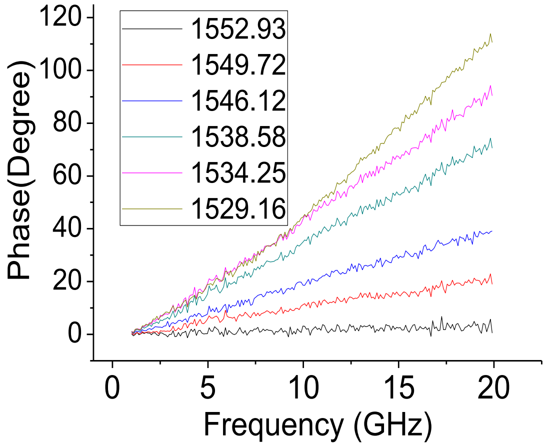

Figure 3.12 The measurement results for the AWG-loop.

Table 2 Designed and measured delays

Wavelength (nm)	**Designed Delay** (ps)	**Measured Delay** (ps)	**Delay Error** (%)
1552.93	0	0	0%
1549.72	2.857	2.922222	2.2829%
1546.12	5.714	5.698333	0.2742%
1538.58	11.428	10.66611	6.6669%
1534.25	14.285	13.44222	5.8997%
1529.16	17.142	16.51056	3.6836%

passive loss. The group delays induced by the fibre connections are eliminated as well. The relation between the phase shift and the group delay can be expressed as: $T = \Delta\phi/(2\pi\Delta f)$, where $\Delta\phi$ and Δf denote the phase and frequency difference between the stimulus microwave signal and the measured one, respectively. Once the phase response curve is measured, the group delay can be derived from it. The group delay measurement results are shown in Figure 3.112. One of the feedback loops could not be measured due to a failure in the waveguide. All of the six measured feedback loops exhibit linear relation between the phase and the frequency. Therefore the 1st derivatives of these phase response curves are constant, which means the delay is frequency-independent. The designed and measured delays are summarized and compared in Table 2. The delay errors vary among all the feedback loops but are all relatively low. The first channel is used as the reference and thus its delay error is 0. It can be seen that less than 6.7% delay errors are obtained for all feedback loops.

3.4.3 Conclusion

In this section, a compact step-wise tunable true time delay unit based on a SC-AWG-loop structure have proposed and realized on a SOI platform. A linear phase shift across a 20 GHz spectral width for different wavelengths was obtained. The measured results show that the delay errors are less than 6.7% for a broad 23-nm operation spectrum. Its compactness, fabrication tolerance, passive controllability, and scalability make it an attractive delay unit for microwave photonics transistors.

3.5 Indium-Phosphide based SC-AWG-loop chip

The indium-phosphide platform can provide efficient amplification in telecom wavelength windows (around 1550 nm), which enables a monolithic integration of both active and passive devices. In this section, a SC-AWG-loop in the indium-phosphide platform is designed, realized and investigated. This can pave the way to implement the full-function optical radio beam steering system including the high-speed photodiodes. In Section 3.5.1, the device design and fabrication is described. And in Section 3.5.2, the measured results are analyzed.

3.5.1 Design of Indium-Phosphide SC-AWG-loop chip

The SC-AWG-loop is fabricated on a 3 inch InP wafer with 500 μm thickness (which will be thinned down to 250 μm after processing). There are three types of waveguides, which are: a low-index-contrast waveguide E200, a medium-index-contrast waveguide E600, and a high-index-contrast waveguide E1700. The E200 and E1700 are employed in our design and their cross-sections are illustrated in Figure 3.13(a). The E200 waveguide provides low loss which enables the low loss operation of the AWG free propagation region. E1700 waveguide provides the high density layout of the designs. A generic foundry approach for the device design and fabrication is employed inside the framework of the Paradigm project. Such approach provides a very reliable device yield, which largely accelerates on-chip system realization. The fabrication was done through FhG-HHI.

The core component for the SC-AWG-loop is a cyclic 5-by-5 AWG. The mask layout of the test structure of the AWG is shown in Figure 3.13(b). There are five main parts inside the AWG: input waveguides, input FPR, arrayed waveguides (AWs), output FPR and output waveguides. The light beam from one input waveguide aperture propagates through the input FPR and diverges to the aperture of the AWs. The coupled light propagates through the AWs with a constant optical length difference (ΔL) between two adjacent waveguides. ΔL can be expressed as: $\Delta L = m\lambda_c/n_{eff}$, where m is the grating order, λ_c the central wavelength, n_{eff} *the* effective index of the AWs. λ_c is designed at 1550 nm and the grating order is designed to be 174. The free spectral range (FSR) is 8 nm (1000 GHz). The channel spacing (CS) is 1.6 nm (200 GHz). The propagated light beams from AWs are recombined at the entrance of the output FPR and are then re-focused at the imaging plane to which the output waveguides connect. Five spot size convertors (SSCs) are used to allow better lateral fibre-to-chip coupling. A photo of the AWG is also shown in Figure 3.13(b) with the same scale of its layout counterpart.

3.5.2 Experimental setup, results and discussion

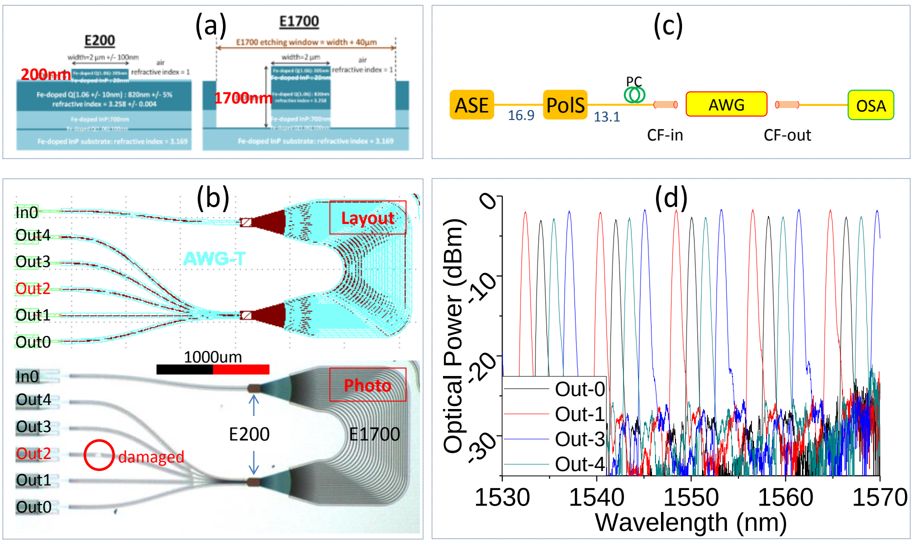

Figure 3.13 (a) The waveguide structure of 5-by-5 cyclic AWG, (b) the mask layout and photo of the AWG test structure, (c) the measurement setup, and (d) the measured spectral transmission of the AWG.

The measurement setup of the AWG is shown in Figure 3.13(c). The 16.9 dBm amplified spontaneous emission (ASE) noise from an EDFA is launched into a polarization beam splitter to allow the pure TE or TM polarization of the ASE noise. A cleaved single mode fibre (CF) is employed for lateral optical coupling. A polarization controller (PC) is employed to adjust the polarization of injected optical signal to be aligned with the TE mode of the input SSC (In0 marked in Figure 3.13(b)). The waveguide connecting In0 is located at the middle of the input FPR. The other cleaved fibre is used to collect the optical signal from the outputs (Out0~Out4) shown in Figure 3.13(b). An optical spectrum analyzer (OSA) with a resolution of 0.02 nm is used to record the measured results. The coupling loss of SSCs is 1.75 dB per facet. The waveguide loss of E1700 is 1.25 dB/cm for TE mode. The measured spectral transmission of the AWG is shown in Figure 3.13(d). The polarization controller introduces around 2 dB loss. The ASE noise is first launched into waveguide test structure and recorded by the OSA as a reference for further calibration. The Out2 waveguide of the AWG test structure is damaged which causes the missing of the transmission of Out-2 in Figure 3.13(d). The measured spectral center of Out2 (measured λ_c) is at 1546.8 nm. The insertion loss of the AWG is less than 2.8 dB and the insertion loss difference of all channels is less than 0.9 dB. The crosstalk is measured to be larger than 25 dB. An FFT operation of the measured spectral transmission data is performed, which indicates a 8 nm free spectral range (FSR) and a 1.6 nm channel spacing (CS). The -3dB bandwidth of all channel pass-bands is measured to be 0.52 nm, which means 65 GHz electrical bandwidth for radio signals. The cyclic spectrum feature is clearly shown in Figure 3.13(d).

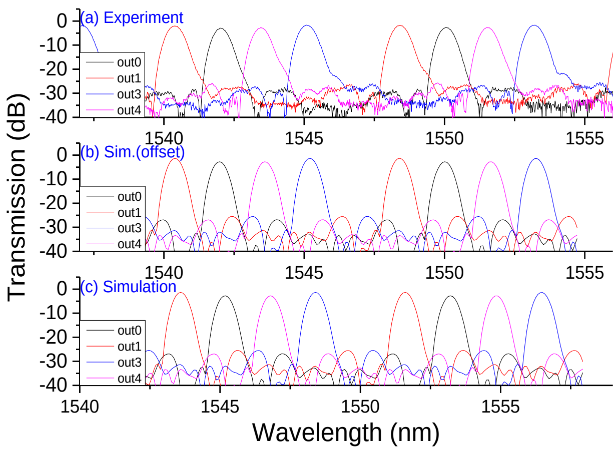

Items	Designed	Measured	Items	Designed	Measured
FSR	8nm	8nm	Insertion Loss	< 2.75dB	< 2.8dB
Central λ	1550nm	1546.8nm	Chan. spacing	1.6nm	1.6nm
BW(-3dB)	0.43nm	0.52nm	X-talk	>25dB	>25dB

Figure 3.14 The detailed comparison between the (a) experimental results and (b)-(c) simulated results.

A detailed comparison of the experimental and simulated results is shown in Figure 3.14. The simulation is performed by using the BrightPhotonics AWG design kit in the Pheonix Software environment. The waveguide loss of E1700 is set to be 1.25 dB/cm. The phase error distribution of the arrayed waveguides is modeled as a Gaussian distribution with σ = 10˚, which means 68% of arrayed waveguides have phase errors within -10˚ to 10˚. The simulation is carried out with the same configuration as the measurement has been done. The simulated result is shown in Figure 3.14(c). With -3.2 nm translation of the simulated results, we obtain its offset version shown in Figure 3.14(b). Comparing Figure 3.14(a) and (b), a very good match between measured results and simulated results are demonstrated except the channel bandwidth and λ_c. The measured channel bandwidth is larger partially because the polarization of injected ASE noise is not perfectly aligned with the TE mode of the input waveguide (In0). The 3.2 nm difference of λ_c with grating order of 174 indicates at least a 0.0018% group index error.

The measurement setup of the SC-AWG-loop is shown in Figure 3.15(a). The 12.9 dBm optical carrier from a tunable laser (Agilent N77xx) passes to a MZM via a PC. An electrical pulse with 500 ps duration generated from an electrical arbitrary waveform generator (E-AWG) is amplified by a 12 GHz electrical amplifier with 19 dB gain (SHF100APP) for optical modulation. The modulated optical signal with 2.6 dBm power is then launched into the SC-AWG-loop (In-

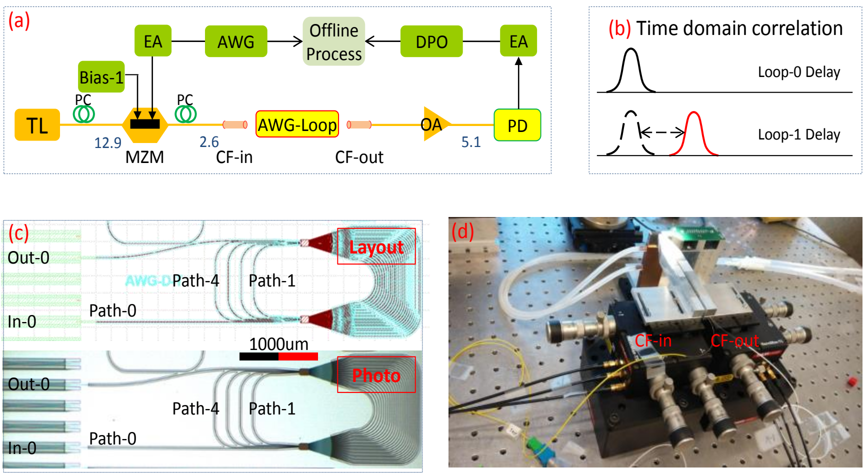

Figure 3.15 The measurement of the proposed AWG-loop, (a) the measurement setup; (b) time domain correlation for delay measurement; (c) mask layout and photo of the AWG-loop; (d) photo of cleaved fibre coupling system. CF-in/-out: cleaved fibre for input and output.

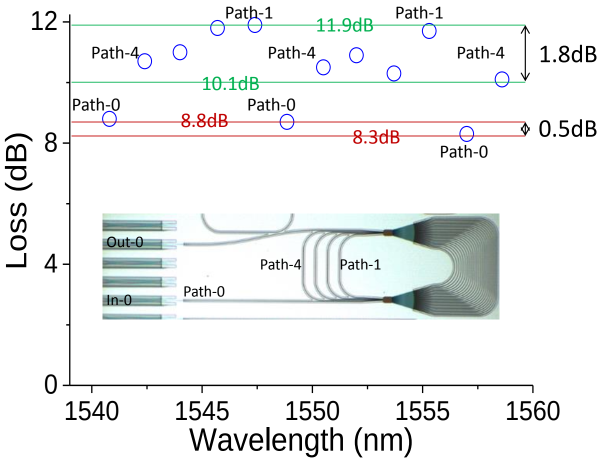

Figure 3.16 The measured insertion loss of different delay channels in the AWG-loop.

0) via a cleaved fibre. A PC is used to align the polarization to TE mode of waveguides in the SC-AWG-loop. Another cleaved fibre is employed to collect the output optical signal. The photo of the cleaved fibre coupling system is shown in Figure 3.15(d). With an EDFA (OA shown in Figure 3.15), the collected optical signal is amplified to 5.1 dBm before illuminating a 40 GHz photodiode (produced by U2T). The detected electrical signal is then amplified by an EA (SHF100APP) and is further sampled by a digital phosphor oscilloscope (Tektronix DPO70000) with an equivalent-time sampling mode. The oscilloscope is locked to the E-AWG by a 10 MHz reference clock. The sampling rate is 2.5 TSa/s and thus the time resolution is 400 fs. The sampled signal is then offline processed to obtain the delays. The layout of the SC-AWG-loop under test is shown in Figure 3.15(c). A 5-by-5 cyclic AWG identical to the previously measured one is used in the SC-AWG-loop. The waveguides connect four pairs of input and output to form the feedback loops with different delays. One pair of input and output of the AWG (In-0, Out-0) is used as the input and output of the SC-AWG-loop and is connected to two SSCs. The E1700 waveguides are used for all these connections. The maximum delay (Path-4) is designed to be 12.5 ps for π phase shift at 40 GHz. The designed delays of Path-1 to Path-4 are progressively increased from 0 to 12.5 ps. The photo of the SC-AWG-loop is also shown in Figure 3.15(c).

The loss of one open path (Path-0) and four feedback loop paths (Path-1 to -4) is measured and results are shown in Figure 3.16. The 3.5 dB coupling loss (1.75 dB per facet) and 2 dB link loss (polarization controller) are taken into account. A tunable laser (TL) is employed to provide fine-tuning of the

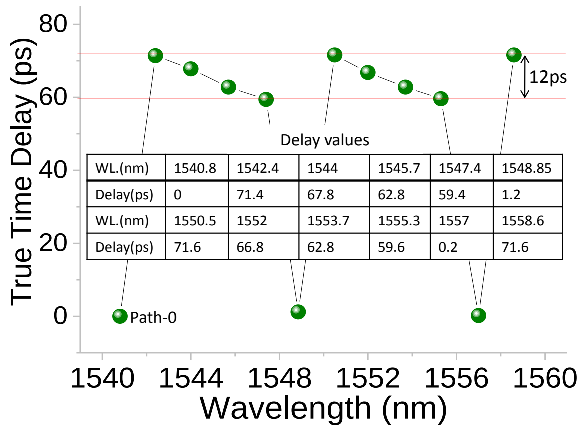

Figure 3.17 The measured delays of different delay channels of the AWG-loop.

wavelength for identifying the transmission peaks. During the loss measurement, the MZM and OA are bypassed and the OSA is replaced by an optical power meter. The measured results show that the loss for all channels is less than 12 dB. Subtracting the 5.5 dB off-chip loss, the measured results show 6.5 dB loss including twice the AWG insertion loss and the loss of waveguides in between. Such insertion loss of the integrated OTDL is acceptable for many applications. Considering the 1 dB waveguide loss and the insertion loss of the AWG itself, the measured results of the SC-AWG-loop exhibit the high consistency with its test structure counterpart. For the Path-0, since it travels through the AWG only once, the loss is lower than for the other paths. The Path-1 to Path-4 exhibit higher loss because of travelling twice through the AWG. On average, 2.5 dB less loss is incurred in Path-0 than the other paths. Due to the cyclic feature of the AWG, the loss also exhibits the cyclic feature. The loss variation of Path-0 is less than 0.5dB while the one of Path-1 to Path-4 are less than 1.8 dB. The measured λ_c is 1547.4 nm (Path-1), suggesting a 0.6 nm spectral offset from the AWG test structure. However, such spectral offset does not induce any mis-alignment because of the feedback loop configuration.

The delay is measured using the time domain correlation method whose principle is shown in Figure 3.15(b). The sampled signal travelled from Path-0 is used as a reference signal. The cross-correlation is performed between the other signals and the reference. The Path-0 can be found based on the minimum loss as indicated in Figure 3.16. For the wavelengths directly travelling from In-0 to Out-0, the total delay is equal to the cross delay of the AWG (AWG-delay). For other wavelengths going through the feedback loops, the total delay includes twice the AWG-delay plus the delay of the feedback loops (loop-delay).

Thus we can see the four progressive delays and also one 'fall-down' delay (Path-0) shown in Figure 3.17. As indicated in Figure 3.6, the 'fall-down' delay issue can be solved by the CODL. As shown in Figure 3.17, linear delay values are exhibited for Path-1 to Path-4 with 12ps delay which is a little bit less than what we expected. This could be caused by the limited time resolution (400 fs). The detailed delay values are also indicated in the inset table of Figure 3.17. The differences between the designed delays and the measured ones for Path-1 to Path-4 are -0.5 ps, 0.1 ps, -0.76 ps and 0 ps from 1540 nm to 1548 nm. And the delays of different wavelengths from Path-1 to Path-4 are 0.2 ps, -1 ps, 0 ps and 0.2 ps. The good match between the designed delays and measured ones demonstrate the high design accuracy.

3.5.3 Conclusion

In this section, a SC-AWG-loop concept has been realized in the indium-phosphide platform. The experimental results show less than 6.5 dB insertion loss of the integrated SC-AWG-loop. Five different delays from 0 ps to 71.6 ps are generated with less than 0.67 ps delay errors. These experimental results show the potential applications of the proposed SC-AWG-loop in the scenario of indoor RoF networks.

3.6 Summary

In this chapter, the operation principle of SC-AWG-loop is proposed and discussed. Due to the novel spectral-cyclic design, both cascaded operation for high resolution of delay and interleaved operation for 2-D radio beam steering can be achieved. The integrated implementation of the SC-AWG-loop concept is successfully demonstrated in both the silicon-on-insulator platform and the indium-phosphide platform. The measurements of both SC-AWG-loop chips demonstrate the feasibility of the SC-AWG-loop concept.

Chapter 4 Localization of radio devices

The localization of radio devices is a prerequisite for radio beam steering. An optical method can provide a transparent and immediate localization of radio devices while being immune for EM interferences. To achieve the simple and stable implementation of the optical localization, a novel solution using parallel optical delay detectors (PODD) is proposed. In Section 4.1, the background of optical localization is shortly reviewed. The intensity modulation-based PODD is studied in Section 4.2. Furthermore a simplified phase modulation-based PODD is investigated in Section 4.3.

4.1 Optical method for radio device localization

Determining the location of a microwave signal emitting device is of great importance for retrieving the position of objects. The parameter angle-of-arrival (AOA) or equivalently the time difference of arrival (TDOA) is required to accurately identify the position. An optical approach to measure the AOA can offer many benefits due to its intrinsic features like ultra-low loss and huge bandwidth, which allows high accuracy, and immunity to electromagnetic interferences. Moreover, with the rapid development of ultra-low drive voltage electro-optical modulators (EOMs) [72, 73] and high-speed photo-diodes [74, 75], the barriers between electrical domain and optical domain are gradually eliminated. Recently some photonic approaches have been proposed to measure AOAs of microwave signals [76-79]. Some of these approaches are based on optical modulators with the advantage of the availability of mature and commercial products. Furthermore, such schemes are scalable based on integrated optics. In [79], a serial optical delay detector using two EOMs and one discrete optical delay line is proposed for AOA measurements.

4.2 Optical localization based on intensity modulation

As discussed above, the scheme proposed in [79] is, in principle, an optical delay detector for microwave signals with serial configuration. However the optical delay line (fibre) between EOMs will introduce unwanted interference due to environment variations (e.g. temperature). In this section, a novel intensity modulation PODD (IM-PODD) with accuracy monitored is proposed based on a dual parallel MZM (P-MZM). P-MZMs are also recognized as IQ modulators for optical long-haul transmission. The integrated parallel structure can increase robustness against environment variations due to the absence of discrete external optical delay lines. Moreover, the DC drift induced measurement accuracy degradation can be monitored. In the following, the operation principle is described.

4.2.1 Operation principle

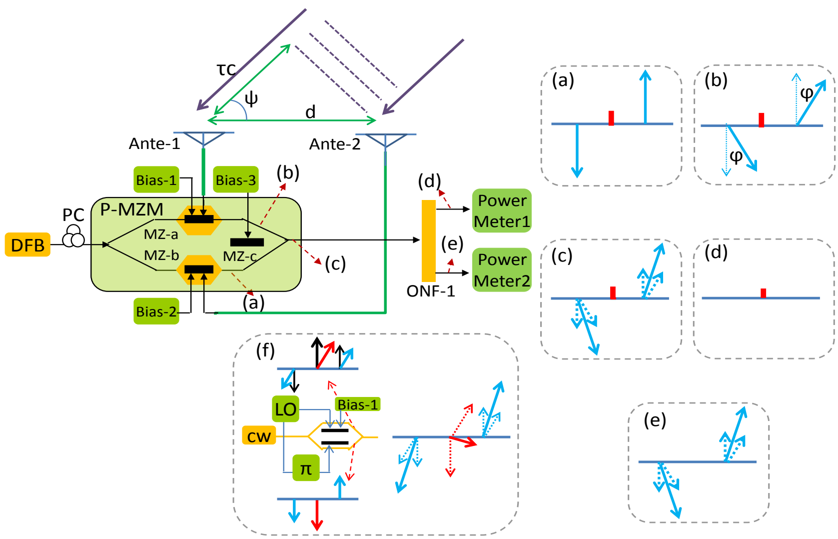

Figure 4.1 The principle of AOA measurement based on intensity modulation by a parallel optical delay detector.

The principle of AOA (or TDOA) measurement is depicted schematically in Figure 4.1. The distance between two antennas (Ante-1 and -2) is denoted as *d*. The AOA is denoted as ψ and the corresponding TDOA can be expressed by:

$$\tau = d\cos(\psi)/c \tag{4.1}$$

where c is the light velocity in air. As shown in Figure 4.1, MZ-a and -b are the sub-MZMs inside P-MZM, MZ-c is the tunable phase shifter between MZ-a and

-b. The electrical paths (including connections and necessary components like amplifiers) between Ante-1 and MZ-a, Ante-2 and MZ-b will introduce phase differences for different frequencies due to physical length differences and impedance mismatches. Such phase differences can be easily compensated using a look-up table. The TDOA τ will introduce a phase shift φ between Ante-1 and -2 as shown:

$$\varphi = \tau \times \omega_m \tag{4.2}$$

where ω_m is the angular frequency of microwave signal. Therefore the task of proposed IM-PODD scheme is to measure the phase shift φ by using optical techniques. The IM-PODD includes a continuous wave (CW) DFB laser, a P-MZM, an optical notch filter, and two optical power meters. MZ-a and -b are connected to Ante-1 and -2. The phase shift φ caused by spatial delay τ will be translated to the phase difference of the optical sidebands. The following task is to measure the phase difference of the optical sidebands by using optical power meters. Both MZ-a and -b are biased at the null points to suppress the optical carrier. The lightwave from the CW laser is modulated by two replicas of microwave signal at MZ-a and -b with spectra shown in Figure 4.1(a) and (b), respectively. The output optical signals from both MZ-a and -b with phase shift φ are then combined at MZ-c with an additional phase shift θ induced by the bias voltage applied to MZ-c. The optical spectrum of the combined signal is shown in Figure 4.1(c). As shown in Figure 4.1(d), the optical carrier is separated from optical sidebands via an optical notch filter (ONF-1 shown in Figure 4.1). Spectrums of the filtered optical sidebands are shown in Figure 4.1(e).

Now the theoretical model for the output optical power regarding to the phase shift φ can be deduced. The optical carrier can be expressed as:

$$E(t) = E_0 \exp(j\omega_0 t) \tag{4.3}$$

where E_0 and ω_0 are the amplitude and the angular frequency of the optical carrier. The optical carrier is then split into two sub-MZMs (MZ-a and -b). Both sub-MZMs are push-pull operated with DC bias at the null points. The microwave signal voltages applied to MZ-a and -b can be described as:

$$\begin{aligned} V_{am}(t) &= V_m \exp(j\omega_m t) \\ V_{bm}(t) &= V_m \exp(j\omega_m t + j\varphi) \end{aligned} \tag{4.4}$$

The high order (>2nd) sidebands are ignored since the received microwave power is relatively lower. The optical signal after MZ-a can be expressed as:

$$\begin{aligned} E_a(t) = &-\frac{1}{2} E_0 J_{+1}(m) \exp(j\omega_0 t + j\omega_m t) \\ &-\frac{1}{2} E_0 J_{-1}(m) \exp(j\omega_0 t - j\omega_m t) \end{aligned} \tag{4.5}$$

where $m=\pi V_m/V_\pi$ denotes the modulation depth and $J_{\pm 1}$(m) is the Bessel function of first kind with regard to modulation index (m). Similarly the output signal from MZ-b can be expressed as:

$$\begin{aligned} E_b(t) = & -\frac{1}{2}E_0 J_{+1}(m)\exp(j\omega_0 t + j\omega_m t + j\varphi) \\ & -\frac{1}{2}E_0 J_{-1}(m)\exp(j\omega_0 t - j\omega_m t - j\varphi) \end{aligned} \tag{4.6}$$

Both optical signals from MZ-a/b are combined via MZ-c with the additional phase shift and the output signal is:

$$\begin{aligned} E_{out}(t) = & -\frac{1}{2}E_0 J_{+1}(m)\exp(j\omega_0 t + j\omega_m t)[\exp(j\varphi) + \exp(j\theta)] \\ & -\frac{1}{2}E_0 J_{-1}(m)\exp(j\omega_0 t - j\omega_m t)[\exp(-j\varphi) + \exp(j\theta)] \end{aligned} \tag{4.7}$$

where θ is the DC bias induced phase shift in MZ-c. After the optical notch filter, the power of upper sideband can be obtained as:

$$\begin{aligned} P_{+1} &= E_0^2 J_{+1}^2(m)[\exp(j\varphi) + \exp(j\theta)][\exp(-j\varphi) + \exp(-j\theta)] \\ &= E_0^2 J_{+1}^2(m)[2 + \exp(j\varphi - j\theta) + \exp(j\theta - j\varphi)] \\ &= 2E_0^2 J_{+1}^2(m)[1 + \cos(\varphi - \theta)] \end{aligned} \tag{4.8}$$

Similarly we can obtain the power of lower sideband as:

$$\begin{aligned} P_{-1} &= E_0^2 J_{-1}^2(m)[\exp(-j\varphi) + \exp(j\theta)][\exp(j\varphi) + \exp(-j\theta)] \\ &= E_0^2 J_{-1}^2(m)[2 + \exp(-j\theta - j\varphi) + \exp(j\theta + j\varphi)] \\ &= 2E_0^2 J_{-1}^2(m)[1 + \cos(\varphi + \theta)] \end{aligned} \tag{4.9}$$

The phase shift θ in MZ-c can be set to zero and thus the power of upper and lower sidebands can be written as:

$$P_{\pm 1} = 2E_0^2 J_{\pm 1}^2(m)[1 + \cos(\varphi)] \tag{4.10}$$

It is clear that the output power is related to the phase shift φ. Since J_{+1}^2(m) is equal to J_{-1}^2(m), the output power of upper and lower sidebands induced by phase shift φ are equal. This feature will be employed for two samples (both output power samples of the upper and lower sidebands) measurement with high robustness since the noise is averaged. The upper and lower sidebands do not need to be separated, therefore by using an optical notch filter the desired results can be produced more simply than by using an optical multi-channel filter. Eq. (4.10) also indicates that amplitudes of sidebands are related to the modulation index m. The high order sidebands are negligible for low driving power, which is the case in AOA measurements. The value required for AOA estimation is the normalized power (P_n), thus the value of E_0 and J_{+1}(m) are less interesting. We can obtain the expressions for TODA (τ) and AOA (ψ) and as:

$$P_n = P_m / P_0 , \quad \varphi = \arccos(P_n - 1)$$
$$\tau = \arccos(P_n - 1) / \omega_m , \quad \psi = \arccos\left(\tau c / d\right) \tag{4.11}$$

According to Eq. (4.11), to estimate the values of τ and ψ, the required parameters are P_n and ω_m. P_n can be obtained by measuring P_m and P_0. P_0 is the measured output power with zero phase shift (φ=0) and the calibration procedure will be detailed in the following way. P_m is the measured optical power with different configurations. Based on the measured P_m, the phase shift φ can be estimated with a given value of ω_m. Further AOA (or TDOA) can be obtained based on Eq. (4.11). If ω_m is unknown, an additional photonic scheme can be utilized to perform frequency measurements before the AOA (or TODA) measurement.

In the above discussion, the optical carriers are assumed to be well suppressed, thus the power and phase shift can be fully modeled according to Eq. (4.11). However, both the limited extinction ratio of the modulator and the DC drift will introduce measurement errors. Since the limited extinction ratio is fixed once the modulator is fabricated, it is reasonable to focus on the analysis of DC drifts induced measurement errors. As shown in Figure 4.1(f), the proper bias applied to the upper arm of a MZM (MZ-a for instance) for optical carrier suppression should introduce π phase shift with respect to the lower arm as the black arrows shown in Figure 4.1(f). The DC drift at MZ-a/b will introduce the phase shift (γ) to the optical carrier and the sidebands. The E-field of the output optical signal from MZ-a can be expressed as:

$$\begin{aligned} E_a(t) = &\frac{1}{2} E_0 \exp(j\omega_0 t)[\exp(j\gamma)+1] J_0(m) \\ &+ \frac{1}{2} E_0 \exp(j\omega_0 t)[\exp(j\gamma)-1] J_{+1}(m) \exp(j\omega_m t) \\ &+ \frac{1}{2} E_0 \exp(j\omega_0 t)[\exp(j\gamma)-1] J_{-1}(m) \exp(-j\omega_m t) \end{aligned} \tag{4.12}$$

Comparing with Eq. (4.5), the power of the sidebands is not accurate to present the phase shift φ with such unwanted γ. Both DC drifts in MZ-a and -b will introduce similar effects. Thus it is of interest to monitor the DC drift during the measurement. Since the DC drift simultaneously introduces residual leakage of the optical carrier, the measurement of the optical carrier power can be used to monitor the DC drift. As shown in Figure 4.1, an optical notch filter (ONF-1 shown in Figure 4.1) is employed to sharply separate the optical carrier and sidebands. The separated optical carrier can then be monitored during the measurement process. In a practical system, an automatic bias control circuit can be used to reduce DC drifts. Such schemes are widely available since they are being used for stable advanced modulation format generations.

4.2.2 Experimental setup, results and discussion

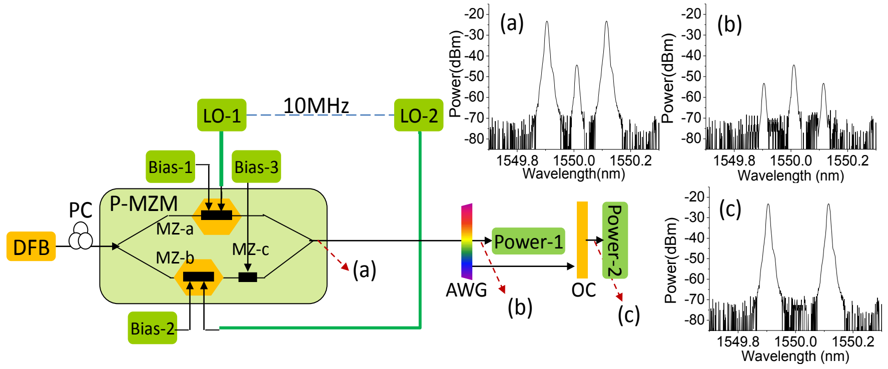

Figure 4.2 The experimental setup of AOA measurement based on intensity modulation parallel optical delay detector.

Figure 4.2 shows the proof-of-concept experimental setup of the AOA (or TDOA) measurement based on a parallel optical delay detector (PODD). The optical carrier is generated from a DFB laser at 1550.016 nm with 1 dBm power. It is fed into a P-MZM after a polarization controller (PC). MZ-a and -b are both biased at minimum points of their power transfer curves. Two commercial microwave sources (LO-1 and LO-2) are synchronized and are employed to drive MZ-a and -b at a frequency of 12.5 GHz. A 10 MHz sine signal generated from LO-1 is sent to LO-2 for synchronization. MZ-c is biased at the maximum point (zero phase shift) of its power transfer curve to avoid any additional phase shift and the optical spectrum of the combined signal is shown in Figure 4.2 (a). The phase differences between LO-1 and -2 induced by different electrical paths and impedance mismatches are measured by a commercial sampling oscilloscope (digital communication analyzer). It is then further calibrated via a look-up table. The output optical signal is then separated by an arrayed waveguide grating (AWG) which acts as an optical notch filter. In general, any kind of optical notch filters can be used here if its passband is narrower than the frequency of measured microwave signal. The channel spacing of the AWG is 12.5 GHz and the signal is then separated into three channels. The optical carrier is in the middle channel (noted as CH-2) and two sidebands are in two neighbor channels (noted as CH-1,3). The signal from CH-2 is used for the DC drift monitoring (measured at Power-1) with spectrum shown in Figure 4.2 (b). Optical signals from CH-1,3 are then coupled again via a coupler (OC) for power measurement (at Power-2). Its spectrum is shown in Figure 4.2 (c).

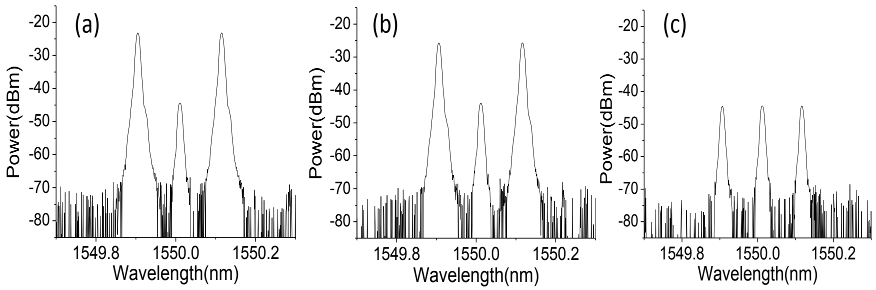

Figure 4.3 Measured spectrum for the phase shift of (a) 0°, (b) 90°, and (c) 180°.

The measured spectra from CH-1,3 with different phase shifts are shown in Figure 4.3. It can be clearly observed that the power of sidebands degrades when the phase shift increases. A calibration to obtain the minimum output power is carried out. After that, P_0 is obtained by getting the maximum power of sidebands. In Figure 4.3 (a) - (c), the optical carrier is not completely suppressed mainly due to the limited extinction ratio (ER), since the DC drift is mostly eliminated at the initial calibration stage. The limited ER is mostly the reason why the measurement errors are slightly worse than those in [79]. Two measurements are carried out. The first measurement is carried out just after the initial calibration stage. The power of the filtered optical carrier (P_0) is -47.6 dBm. The phase shift φ and corresponding measurement errors are measured. The second measurement is after a few tens of minutes and P_0 increase to -41.7 dBm due to DC drift. The phase shift φ is measured again with measurement errors. The measured powers versus different phase shifts (circles) are shown in Figure 4.4(a) for the first measurement. The theoretical power distribution (red curve) versus phase shift is also shown in Figure 4.4(a). An acceptable agreement has been obtained. The detailed measurement errors are shown in

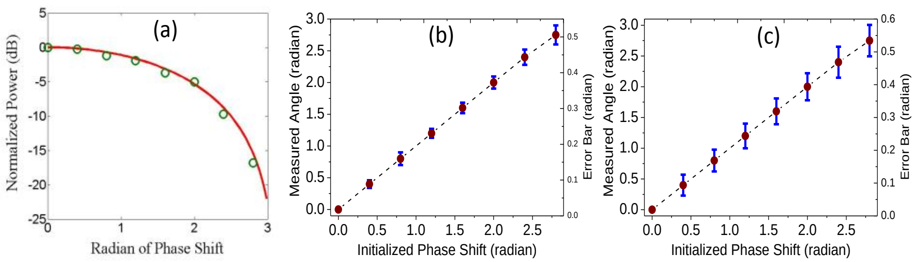

Figure 4.4 (a) Measured optical power (circles) and theoretical trend (curve); (b) Measured phase shift (dots) and their measurement errors (vertical bars),P_{mo}=-47.6dBm; (c) Measured phase shift (dots) and their measurement errors (vertical bars), P_{mo}=-41.7dBm.

Figure 4.4(b) and (c) for both measurements. The measurement errors are less than 8.59° within the range from 0° to 160° when the filtered power is -47.6 dBm. It is clear that the measurement errors increase when the phase shift goes to π. This is mainly because of the imperfect destruction of sidebands induced by the limited ER. Comparing Figure 4.4(b) and (c), it is obvious that the measurement errors increase when P_0 drifts to -41.7 dBm. It shows that the measurement accuracy degradation caused by DC drifts can be well monitored in this scheme. Note that a zero phase shift is used for normalization hence has no measurement error.

4.2.3 Conclusion

In this section, a parallel optical delay detector is proposed for angle-of-arrival measurement with the capability to monitor the accuracy. The spatial delay measurement is translated into the phase shift between two replicas of a microwave signal. The measurement errors are less than 8.59° within the range from 0° to 160°. Moreover, the capacity to monitor the measurement accuracy is investigated.

4.3 Optical localization based on phase modulation

In Section 4.2, the intensity modulation parallel optical delay detector has been proposed based on a P-MZM. Its integrated structure can increase the tolerance with respect to environment variations. Since there are three DC-biases and only one monitored parameter (power of optical carrier) in a P-MZM, a simple and robust automatic bias control (ABC) is difficult to achieve. To solve this problem, the core idea is to avoid unnecessary DC-biases by replacing intensity modulation with phase modulation. In this section, a novel phase modulation parallel optical delay detector (PM-PODD) using only one dual-electrode MZM (DE-MZM) is proposed. Because there is only one DC-bias in a DE-MZM, a simple and robust ABC is achievable. Moreover, the complexity and intrinsic insertion loss of the proposed scheme are halved compared to the one studied in Section 4.2.

4.3.1 Operation principle

The proposed scheme for AOA (or TDOA) measurement is depicted in Figure 4.5. It includes a DFB laser, a DE-MZM, an optical notch filter (ONF), and two optical power meters. The upper arm (U-arm) and lower arm (L-arm) are the two arms inside DE-MZM. Bias-1 is the tunable phase shifter between U- and L-arm. The U- and L-arm of the DE-MZM are connected to two

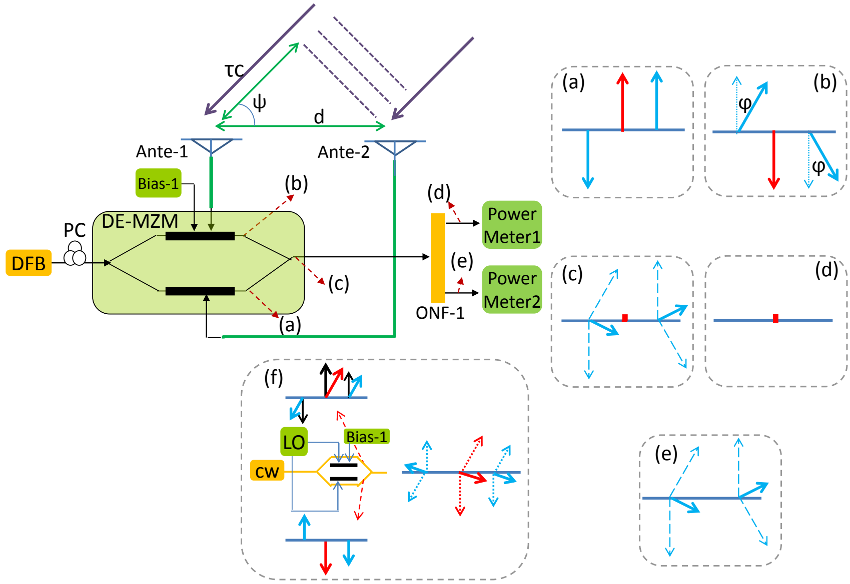

Figure 4.5 The principle of AOA measurement based on phase modulation by a parallel optical delay detector.

antennas, Ante-1 and -2. Similar as discussed in Section 4.2, The TDOA can be measured based on Eq. (4.1) and (4.2) .

The next task is to measure this phase difference of the optical sidebands by using optical power meters. The U-arm is biased at the null point to suppress the optical carrier. The lightwave from the CW laser is modulated by two replicas of the microwave signal with phase shift φ at the U- and L-arm, of which the spectra are shown in Figure 4.5(a) and (b), respectively. The output optical signals from both U- and L-arm with phase shift φ are then combined with an additional phase shift θ induced by the bias voltage applied to Bias-1. The optical spectrum of the combined signal is shown in Figure 4.5(c). As shown in Figure 4.5(d), the optical carrier is separated from the optical sidebands via an optical notch filter (ONF-1 shown in Figure 4.5). The spectrum of the filtered optical sidebands is shown in Figure 4.5(e).

Now the theoretical model for the output optical power regarding the phase shift φ can be deduced. The optical carrier can be expressed as Eq (4.3). The optical carrier is then split into two arms (U- and L-arm). The microwave signal applied to the U- and L-arm can be expressed as Eq. (4.4). The optical signal after the DE-MZM can be expressed as:

$$E_{out}(t) = \frac{1}{2} E_0 \exp(j\omega_0 t) \times \sum_{n=-\infty}^{\infty} [\exp(jn\varphi) + \exp(j\theta)] j^n J_n(m) \exp(jn\omega_m t) \quad (4.13)$$

where $m=\pi V_m/V_\pi$ denotes the modulation depth. θ is a phase shift introduced by a DC bias. This θ is equal to π for the null points. The high order (>2nd) sidebands are ignored since the received microwave power of these high order sidebands is relatively low. The expression can be further condensed to:

$$\begin{aligned} E_{out}(t) = &+\frac{1}{2} jE_0 J_{+1}(m)[\exp(j\varphi) - 1] \exp(j\omega_0 t + j\omega_m t) \\ &-\frac{1}{2} jE_0 J_{-1}(m)[\exp(-j\varphi) - 1] \exp(j\omega_0 t - j\omega_m t) \end{aligned} \quad (4.14)$$

After the optical notch filter, the power of the upper sideband can be obtained as:

$$\begin{aligned} P_{+1} &= \frac{1}{4} E_0^2 J_{+1}^2(m)[\exp(j\varphi) - 1][\exp(-j\varphi) - 1] \\ &= \frac{1}{2} E_0^2 J_{+1}^2(m)[1 - \cos(\varphi)] \end{aligned} \quad (4.15)$$

where $J_{+1}(m)$ is the Bessel function of the first kind with regard to modulation index (m). Similarly, the power of the lower sideband can be obtained as:

$$\begin{aligned} P_{-1} &= \frac{1}{4} E_0^2 J_{-1}^2(m)[\exp(-j\varphi) - 1][\exp(j\varphi) - 1] \\ &= \frac{1}{2} E_0^2 J_{-1}^2(m)[1 - \cos(\varphi)] \end{aligned} \quad (4.16)$$

Thus, the power of the upper and lower sideband can be written in a unified expression:

$$P_{\pm 1} = \frac{1}{2} E_0^2 J_{\pm 1}^2(m)[1 - \cos(\varphi)] \quad (4.17)$$

It is clear that the output power is related to the phase shift φ. Since $J_{+1}^2(m)$ is equal to $J_{-1}^2(m)$, the output power of upper and lower sidebands induced by phase shift φ are equal. This feature will be employed for the measurement of the two samples (output power samples of both the upper and lower sidebands) with high robustness since the noise is averaged. The upper and lower sidebands do not need to be separated; therefore an optical notch filter can be used to obtain the desired results. From Eq. (4.17), it is clear that the amplitudes of the sidebands are related to the modulation index m. The high order sidebands are negligible for low driving power, which is the case for AOA measurements. The value required for the AOA estimation is the normalized power (P_n), thus the value of E_0 and $J_{\pm 1}(m)$ are less interesting. We can obtain the expressions for the TODA (τ) and AOA (ψ) as:

$$\begin{aligned} &P_n = P_m / P_0, \quad \varphi = \arccos(P_n - 1) \\ &\tau = \arccos(P_n - 1)/\omega_m, \quad \psi = \arccos\left(\tau c / d\right) \end{aligned} \tag{4.18}$$

According to Eq. (4.18), to estimate the values of τ and ψ, the required parameters are P_n and ω_m. P_n can be obtained by measuring P_m and P_0. P_0 is the measured output power with zero phase shift ($\varphi=0$) and the calibration procedure will be detailed in the following. P_m is the measured optical power with different configurations. Based on the measured P_m, the phase shift φ can be estimated for a given value of ω_m. Further we can get the AOA (or TDOA) based on Eq. (4.18). If ω_m is unknown, an additional photonic scheme can be utilized to perform a frequency measurement before the AOA (or TODA) measurement. In the above discussion, we assume that the optical carrier is well suppressed, and thus the power and phase shift can be fully modeled according to Eq. (4.18). However, both the limited extinction ratio and the DC drift will introduce measurement errors. Since the limited extinction ratio is given once the modulator is fabricated, it is reasonable to emphasize the analysis of DC drifts induced measurement errors. The proper bias applied to the U-arm for optical carrier suppression should introduce π phase shift between the U- and L-arm as the black arrows show in Figure 4.5(f). The DC drift will introduce the phase shift θ to the optical carrier and the sidebands. The E-field of output optical signal can be expressed as:

$$\begin{aligned} E_{out}(t) = &\frac{1}{2} E_0 \exp(j\omega_0 t)[1+\exp(j\theta)] J_0(m) \\ &+\frac{1}{2} E_0 J_{+1}(m) \exp(j\varphi + j\theta) \exp(j\omega_0 t + j\omega_m t) \\ &+\frac{1}{2} E_0 J_{-1}(m) \exp(-j\varphi + j\theta) \exp(j\omega_0 t - j\omega_m t) \end{aligned} \tag{4.19}$$

Comparing with Eq. (4.14), the power of the sidebands is not accurate to present the phase shift φ with such unwanted θ. Both DC drifts in the U- and L-arm will introduce similar effects. Thus it is of interest to monitor the DC drift during the measurement. Since the DC drift simultaneously introduces residual leakage of the optical carrier, the power measurement of the optical carrier can be used to monitor the DC drift. As shown in Figure 4.5, an optical notch filter (ONF-1 shown in Figure 4.5) is employed to sharply separate the optical carrier and the sidebands. The separated optical carrier can then be monitored during the measurement process. In a practical system, an automatic bias control circuit can be used to reduce DC drifts. Such kind of scheme is widely available since they are commonly used for stable advanced modulation format generations.

4.3.2 Experimental setup, results and discussion

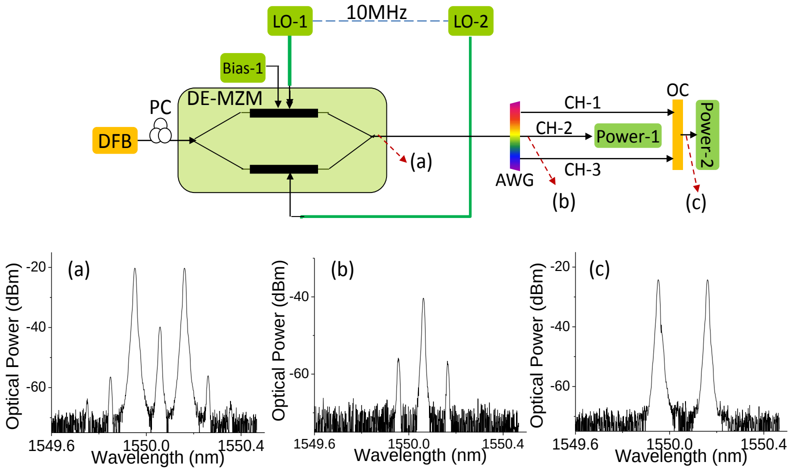

Figure 4.6 The experimental setup of AOA measurement based on phase modulation parallel optical delay detector.

Figure 4.6 show the proof-of-concept experimental setup of the AOA (or TDOA) measurement based on the proposed PM-PODD. The optical carrier is generated from a DFB laser at 1550.016 nm with 1 dBm power. It is fed into a DE-MZM after a polarization controller (PC). Two commercial microwave sources (LO-1 and LO-2) are employed to drive the U- and L-arm at a frequency of 12.5 GHz, respectively. A 10 MHz sinusoidal signal generated from LO-1 is sent to LO-2 for phase synchronization. The DE-MZM is biased at the null of its power transfer curve and the optical spectrum of the combined signal is shown in Figure 4.6 (a). The observed 2nd and 3rd order sidebands are lower than the 1st order side band by more than 35 dB and 45dB respectively. Thus the higher order sidebands can be neglected. The phase differences between LO-1 and LO-2 induced by different electrical paths and impedance mismatches are measured by a sampling oscilloscope (digital communication analyzer). It is then further calibrated via a look-up table. The optical output signal is separated by an AWG which acts as an optical notch filter. In general, any kind of optical notch filter can be used here if its stop-band is narrower than the carrier frequency of the measured microwave signal. The channel spacing of the AWG is 12.5 GHz and the signal is separated into three channels. The optical carrier is in the middle channel (noted as CH-2) and two sidebands are in two neighbor channels (noted as CH-1,3). The signal from CH-2 is used for the DC drift monitoring (measured at Power-1) with its spectrum shown in

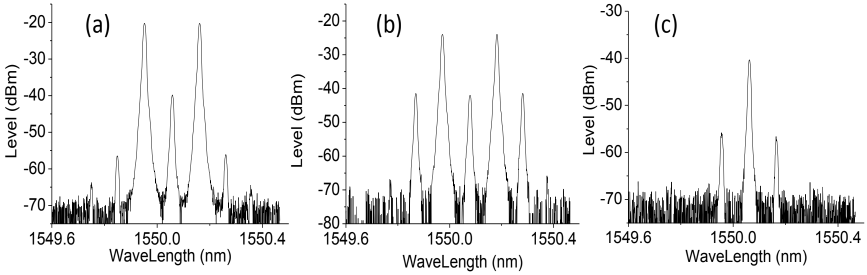

Figure 4.7 The measured spectrum for (a) 180 °phase shift, (b) 90 °phase shift, and (c) 0 °phase shift

Figure 4.6 (b). Optical signals from CH-1,3 are then coupled again via a coupler (OC) for power measurement (at Power-2). Its spectrum is shown in Figure 4.6 (c).

The measured spectra from CH-1,3 with different phase shifts are shown in Figure 4.7. As shown in Figure 4.7(a), the sidebands are enhanced when the phase shift is 180°. The sidebands are destructively combined once the phase shift is 0° shown in Figure 4.7(c). We can clearly observe that the power of the sidebands degrades when the phase shift φ decreases, which is in agreement with Eq. (4.17). It should be noted that the 2nd order sidebands vary when the phase shift changes. In our experiment, the 2nd order sidebands are filtered out as well by the AWG as shown in Figure 4.6 (c). Thus its influence will be largely limited. However, even for the system using only one optical notch filter, its effect is negligible since its power is lower than the power of 1st order sidebands by >35-dB. A calibration to obtain the minimum output power of the optical carrier is carried out. After that, the P_0 is obtained by getting the maximum power of the sidebands. In Figure 4.7(a)-(c), the optical carrier is not

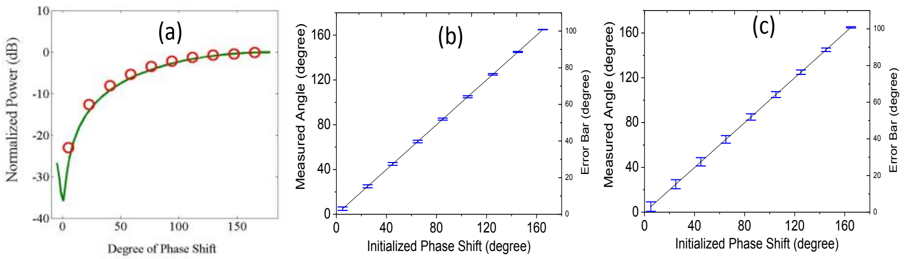

Figure 4.8 (a) Measured optical power (circles) and theoretical trend (curve), P_{mo}=-45.3dBm; (b) Measured phase shift (dots) and their measurement errors (vertical bars), P_{mo}=-45.3dBm; (c) Measured phase shift (dots) and their measurement errors (vertical bars), P_{mo}=-40.5dBm.

completely suppressed mainly due to the limited extinction ratio, since the DC drift is mostly eliminated at the initial calibration stage. Two measurements are carried out. The first measurement is carried out just after the initial calibration stage. The power of the filtered optical carrier (P_0) is -45.3 dBm. The phase shift φ and corresponding measurement errors are measured. The second measurement is after a few tens of minutes and P_0 increased to -40.5 dBm due to DC drift. The phase shift φ is measured again with measurement errors. The measured powers versus different phase shifts (circles) are shown in Figure 4.8(a) for the first measurement. The theoretical power distribution (red curve) versus phase shift is also shown in Figure 4.8(a). An accepted agreement is obtained. The detailed measurement errors are shown in Figure 4.8(b) and (c) for both measurements. The measurement errors are less than 3.1° within the range from 5° to 165° when the filtered power is -45.3 dBm. It is clear that the measurement errors increase when the phase shift goes to 0°. This is mainly because of imperfect destruction of sidebands induced by the limited extinction ratio. Comparing Figure 4.8(b) and (c), it is obvious that the measurement errors increase up to 7.7° when P_0 drifts to -40.5 dBm. It shows that the measurement accuracy degradation induced by DC drifts can be well monitored in this scheme.

4.3.3 Conclusion

In this section, a phase modulation parallel optical delay detector for microwave angle-of-arrival measurement with accuracy monitoring is proposed using only one dual-electrode MZM. The spatial delay measurement is translated into the phase shift between two replicas of a microwave signal. Thanks to the accuracy monitoring, phase shifts from 5° to 165° are measured within 3.1° measurement error. With the capability of accuracy monitoring, and robust parallel and simple structure, the proposed scheme can be an attractive solution for photonic AOA measurements.

4.4 Summary

In this chapter, the optical localization of radio devices is studied based on the two novel parallel optical delay detector (PODD) schemes. The intensity modulation PODD (IM-PODD) is first investigated for angle-of-arrival measurement. A major advantage of such scheme is that the measurement accuracy can be monitored. Experimental results show that the measurement errors are less than 8.59° within the range from 0° to 160°. Furthermore, to simplify the IM-PODD, a novel phase modulation PODD scheme is then proposed using only one dual-electrode MZM. Similarly as IM-PODD, PM-

PODD can also provide the measurement accuracy monitoring. Thanks to the accuracy monitoring, the phase shifts from 5 ° to 165 ° are measured with 3.1 ° measurement error. The PM-PODD performs clearly better than the IM-PODD in terms of measurement errors.

Chapter 5 Control Channel for Indoor Fiber-wireless Networks

As discussed in Chapter 2, the gateway of indoor fibre-wireless networks should deal with three types of signals: the first is the baseband signal, the second is the IF signal and the last is the RF signal. Usually, the baseband signal is from optical access networks (mostly passive optical networks). The IF and RF signals can be within the indoor networks, and can also be from the outdoor network, in particular a cellular network (GSM, UMTS, LTE) of which the signal also needs indoor coverage. Control channel is necessary to provide functions as:

-manage the traffic routing elements (λ-routers, switches);

-manage the dynamic bandwidth allocation (allocation of time slots in TDMA, of frequency slots in FDMA) to terminal users;

-manage protection mechanism (rerouting of traffic if network parts fail)

-manage mobility of users (reroute traffic when users move).

In this chapter, a novel and simple control signaling delivery for the gateway of indoor networks is studied. The control signaling is important for the realization of network functions and it only occupies limited bandwidth. For optical access networks, the gateway is considered as a remote node to pick up the data from optical access networks, for instance, passive optical networks (PON). The control signaling needs to be obtained for gateway. The difficulty is to process the high speed baseband data (>10Gb/s). For the IF and RF signals, signaling delivery is required for the remote access network in each room for network functions. The challenge is to efficiently obtain the low speed control signaling from the mm-wave frequency carrier. In this chapter, the control signaling delivery for PON data is investigated in Section 5.1. Next, the one for the IF/RF signal is studied in Section 5.2.

5.1 The control channel embedded in a PON fiber access network

In this section, a simple control channel insertion and detection scheme that can satisfy the aforementioned requirements is proposed. The section is organized as follows. First a short review of OFDM-PON is given in 5.1.1 to address its advanced features and the importance of control channel delivery in such networks. In Section 5.1.2, the architecture of a reconfigurable WDM-OFDM-PON and the operation principle of a low frequency insertion and detection (LFID) scheme are described. Section 5.1.3 analyzes the impairments induced by control channel insertion and the corresponding techniques to alleviate them. In Section 5.1.4, an experiment based on the LFID scheme is demonstrated to evaluate the system performance. The experiment is for OFDM-PON, however, the concept of LFID can be extended to other types of PONs.

5.1.1 Control channel requirement for OFDM-PON signal

Optical orthogonal frequency division multiplexing (OOFDM) has been proposed for the future optical networks based on various architectures [80-88]. High frequency efficiency, robustness to the transmission impairments and dynamic bandwidth allocation in both frequency and time domain make OOFDM suitable for the next generation optical access networks. Combined with WDM structure, the WDM-OFDM optical access network has already drawn much attention [80].

The rapid development of wireless communication means that the resulting traffic occupies a conspicuous proportion in access networks and will play an increasing role in the foreseeable future. The traffic-load profiles attributed to wireless networks are different from fixed networks, because of the mobility of the users. Thus dynamic bandwidth allocation (DBA) needs to be investigated for the future access networks. Research on this topic typically focused on the DBA protocols implemented at the higher layers of the network-layer stack [89, 90]. To take full advantage of the bandwidth available in the optical domain, physical layers that can support dynamic channel allocation (DCA) are a must for future optical access networks. Namely, the optical physical layers should comprise the wavelength-routing capability. To dynamically adapt reconfigurable nodes (RNs), the control channel system is a key for the efficient operation of reconfigurable networks. J.A. Lazaro et al. proposed a reconfigurable wavelength division multiplexing and time division multiplexing (WDM-TDM) network with ring-tree topology [91]. The authors did not discuss the control channel in detail. P. J. Urban et al. investigated a reconfigurable

WDM-TDM network with micro-ring resonators (MRRs) based reconfigurable optical add-drop multiplexers (OADM) [92, 93]. They proposed the control channel using a pair of independent wavelengths [93]. X. Xin et al. discussed the dynamic bandwidth allocation in the optical domain of WDM-OFDM access networks [82]. They claimed that the conventional OFDM access network lacked channel scheduling and the dynamic wavelength distribution was essential for WDM-OFDM optical access networks (WDM-OFDM-OAN). However, they did not address the control channel for wavelength routing in their proposed scheme.

For the traditional optical access network the signaling in the control channel is embedded into designated time slots. The insertion and detection of signaling is consequently operated at the full line rate speed. Because the RNs only take roles of switching and no user data process is involved, the utilized bandwidth is low and most bandwidth is wasted. Taking a 100 Gb/s access network for example, the RNs detects the optical signal by using the 100 Gb/s receivers and logical circuits only to retrieve relatively low speed signaling (<100 Mb/s). The complicated structure certainly introduces instability and extra cost. For future cost-efficient reconfigurable optical access networks, compatible, in-band, synchronized, simple and stable control channel systems are desired.

5.1.2 Architecture and operation principle

In this section, a ring-tree topology based architecture of reconfigurable WDM-OFDM-OANs is proposed and described. Based on this network, the operation principle of LFID is addressed.

A) Architecture of the reconfigurable WDM OFDM access network

The proposed architecture of reconfigurable WDM OFDM access networks is depicted in Figure 5.1. A ring-tree topology is introduced in line with previous research carried out in our group [93]. Other reconfigurable topologies are also available for LFD implementation. This architecture is based on a WDM fibre ring with single-fibre wavelength division trees connected to the main ring at reconfigurable nodes (RNs). Each RN has to drop and add signals (downstream and upstream) at two independent wavelengths. All signals can be launched into the ring fibre in both directions. This provides two paths to reach each RN and thus protection can be available for all the RNs even in case of fibre failure. The ONUs are connected to corresponding RNs with a power splitting distributive passive optical network (PON). Each PON shares an optical channel on a time division multiplexing (TDM) and frequency division multiplexing (FDM) basis.

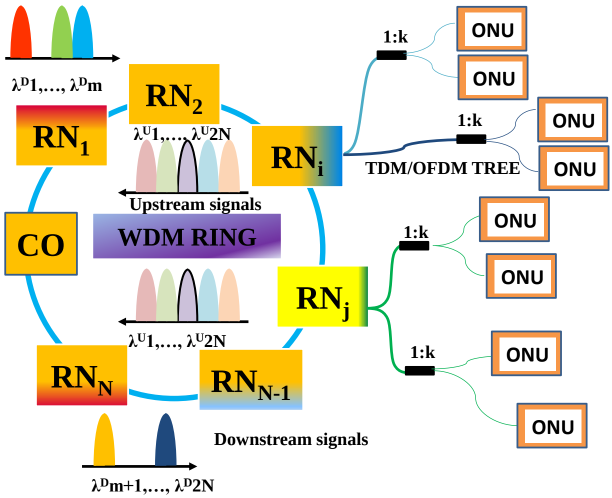

Figure 5.1 The principal architecture of reconfigurable WDM OFDM access networks with ring-tree topology.

The benefit of reconfigurability is based on flexible capacity reallocation [94]. Given the actual traffic loads on all the used wavelength channels, the request from one ONU may not fit into its default wavelength channel, but may fit into another wavelength channel that still has sufficient capacity available. In the fixed wavelength assignment case, this request will be blocked but it can be accepted when utilizing the flexible wavelength assignment. Therefore, such architecture will decrease the blocking probability, which means that more requests can be accepted.

B) Operation principle of low frequency insertion and detection scheme

The low frequency control channel insertion and detection scheme is to be utilized in the reconfigurable WDM-OFDM-OAN described above. Here the LFID operation principle in the signal process layer and also in the network layer will be discussed. The LFID operation principle in the signal process layer is depicted in Figure 5.3. The OOK modulated low speed signaling is added to the OFDM signal. The main power contribution of the OOK signaling signal is located in the frequency range below the first null of the OFDM signal spectrum. The accurate mathematical model and more details will be discussed in Section 5.1.3. To reduce the interference, the OFDM subcarriers which overlap with the OOK spectrum are reserved (carrying no bits). The coupling operation of the OOK signal and the OFDM signal is preferably realized in the digital domain because the OFDM signal is always generated based on digital IFFT. The digital combination of OOK and OFDM is the simple addition of their values. After combining of OOK and OFDM, the combined digital waveform is

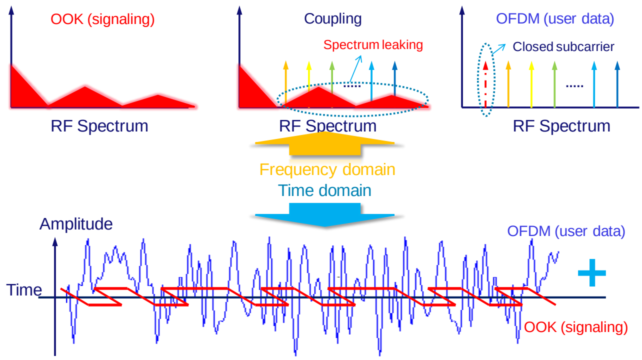

Figure 5.3 The signal process principle of low frequency signaling insertion in the electrical domain.

converted to an analog signal through a DAC. The electrical signal after the DAC is then modulated on the optical carrier via a MZM to construct a directly detected, low cost and no frequency guard interval (FGI) optical OFDM transmitter which is suitable for access networks [84, 95].

The optical spectrum of the modulated optical signal is depicted in the Figure 5.2(a). After the transmission over the fibre ring, the RN will receive the optical signal after an asymmetric optical splitter. A low speed photo-diode followed by an electrical low-pass filter is employed to detect the combined signal. The direct detection introduces the beating noise induced by square-law photon detection to the received combined signal as shown in Figure 5.2(a)-(d). The low pass feature of the low speed PD and low-pass filter is used to remove the OFDM signal as shown in Figure 5.2(d). Then the signaling (OOK signal) can be retrieved using low speed logical circuit. There is no complicated high-speed device needed for signaling detection in RNs. This is a significant advantage of

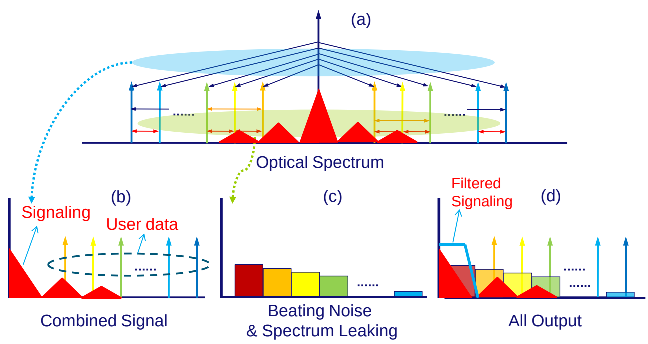

Figure 5.2 The signal process principle of optical modulation and retrieving of combined signal (signaling and user data).

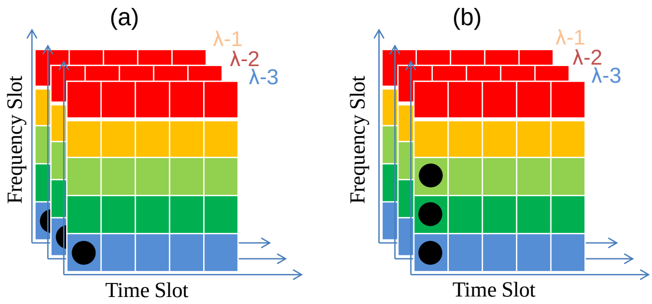

Figure 5.4 The operation principle of signaling insertion in the LFID scheme.

the LFID scheme and is beneficial to reduce the cost of RNs. The user data (OFDM) can be well retrieved in the ONU even without any electrical high-band pass filter (which will be discussed in Section 5.1.3). The LFID introduces no additional complexity to the user data demodulation. Thus the total cost of the proposed scheme can be largely reduced.

The operation principle of LFID in the network layer is illustrated in the Figure 5.4. The diagrams in both Figure 5.4(a) and (b) denote the bandwidth resource located in one wavelength channel. The different planes denote the different wavelengths launched into the fibre ring. The vertical grids in one plane denote the frequency slots (OFDM subcarriers) and the horizontal grids denote the time slots. The black solid circles present the occupied bandwidth resource (frequency and time slots) for the control channel signaling insertion. The occupied bandwidth resource can be tailored to satisfy various signaling delivery methods.

Figure 5.4(a) demonstrates the first signaling insertion method. The signaling is inserted in the low frequency slots of all wavelengths. In this case the signaling detection for RNs is processed in all wavelength channels. In each RN, the signaling is retrieved from the dropped wavelength. A complicated algorithm is required to synchronize and coordinate the switch of wavelengths.

The second operation method of signaling insertion is illustrated in the Figure 5.4(b). Apart from the first method, all the signaling required for all wavelengths is packed and then inserted into one dedicated wavelength. In this case, one dedicated wavelength is filtered out for signaling delivery in each RN. This method requires the same optical notch filter for all RNs. The capacity of delivered signaling varies from 1Mb/s level (the first method) to 100Mb/s level (the second method). To allow an adequate bandwidth for control channel insertion, an accurate mathematical model is derived in the Section 5.1.3.

5.1.3 Impairments and compensation techniques

In this section, the impairments incurred by the insertion and detection in the LFID scheme will be analyzed based on a mathematic model. The spectrum of an electrical OFDM signal modulated on an optical carrier is shown in Figure 5.2(a). The time domain representation of an OFDM signal can be defined as:

$$S(t)=\sum_{k=n_0}^{N}\left(a_k\cos k\Omega t+b_k\sin k\Omega t\right) \tag{5.1}$$

where N denotes the number of subcarriers in a OFDM symbol, Ω is the frequency spacing between the subcarriers, $k\Omega$ is the frequency of k_{th} subcarrier, n_0 is the index of the lowest subcarrier with data (lower subcarriers are unfilled, i.e. carrying no data) to allow insertion of signaling, a_k and b_k represent complex data symbols of in-phase and quadrature components for the k_{th} subcarrier. The OFDM signal inserted with signaling can be described as follows:

$$\begin{gathered}S_I(t)=\sum_{k=n_0}^{N_1}\left(a_k\cos k\Omega t+b_k\sin k\Omega t\right)g_1(t-nT_1)\\+\sum_{n=1}^{N_2}c_n g_2(t-nT_2)\\c_n=\begin{cases}C_1, & when\ c_n\ denotes\ 'one'\\C_0, & when\ c_n\ denotes\ 'zero'\end{cases}\end{gathered} \tag{5.2}$$

T_1 and T_2 denotes time period of an OFDM symbol (user data) and OOK symbol (signaling data). c_n denotes a data symbol of the OOK signal. C_0 and C_1 denote the electrical levels for logical ‘zero’ and logical ‘one’ of the OOK signal at the period from $(n-1)T_2$ to nT_2. $g_1(t)$ and $g_2(t)$ are windowing functions, which can be for instance a rectangular or raised cosine window. The optical OFDM signal using double-sideband modulation can be expressed as:

$$E_{out}(t)=A_o\cos(\omega_o t)\left[1+\gamma S_I(t)\right] \tag{5.3}$$

where γ denotes optical modulation index (OMI) in the linear range of an intensity modulator (IM). The OMI can be expressed as:

$$\gamma=\frac{V_{pp}}{V_\pi\sqrt{PAPR}} \tag{5.4}$$

V_{pp} is the peak-to-peak voltage of the OFDM signal applied to the MZM. PAPR denotes the peak-to-average power ratio of the OFDM signal. Note that the OFDM signal can be optionally pre-distorted in case that its peak-to-peak voltage (V_{pp}) lies out of the linear driving range. The square-law photo-detector works as an envelope detector and converts the intensity modulation on lightwave into an electrical signal. Here the fibre nonlinearity and noise is neglected. The unfiltered photon current can be expressed as:

$$\begin{aligned} I(t) &= R_d \left\langle \left| A_o \cos\left(\omega_o t\right)\left[1+\gamma S_I\left(t\right)\right] \right|^2 \right\rangle \\ &= \frac{1}{2} R_d A^2{}_o + \frac{1}{2} R_d \gamma^2 S^2{}_I\left(t\right) + R_d \gamma A_o S_I\left(t\right) \end{aligned} \tag{5.5}$$

Where R_d denotes the responsivity of the photo-diode, and < > denotes time averaging. The linear item from Eq. (5.5) can be addressed as below

$$\begin{aligned} I_{linear}(t) &= R_d \gamma A_o S_I\left(t\right) \\ &= R_d \gamma A_o \sum_{k=n_0}^{N_1} \left(a_k \cos k\Omega t + b_k \sin k\Omega t\right) g_1(t-nT_1) \\ &+ R_d \gamma A_o \sum_{n=1}^{N_2} c_n g_2(t-nT_2) \end{aligned} \tag{5.6}$$

The beating items from Eq. (5.5) can be addressed as below

$$\begin{aligned} I_{beat}(t) &= \frac{1}{2} \mu \gamma^2 S^2{}_I\left(t\right) \\ &= \frac{1}{2} R_d \gamma^2 \left(\sum_{k=n_0}^{N_1} \left(a_k \cos k\Omega t + b_k \sin k\Omega t\right) g_1(t-nT_1) \right)^2 \\ &+ \frac{1}{2} R_d \gamma^2 \left(\sum_{n=1}^{N_2} c_n g_2(t-nT_2) \right)^2 \\ &+ R_d \gamma^2 \sum_{k=n_0}^{N_1} \left(a_k \cos k\Omega t + b_k \sin k\Omega t\right) * g_1(t-nT_1) \times \sum_{n=1}^{N_2} c_n g_2(t-nT_2) \end{aligned} \tag{5.7}$$

The following discussions about the main impairments in LFID are based on Eq. (5.6) and Eq. (5.7).

A) Spectrum leaking interference

According to Eq. (5.5), the detected signal contains linear and beating noise contributions. In this section, the linear contribution is first addressed. From Eq. (5.6), the retrieved signal contains two parts, one is the windowed OOK signal; the other is the OFDM signal with low frequency guard interval. The period ratio, the power ratio and the window function are three crucial factors associated to the spectrum-leaking induced interference (SLII) between user data (OFDM) and signaling data (OOK). In the following, it is assumed that both OFDM and OOK signals have rectangular time windows. The quantitative relationship between the signaling bit rate and the number of reserved subcarriers for low frequency guard interval will be first derived. Then the

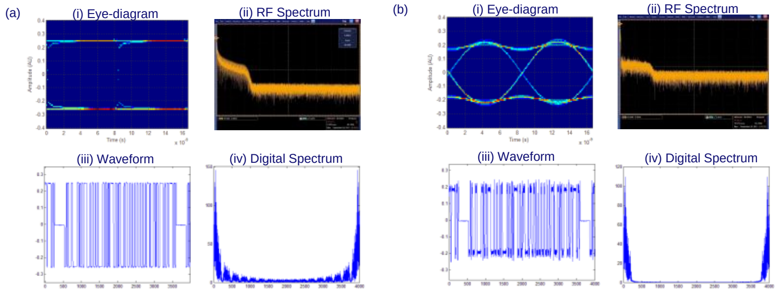

Figure 5.5 The eye diagrams, RF spectrum, waveforms and digital spectrum of 120Mbps OOK signal (a) before rectangular low pass filter; (b) after rectangular low pass filter.

power ratio of OFDM and OOK signals will be discussed to minimize the SLII. Finally, the frequency window functions which can be applied to the OFDM and OOK signals to further reduce the SLII are analyzed.

As assumed above, the time window functions $g_1(t)$ and $g_2(t)$ are rectangular windows. The Fourier transform of the rectangular window can be expressed as follows:

$$G(\omega) = 2\frac{\sin(\omega T)}{\omega} \tag{5.8}$$

The spectrum of the OOK signal can be expressed as:

$$F_{OOK} = \begin{cases} 2C_1\dfrac{\sin(\omega T_2)}{\omega}, & when\ c_n = C_1(\text{'ones'}) \\ 2C_0\dfrac{\sin(\omega T_2)}{\omega}, & when\ c_n = C_0(\text{'zeros'}) \end{cases} \tag{5.9}$$

The expression of OOK signal spectrum suggests that its main energy exists within the first null point ($f = 0.5T_2^{-1}$) and the residual energy is extended infinitely. The Figure 5.5(a-ii) shows the spectrum of rectangular windowed OOK signal generated from an arbitrary waveform generator (Tektronix AWG7122) and retrieved by a real time oscilloscope (Tektronix DPO72004B). The bit rate of the OOK signal is 120 Mb/s. It can be clearly observed that the spectrum of OOK signal is extended further than the first null point. The OFDM signal is usually realized using inverse fast Fourier transform (IFFT) with rectangular windows. Thus the OFDM signal will also introduce the SLII.

Period ratio

The motivation to investigate the period ratio between OOK and OFDM signal is to find out the suitable ratio for preventing their spectrums from overlap within the first null point. The first null point of OOK and OFDM signal can be expressed as:

$$f_{OOK} = \frac{1}{2T_2}$$
$$f_{OFDM} = \frac{N_{GI}}{T_1} - \frac{1}{2T_1} = \frac{1}{2T_1}\left(2N_{GI} - 1\right) \tag{5.10}$$

N_{GI} denotes the amount of subcarriers reserved (carrying no data) for the low frequency guard interval and its value is always larger than zero. To prevent the OOK and OFDM signal from overlapping, the following relationship should be satisfied,

$$f_{OFDM} \geq f_{OOK} \tag{5.11}$$

thus the required period ratio is derived as:

$$\frac{T_2}{T_1} \geq \frac{1}{2N_{GI} - 1} \tag{5.12}$$

Eq. (5.12) serves as one design principle of LFID schemes. The bit rate of OOK is T_2^{-1}. T_1 is usually fixed when the IFFT size and the sampling rate of the digital-to-analog converter (DAC) are given. The factor N_{GI} should be first calculated to satisfy Eq. (5.12) when the bit rate of the signaling data is given. For a practical LFID scheme, the factor N_{GI} will be kept a bit larger.

Power ratio

Another interesting issue of SLII is the power ratio between the OOK and the OFDM signal. For both OOK and OFDM signal, the larger the power is, the larger the signal to noise ratio (SNR) is and also the larger the SLII is. Thus there is a trade-off to optimize the performance of OOK and OFDM signal. The power ratio of OOK and OFDM signal can be expressed as:

$$V_{pp-OOK} = \sqrt{K} \times V_{pp-OFDM} \Big/ \sqrt{PAPR \times N_{used}} \tag{5.13}$$

V_{pp-OOK} and $V_{pp-OFDM}$ are the peak-to-peak voltages of the OOK and OFDM signal, respectively. N_{used} is the number of the used OFDM subcarriers. $PAPR$ is about 14 dB for the OFDM scheme we use. 200 subcarriers are employed in our experiment. The factor K is used to linearly control the power ratio between the OOK and the OFDM signal. If its value equals to 1, the OOK signal is kept at the same power level as one OFDM subcarrier. If its value is larger than 1, the OOK signal is kept at a higher power level and vice versa. Usually QPSK and other higher order formats are utilized in the OFDM subcarriers modulation. The OOK signal has a relatively larger Euclidean distance than the one of OFDM subcarriers. This means that the OOK signal is more tolerant to noise than the OFDM signal. On the other hand, the OOK signal is located in the low frequency part and thus it suffers more beating noise. In the practical LFID scheme, usually a relatively high power level (K=2.5) of the OOK signal is chosen to ensure a good quality of signaling delivery.

Frequency filter to reduce SLII

The SLII is induced by the rectangular window $g_1(t)$ and the spectrum is extended infinitely. The methods to reduce SLII beyond the first null point are mainly low-pass filtering in the frequency domain and windowing in the time domain. Here we use a low-pass filter in the frequency domain to eminently cut off the undesirable spectrum components by using a rectangular low-pass filter (RLPF). The RLPF function is created based on the IFFT and FFT. The waveform is processed by FFT and the spectrum out of the first null point is forced to zero [96]. Then the IFFT is performed to convert the waveform back to the time domain. The comparisons based on eye diagrams, waveform and spectrum before and after RLPF are depicted in Figure 5.5. A 120 Mb/s rectangular OOK signal is generated from the AWG at the sampling rate of 12 GSa/s. And then the waveform is retrieved by using the real time oscilloscope (RTO) at a sampling rate of 50 GSa/s. The eye diagram and RF spectrum of the OOK signal before and after RLPF are both depicted in Figure 5.5(a-i) and (a-ii), and Figure 5.5(b-i) and (b-ii). Comparing the eye diagrams in Figure 5.5(a) and (b), the rising / falling time largely increases with the high-frequency components being distinctly suppressed after RLPF.

To show more details of the spectrum, the waveform retrieved in RTO is processed by employing digital FFT to present the corresponding digital spectrum. It can be observed that the frequency components beyond the first null point are evidently suppressed. The SLII to the OFDM signal can be observed by means of constellation diagrams. The constellation diagrams of

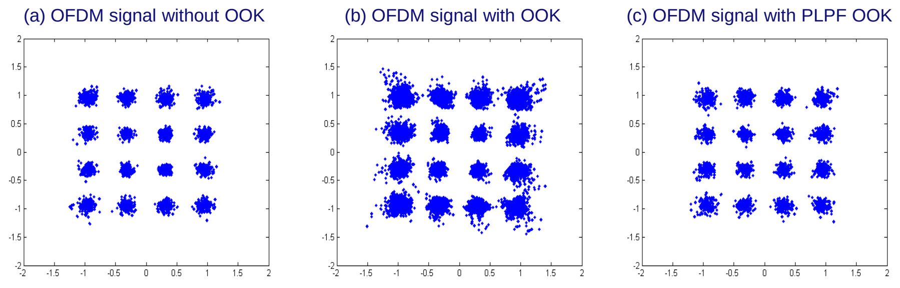

Figure 5.6: The constellations of OFDM signal in different conditions (a) without OOK signal; (b) with rectangular OOK signal; (c) with RLPF OOK signal.

optical BTB OFDM signal without inserted OOK signal, with rectangular OOK signal and with RLPF OOK signal are illustrated in Figure 5.6. The low frequency subcarriers reserved for the guard interval are all blank for three different conditions. No high-pass filters are utilized to suppress the OOK signal. The measurement conditions agree with the description in Table 3. Figure 5.6(b) shows that the SLII seriously degrades the OFDM signal while Figure 5.6(c) shows the RLPF can significantly reduce the SLII. However the operation complexity of RLPF should be taken into account due to FFT and IFFT operations. Considering that the OOK signal only has two symbols, ‘one’ and ‘zero’, the method of look-up-table can be implemented to accelerate the process of RLPF. The two waveforms of ‘one’ and ‘zero’ symbols after low pass filtering can firstly be stored in the memory. And then the stored waveforms can be recalled to form the long bit sequence by assembling the basic waveforms. The assembling process requires only an adding operation and it can remarkably reduce the complexity.

B) Beating induced interference

The beating induced interference (BII) exists universally in the direct detected no frequency guard interval (FGI) optical OFDM systems [97, 98]. The LFID scheme will also introduce extra beating noise. In this section, the BII in the LFID based on the Eq. (5.7) will be discussed. The BII includes mainly three parts, the accumulated beating noise of OFDM subcarriers, the OOK-OOK beating noise and the OOK-OFDM beating noise. The amplitude of the beating noise is proportional to γ^2, so OMI squared. Using Eq. (5.4), the γ^2 can be expressed as:

$$\gamma^2 = \frac{V_{pp}^2}{V_\pi^2 \times PAPR} \qquad (5.14)$$

Considering the high value of PAPR (typically around 14 dB here), the amplitude of beating noise will rapidly decrease when the OMI γ gets smaller. For the scenario of access network with relatively short distance transmission, the OMI is usually small and thus the interference contributed by the beating

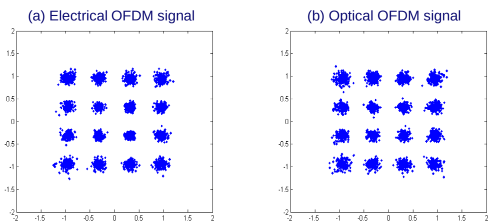

Figure 5.7 The constellations of OFDM signal in different conditions: (a) electrical BTB; (b) optical BTB.

noise is limited. Figure 5.7 shows the constellation diagrams of electrical back-to-back (BTB) OFDM and optical BTB OFDM signals. The bandwidth of the OFDM signal is 4.8 GHz and V_{pp} is 1 V. The other measurement conditions agree with the description in Table 3. The optical BTB OFDM signal will suffer from the beating noise induced by square-law photon detection rather than the electrical one. The constellation diagrams show that the beating noise only degrades the performance a little bit. Thus the beating noise is not a dominant limiting factor of LFID.

C) Detection filters induced distortion

As discussed in Section 5.1.2, the OOK signal is detected in RNs and then separated from the OFDM signal by using an electrical low pass filter (LPF). For the OFDM signal detected in the ONUs, the electrical high pass filters (HPF) should also be considered. Conventional analog filters are preferred due to their low cost and low complexity although these filters will introduce some unwanted distortion. In this section the detection performance of three conventional analog LPFs/HPFs including Butterworth LPF/HPF, Chebyshev I LPF/HPF and elliptic LPF/HPF of order one to four are discussed. To exactly present the properties of such analog filters, all these filters are realized in the digital domain by using direct-form infinite impulse response (IIR). The bandwidth of the combined signal is 4.8 GHz and it is sampled by a 50 GSa/s RTO. The oversampling is helpful to accurately perform the analog filtering. The signaling control channel inserted in the OFDM signal over 12.5 km single mode fibre (SMF-28) is detected and separated by using different LPFs and HPFs as mentioned above. This fibre length is chosen because it matches a typical distance between two neighboring RNs. Actually the system is robust

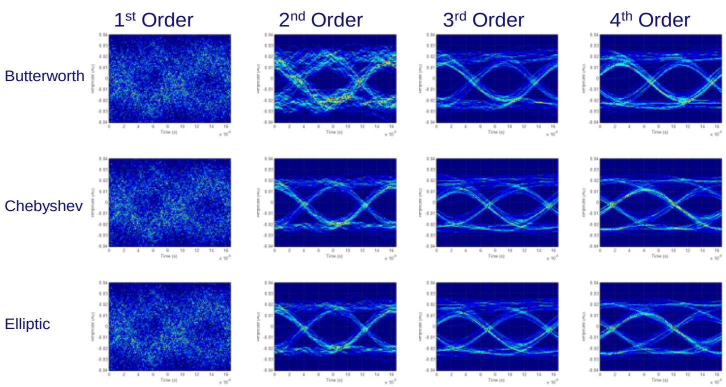

Figure 5.8 The eye diagrams of the signaling inserted OFDM signal over 12.5 km SMF with different detection low pass filters.

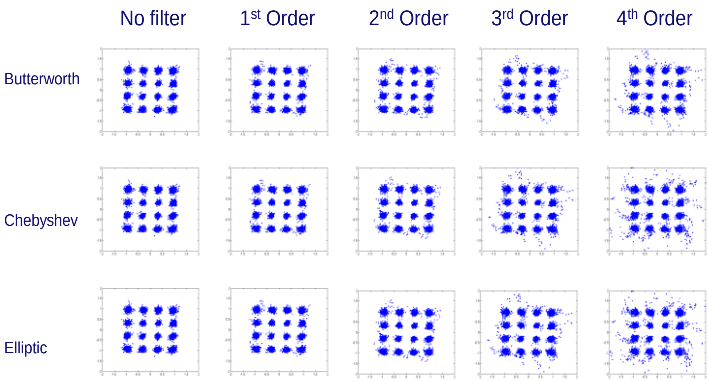

Figure 5.9 The constellations of the signaling inserted OFDM signal over 12.5 km SMF with different detection high pass filters.

even if the distance is extended to 100 km. The optical power launched into and out of the fibre is 3 dBm and -1.5 dBm, respectively. The other conditions match with the description in Table 3. The eye diagrams of the OOK signal after LPFs are depicted in Figure 5.8. The -1 dB pass band frequency is 120 MHz equal to the first null point of the OOK signal. For all types of LPFs, the eye diagrams get clearer as the orders increase because the high order LPFs can better suppress the out-of-band interference. The ripple of '1'line and '0'line in the eye diagrams declines when the out-of-band interference reduces. This will reduce the decision error probability. On the other hand, the rise and fall time is another issue related to the eye diagram quality. As shown in Figure 5.8, Butterworth LPFs retain the shortest rise and fall time for 2 to 4 orders.

The constellations in Figure 5.9 show the quality of the OFDM signal with and without HPFs over 12.5 km SMF. The scattering of the signal constellation points gets worse as the orders of HPFs increase. The constellation without HPF is better than other cases with HPFs. The corresponding bit error rate (BER) of Figure 5.9 is shown in Figure 5.11. The '0' order denotes the case without HPF. It can be clearly seen that the BERs all get worse. This is largely caused by the high order filters which introduce phase distortion, degrading the performance of the pilots assisted equalization of the OFDM signal. The BERs of 3rd and 4th order Butterworth HPFs are better than the other 3 and 4 order HPFs because their phase response is relatively smooth. The spectrum of OOK can be suppressed even without any HPF. This is because the spectrum of OOK can be discarded after FFT (which is needed anyhow for OFDM demodulation), and the higher part can be maintained, which performs a rectangular HPF function.

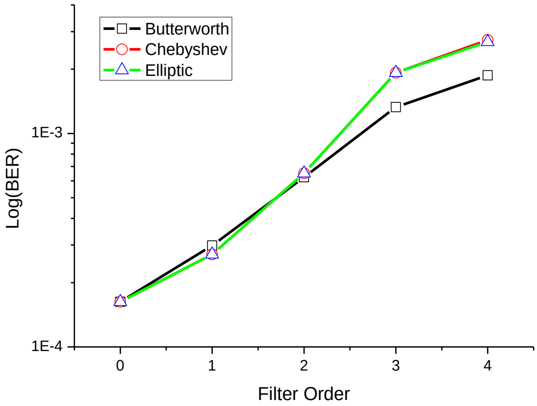

Figure 5.11 The BERs after different high pass filters.

5.1.4 Experimental setup and results

Figure 5.10 shows the experimental setup to demonstrate the LFID scheme for a reconfigurable WDM-OFDM-OAN. The detailed experimental conditions are shown in Table 3. The OFDM signal is generated from the Tektronix AWG 7122B at the sampling rate of 12 GSa/s. The size of IFFT is 256 and the

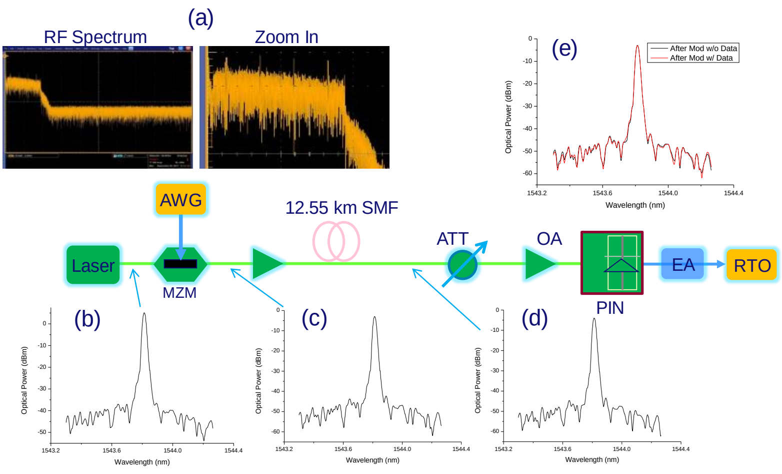

Figure 5.10 Experimental setup for low frequency insertion and detection scheme (LFID) of signaling. Laser: distributed feedback laser, MZM: Mach-Zehnder modulator, AWG: arbitrary waveform generator, SMF: single mode fibre, ATT: optical attenuator, OA: optical amplifier, PIN: p-i-n photo-diode, EA: electrical amplifier, RTO: real time oscilloscope.

Table 3 The basic parameters used in the experiment.

Fibre	Type	SMF-28
	Dispersion	16.75ps/nm /km
	Attenuation	0.19dB/km
MZM	Vpi	4.2V
	Extinction Ratio	>20dB
PD	Electrical Bandwidth	75GHz
	Responsivity	0.6A/W
AWG	Sampling rate	12GSa/s
	Amplitude (peak-peak)	1V
Optical Power	In fibre	3dBm
	Out fibre	-1.5dBm
	In PD	1dBm
DFB	Wavelength	1543.81nm
	Power	5.2 dBm
EA	Bandwidth	13.5GHz
	DC supply	5.6V
RTO	Sampling rate	50GSa/s

subcarriers used for data, pilots and high-frequency guard band (HFGB) are 192, 8, and 56, respectively. Note that the HFGB is used to suppress the out-of-band spectrum of the OFDM signal which is different from the low frequency guard interval for signaling insertion as discussed before.

The subcarriers are arranged to satisfy the Hermitian symmetry with respect to their complex conjugate counterparts to allow the real-valued IFFT output. The period of an OFDM symbol (T_1) is 21.33 ns. The symbol rate for each subcarrier is 46.875 MS/s. 16QAM is employed in the data subcarrier modulation. The cyclic prefix is 1/8 of an OFDM period, which corresponds to 32 samples in every OFDM symbol. One training symbol is inserted in front of 64 data OFDM symbols for the timing and coarse estimation. The bit rate of the OOK signal is 120 Mb/s and the period of one OOK symbol (T_2) is 8.33 ns. Using the Eq. (5.12), the number of closed low frequency subcarriers (N_{GI}) is 3. Thus the three lowest subcarriers are closed to avert spectrum overlap within the first null point. The net bit rate of the OFDM signal is 15.265 Gb/s. The power level of the OOK signal is 2.5 times of the one of an OFDM subcarrier to allow adequate performance of signaling delivery. According to Eq. (5.13), the amplitude (Vpp) of the OOK signal is set to 30 mV while Vpp of the OFDM signal is 1 V. The RF spectrums of the combined OOK and OFDM signal are depicted in Figure 5.10(a).

The 5.2 dBm optical carrier from a commercial distributed feed back (DFB) laser is modulated to generate optical OFDM signal. A single electrode Sumitomo MZM with 10 GHz bandwidth and 4.2 V drive voltage (Vpi) is biased in the middle of its power transfer curve. The optical spectra before and after the MZM are depicted in Figure 5.10(b) and (c) respectively. The optical power after modulation is -2.9 dBm. The optical spectra after the MZM with and without data modulation are compared in Figure 5.10(e). The black line denotes the spectra without data modulation while the red line denotes the one with data modulation. Only a little difference can be observed due to the low OMI. The optical OFDM signal is amplified to 3 dBm and then launched into a span of 12.5 km SMF. The optical power after transmission is -1.5 dBm and then is attenuated to measure power penalty. An Eigen Light 410 is used as an optical attenuator and in-line optical power monitor. The attenuated optical signal is then pre-amplified by a commercial EDFA and then fed to a 75 GHz photo-diode. The converted signal is amplified by an electrical broadband amplifier with bias voltage of 5.6 V. The amplified signal is then sampled by a commercial real time oscilloscope and processed off-line.

The OOK signal (signaling) is detected by using a 4-order Butterworth LPF with 120 MHz 1 dB pass bandwidth. The curves of its quality factor values (Q Factor) versus received optical power BTB with 12.5 km SMF, and with 100 km SMF transmission are depicted in Figure 5.12(a). The power penalty at Q=5.4 (corresponding BER is about 3.44×10^{-8}) is less than 0.35 and 0.85 dB for 12.5 km and 100 km. The BERs of the OFDM signal with and without inserted

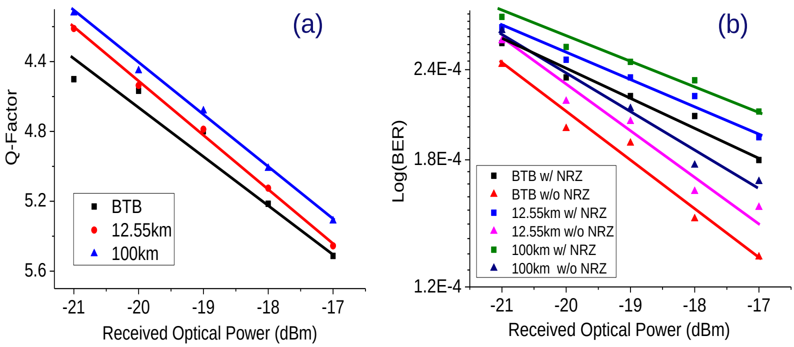

Figure 5.12 The curves for (a) Q factor of OOK signal (signaling) versus received optical power, and (b) BER of OFDM signal (user data) versus received optical power.

OOK signal are measured optical BTB, over 12.5 and 100 km SMF as shown in Figure 5.12(b). No high-band pass filter is implemented to suppress the OOK signal. The OOK insertion induced power penalty for BER=2.4×10^{-4} is 0.9, 1.1 and 1.5 dB for BTB, 12.5 km and 100 km respectively. When the transmission of 100 km is considered, the OOK signaling adds only 1.5 dB, demonstrating that this signaling insertion and detection scheme does not increase system penalty considerably.

5.1.5 Conclusion

A simple signaling insertion and detection scheme for reconfigurable WDM-OFDM optical access networks is proposed. The signaling is synchronously inserted into OFDM signals without any extra optical wavelength or high-speed logical operation. The experimental results show that, when the transmission of 100 km is considered, the OOK signaling adds only 1.5 dB power penalty, demonstrating that this signaling insertion and detection scheme does not increase system penalty considerably.

5.2 Signaling delivery for optical mm-wave data

In this section, the indoor 60 GHz RoF systems are discussed. The efficient and simple signaling delivery is of demand. The main challenge is to down convert the control signaling from the 60 GHz carrier frequency, which may introduce complicated electronics in the radio access point. By exploring the envelop detection feature of the photodiode, it is possible to obtain the low bandwidth data modulated on the 60 GHz mm-wave by a low-speed photodiode. The experiment is carried out for a 60 GHz RoF system, however, the concept of LFID can be extended to all IF/RF signals of an indoor RoF system.

5.2.1 Motivation

Indoor networks should provide the control signaling channel for functions related to data communication like optical routing, and also for the sensors and actuators served for indoor automation. Therefore, it is pivotal to have signaling information delivery for indoor networks. The bit rate of signaling channel is usually set to 1% of user data to allow enough budgets for future applications. Traditionally, the signaling data is embedded into designated time slots. The process of signaling insertion and detection is consequently operated at the full line rate speed. For RoF systems, one more process of down conversion from radio frequency to baseband is required. This will introduce additional complexity and instability to systems. A separate wavelength for signaling can encounter such problem; but such system will be more complicated and extra synchronization is of demand. In this section, a simple low-cost signaling insertion and detection scheme having capability to achieve synchronization through digital frequency division multiplexing (D-FDM) is proposed. To suppress the inter-channel interference (ICI) between signaling and user data, digital pulse shaping is employed.

5.2.2 Operation principle

In this section, the two major techniques employed in the signaling delivery of 60GHz RoF system are discussed below.

A) Digital frequency division multiplexing and digital pulse shaping

The principle of D-FDM is depicted in Figure 5.13. Low speed Polar non-return-to-zero (Polar-NRZ) signal for control signaling is coupled with OFDM signal by simply adding their digital values in time domain before digital-to-analog conversion as shown in Figure 5.13(a). This process will synchronize the signaling with OFDM signal, which is extremely important in time-varying application like optical routing. To reduce ICI, as shown in Figure 5.13(b), the OFDM subcarriers overlapping the main lobe of the Polar-NRZ spectrum are reserved (carrying no bits). This is because the main power of the Polar-NRZ signal is within its main lobe. To further reduce ICI, digital pulse shaping is employed. Pulse shaping is used to cut off or roll off unwanted spectrum without additional inter-symbol interference at sampling instants. The digital pulse shaping is achieved by convolving the normalized *sinc* function $f(t/T)=sin(\pi t/T)/(\pi t/T)$ with the Polar-NRZ signal. Its cutoff frequency is $f_{cutoff}=0.5\times T^{-1}$,where T is the period of the symbol rate of the Polar-NRZ signal. For practical implementation of the *sinc* function, its tails are truncated to reduce the number of discrete samples. The *sinc* function is chosen since it can

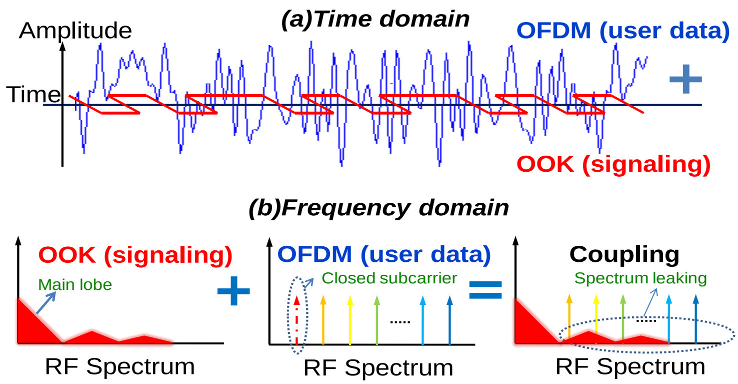

Figure 5.13 Principle of D-FDM for: (a) time domain and (b) frequency domain.

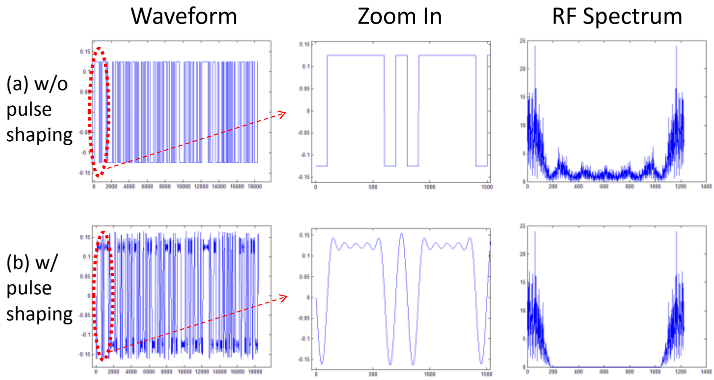

Figure 5.14: Process of pulse shaping: (a) without and (b) with pulse shaping.

completely suppress unwanted spectrum and introduce little distortion to the remained part. The waveforms and RF spectrum with and without pulse shaping are shown in Figure 5.14.

Without pulse shaping, the waveform of Polar-NRZ signal is rectangular and its spectrum is extended far beyond the 1st null. With pulse shaping, the spectrum of Polar-NRZ signal is well confined between DC - 1st null. To avoid complicated convolution process, the waveform of a convolved “1” is placed in the look-up table and recalled when “1” appears. Its inverted waveform is recalled when “-1” appears. This process is for downlinks, and analog FDM can be used for uplinks.

B) Low frequency detection for RoF signal

In this section, a mathematical model will be built to analyze the low frequency detection (LFD) of the RoF signal. The electrical field of the optical mm-wave carrier with the OFDM signal modulated can be expressed as [16]:

$$E(t) = \left[A_{+1} \times \cos(\omega_o + \omega_m)t + A_{-1} \times \cos(\omega_o - \omega_m)t\right] \times (1 + \gamma S(t)) \quad (5.15)$$

where A_{+1} and A_{-1} denote the amplitudes of upper and lower sidebands, respectively, ω_o and ω_m denote the angular frequency of the optical carrier and driving LO. The optical modulation index is denoted by γ. $S(t)$ is the presentation of the OFDM signal, which can be expressed as:

$$S(t) = \sum_{k=1}^{N} \left(a_k \cos k\Omega t + b_k \sin k\Omega t\right) \quad (5.16)$$

where N denotes the number of subcarriers in an OFDM symbol, Ω is the 1st sub-carrier frequency, $k\Omega$ is the frequency of k_{th} subcarrier. a_k and b_k represent the complex symbols of the in-phase and quadrature components for the k_{th} subcarrier. After square-law detection of the photo-diode, the output current can be expressed as [16]:

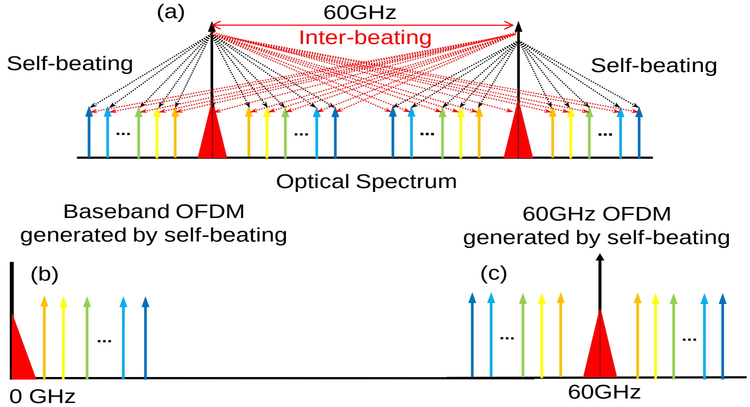

Figure 5.15 Beating process and low frequency detection: (a) optical spectrum of data modulated optical mm-wave; (b) RF spectrum of detected BB signal; (c) RF spectrum of detected 60 GHz signal.

$$I(t) = \frac{1}{2}\mu(A_{+1}^2 + A_{-1}^2)[1 + 2\gamma S(t) + \gamma^2 S^2(t)] + \mu A_{+1}A_{-1}\cos(2\omega_m t)[1 + 2\gamma S(t) + \gamma^2 S^2(t)] \tag{5.17}$$

It is obvious that the baseband (BB) OFDM signal is identical to the OFDM signal at mm-wave carrier. Thus the BB OFDM signal can be detected to get the signaling data. As discussed in Section 5.1.2, the signaling data is inserted in the lower frequency part of the BB OFDM signal and thus a low speed (100 MHz level) PD can detect the signaling data.

The principle of low frequency detection is illustrated in Figure 5.15. The optical spectrum of the 60 GHz optical mm-wave with the OFDM signal modulated is principally depicted in Figure 5.15(a). The two vertical black arrows denote the two sidebands of optical mm-wave signal. The colored arrows around them denote the subcarriers of modulated OFDM signal. The beating process includes two parts, namely, self-beating and inter-beating. Self-beating refers to beating between one sideband and the subcarriers around it, which generates the baseband (BB) OFDM signal shown in Figure 5.15(b). The self-beating process allows low frequency detection of the OFDM signal on the 60 GHz optical mm-wave. Inter-beating refers to beating between one sideband and subcarriers around the other sideband which generates the 60 GHz OFDM signal shown in Figure 5.15(c). Since signaling (Polar-NRZ signal) is inserted in the low frequency part of the BB OFDM signal as shown in Figure 5.15(b), the PD bandwidth required for detection of signaling (Polar-NRZ signal) is only a little higher than the signaling bandwidth. The detected signaling (Polar-NRZ signal) can be further processed using low speed logical circuits. Thus high-speed PDs, logical circuits, and down conversion schemes can be avoided.

5.2.3 Experimental setup, results and discussion

Figure 5.16 shows the experimental setup to demonstrate the proposed signaling insertion and detection scheme in a 60 GHz OFDM-RoF system. The OFDM signal is generated from the Tektronix Arbitrary Waveform Generator (AWG) 7122B at 10 GSa/s. The size of the IFFT is 256 and the subcarriers used for data, pilots and high-frequency guard interval are 192, 8, and 56, respectively. The subcarriers are arranged to satisfy the Hermitian symmetry with respect to their complex conjugate counterparts to allow the real-valued IFFT output. The period of an OFDM symbol is 25.6 ns. The symbol rate for each subcarrier is 39 MS/s. 16QAM is employed for subcarrier modulation. The cyclic prefix is 1/8 of an OFDM period, which corresponds to 32 samples in every OFDM symbol. One training symbol is inserted in front of 64 data OFDM symbols for timing and channel estimation. The net bit rate of OFDM signal is 12.72 Gb/s. The bit rate of the Polar-NRZ signal is 100 Mb/s and one Polar-NRZ symbol lasts for 10ns. The f_{cutoff} of the *sinc* function is set to 100MHz and its digital waveform is sampled at f=100 ×f_{cutoff} agreeing with the sampling rate of OFDM signal. The truncation size of the sinc function is 10 ×T. The three lowest frequency subcarriers are closed reserving a bandwidth of 117 MHz.

The V_{pp} of the Polar-NRZ signal is set to be 30 mV while the V_{pp} of the

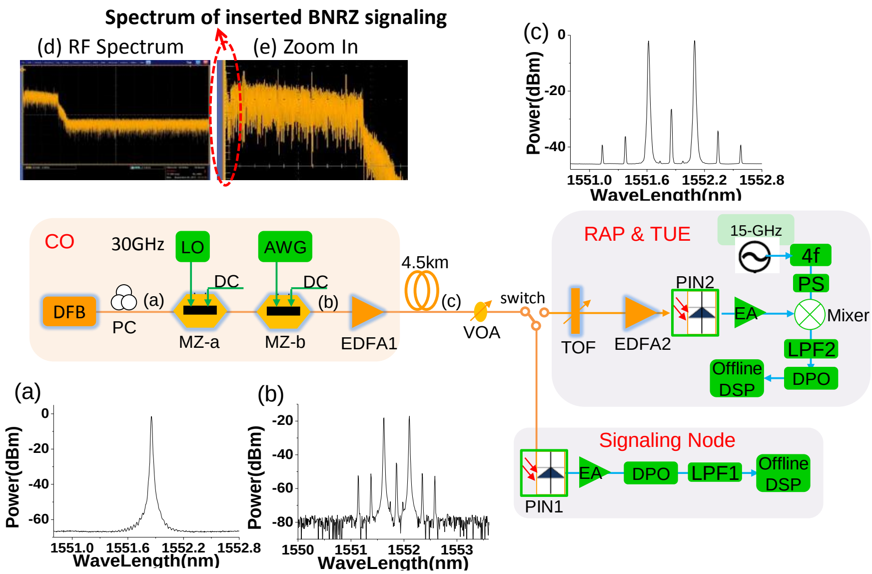

Figure 5.16 Experimental setup and measured results: (a)-(c): measured optical spectrum; (d)-(e): measured RF spectrum.

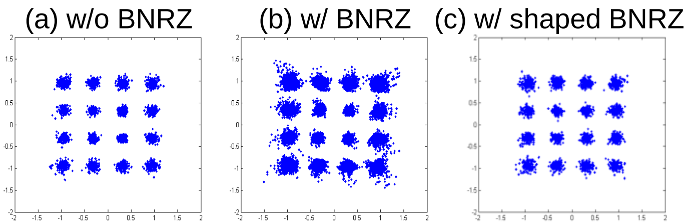

Figure 5.17 Constellations of OFDM signals (a) without and (b) with Polar-NRZ, (c) with pulse shaped Polar-NRZ.

OFDM signal is 1 V. The RF spectrums of the combined signal of Polar-NRZ and OFDM are depicted in Figure 5.16(d) and (e). A DFB-laser with 1 dBm launch power, is modulated to generate the 60 GHz optical mm-wave via a MZM (MZ-a) biased at the null point with a 30 GHz electrical local oscillator (LO). A MZM (MZ-b) is used for the OFDM signal modulation. The optical spectrum of the OFDM signal modulated on an optical mm-wave is depicted in Figure 5.16(b). The optical signal is amplified to 0 dBm before launched in a 4.5 km single mode fibre (SMF). After transmission, its received optical power (ROP) is -1.5 dBm with the optical spectrum shown in Figure 5.16(c). A variable optical attenuator (VOA) is used to control the ROP for measurement. Two optical receivers are constructed for both signaling node, and antenna point (RAP) and terminal users (TU). The signaling node receiver comprises a 10 GHz photo-diode (PD, PIN-1) and a 6 GHz low noise amplifier (LNA1). The signal after LNA1 is filtered by a 4-order Butterworth LPF (LPF1) with 100 MHz 1 dB pass bandwidth and then sampled at 1.25 GSa/s by a real time oscilloscope (DPO). The RAP-TU receiver contains a preamplifier (EDFA-2) and a 75 GHz PD (PIN-2). After the PD, the electrical 60 GHz OFDM signal is generated and amplified by an 8 GHz narrow band amplifier centralized at 60 GHz. The 60 GHz OFDM signal is then down converted via a 60 GHz electrical mixer in combination with a 60 GHz LO. The 60 GHz LO is generated from an electrical frequency quadruple multiplier cascaded with a 15 GHz microwave source. An electrical phase shifter (PS) is used to adjust the phase of the 60GHz LO. A LNA (LNA2) is followed by a 6GHz low-pass filter (LPF2) to retrieve the BB OFDM signal which is further sampled at 25GSa/s by a DPO and processed off-line. The system evaluation is carried out to assess the followings: (i) the impact to the OFDM signal induced by signaling insertion; (ii) evaluation of low-pass filters for signaling detection; (iii) the EVM performance of OFDM before and after fibre transmission; (iv) the Q factor of signaling data before and after fibre transmission. The constellations of OFDM signal over 4.5 km SMF are depicted in Figure 5.17 with ROP of -16 dBm, which include OFDM signals (a) without Polar-NRZ, (b) with no-shaped Polar-NRZ and (c) with pulse shaped Polar-NRZ. Comparing Figure 5.17(a) and (b), it is evident that the

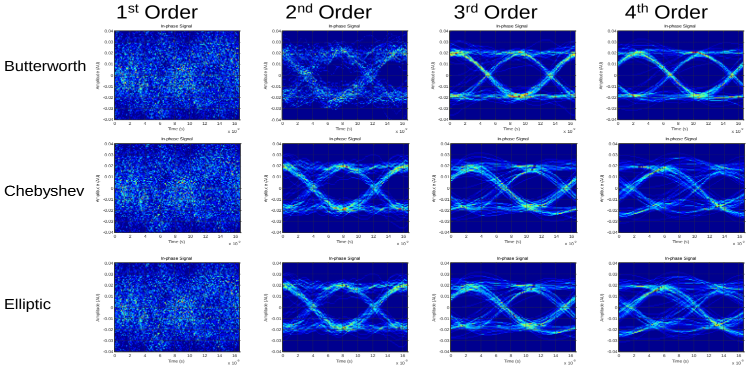

Figure 5.18 The eye diagrams of the signaling inserted OFDM signal at 60 GHz optical mm-wave over 4.5 km SMF with different detection low pass filters.

inserted Polar-NRZ introduce interference to the OFDM signal whereas for the pulse shaped Polar-NRZ, the interference is not obvious.

Here the detection performance of three traditional analog LPFs/HPFs including Butterworth LPF/HPF, Chebyshev I LPF/HPF and elliptic LPF/HPF with the 1st to the 4th order is discussed. To exactly present the properties of such analog filters, all these filters are realized in the digital domain by using direct-form IIR. Their 1 dB pass band frequencies are all 100 MHz equal to first null point of the Polar-NRZ signal. The bandwidth of the combined signal is 4 GHz and sampled by a 50 GSa/s RTO. The oversampling is helpful to accurately perform the analog filtering. The signaling inserted to the OFDM signal at the 60 GHz optical mm-wave and transported over 4.5 km single mode fibre (SMF-28) is detected and separated by using different LPFs and HPFs as mentioned above. The signal is detected with received power of -16 dBm. As shown in Figure 5.18, for all types of LPFs, the eye diagrams get clearer as the orders increase because the high order LPFs can better suppress the out band interference. The background color is intentionally set to blue for illustration purpose. The ripple of the '1'line and the '0'line in the eye diagrams declines as long as the out band interference reduces. This will reduce the decision error probability. On the other hand, the rise and fall time is another issue related to the eye diagram quality. As shown in Figure 5.18, Butterworth LPFs retain the shortest rise and fall time for the 2nd to the 4th order. Thus the following measurement for signaling data is based on the 4th order Butterworth filter.

The EVMs of the OFDM signal with and without inserted Polar-NRZ signal are measured for optical BTB and over 4.5 km SMF. Plots are shown in Figure 5.19(a). No high pass filter is implemented to suppress the Polar-NRZ signal. The Polar-NRZ insertion induced power penalties for the EVM of 11.2% are both 0.8 dB for BTB and 4.5 km transmission demonstrating that this signaling

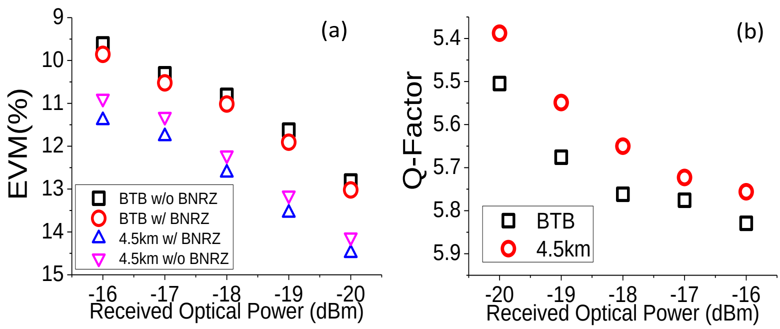

Figure 5.19 Measured system performance for BTB and 4.5 km SMF transmission: (a) EVM for user data, (b) Q factor for signaling data.

insertion and detection scheme does not increase system penalty considerably. The power penalty for the EVM of 11.2% is 1.7 dB after 4.5 km transmission for Polar-NRZ inserted OFDM. This is mainly due to the frequency selective fading for double sideband modulation. The curves of the Q factor of Polar-NRZ signal versus ROP for BTB and 4.5 km SMF transmission are depicted in Figure 5.19(b). The power penalty at Q=5.5 (corresponding BER is about 1.95×10^{-8}) is 1.2 dB for 4.5 km SMF transmission.

5.2.4 Conclusion

A signaling insertion and detection scheme based on digital frequency multiplexing and pulse shaping for 12.7 Gb/s throughput 60 GHz indoor fibre-wireless networks is demonstrated. The power penalty due to signaling insertion is less than 0.8 dB. Based on achieved results, it is proved that the proposed scheme can provide a reliable and low-cost signaling delivery channel for 60 GHz indoor fibre-wireless networks.

5.3 Summary

In this chapter, a novel simple control signaling delivery for the gateway of indoor networks is studied. For passive optical networks (PON), by using low frequency insertion and detection techniques, the signaling can be detected and processed by a low-speed receiver and logical circuit. The design principle and impairment elimination techniques are performed based on the theoretical analysis and experiment verification. The experiment has demonstrated that this scheme does not add a significant penalty to the performance of the OFDM signals. For the IF and RF signals, by exploring the envelop detection feature of photodiodes, a signaling insertion and detection scheme based on digital frequency multiplexing and pulse shaping is demonstrated for a 12.7 Gb/s throughput 60 GHz indoor fibre-wireless network. The power penalty due to signaling insertion is less than 0.8 dB.

Based on the achieved results and the simplicity, it is proved that the proposed schemes could provide reliable and a low-cost signaling delivery system for indoor fibre wireless networks.

Chapter 6 Optical Radio Beam-steered Radio-over-Fibre System

In this chapter, the optical radio beam steered radio over fibre systems (ORBS-RoF) are experimentally investigated for indoor fibre wireless networks. In Section 6.1, a brief review of reported optical radio beam steering systems based on optical true time delay techniques is presented. In Section 6.2, the ORBS-RoF systems are investigated based on bulk OTDLs. The basic parameters regarding the phased antenna array and the optical true time delay induced beam steering are studied. The data transmission up to 4Gb/s data rate is successfully demonstrated in such system. In Section 6.3, the ORBS-RoF system based on an integrated spectral-cyclic arrayed grating waveguide feedback loop (SC-AWG-loop) is experimentally investigated. The involvement of the integrated SC-AWG-loop allows a compact footprint, much reduced cost and flexible remote control for the indoor ORBS-RoF system.

6.1 Background of ORBS-RoF

A lot of research has been carried out to exploit wireless capacity. Unlike spatial multiplexing which requires complicated digital signal processing, beam steering (BS) directs signals to the desired user with minimum interference. Phased array antennas (PAAs) are widely considered as the best candidate for microwave beam-steering due to their fast steering and compactness [56]. The operational bandwidth of a conventional PAA is limited. Specifically, a severe limitation is often caused by the use of phase shifters to scan the beam, which results in beam deformations ("squint") in the measured antenna pattern. The use of true time delay (TTD) technology potentially eliminates such bandwidth restriction, as it provides a theoretically frequency-independent time delay on each channel of the array [57]. Standard TTD technology typically consists of digitally-switched transmission line sections wherein weight, loss and cost increase rapidly with increased operational frequency and/or phase tuning resolution. These issues can be avoided by adopting optical TTD radio beam steering (OTTD-RBS) as reported in [58-61]. Especially, OTTD can be integrated into RoF systems which are the key technology for next generation wireless communication systems, with low additional cost. The RoF technique is highly appreciated for ultra-broadband distributed pico-cell indoor networks with simplified architectures as discussed in Chapter 2. By reusing the RoF link, the OTTD-RBS can be realized with a few additional components. The first applications of OTTD-RBS in a RoF network, Ref. [99] reports a 19 GHz indoor RoF system with OTTD-RBS. A significant sensitivity improvement was observed with 1 Gb/s transmission. Later Ref. [100] reports the delivery of an advanced modulation format (OFDM) over the same system.

6.2 ORBS-RoF system based on bulk OTTD

The simulation results presented in this section assumed that the transmitter and receiver components were operating at the optimal points and no imperfections were present. In practice, deviations from optimal conditions and imperfections are always present, especially in complex structures such as multilevel differential transceivers. It is, therefore, important to estimate the robustness of a proposed modulation format against these impairments. The effect of non-ideal operating conditions of the transmitter is shown with the coded 16QAM format, while receiver imperfections are studied with phase pre-integrated 16QAM.

6.2.1 Principle of ORBS based on OTTD

As shown in Figure 6.1(a), the OTTD-RBS PAA includes a group of individual radiators (antennas), which are oriented in the linear spatial configuration. With equal magnitudes and progressive phases, its far field pattern can be expressed as:

$$E(\theta) = AF(\theta) \times P_e(\theta) \tag{6.1}$$

where $P_e(\theta)$ and $AF(\theta)$ are the far field pattern of element antennas, and the array factor, correspondingly. The properties of $P_e(\theta)$ and $AF(\theta)$ will be explored in the following sections.

A) Bandwidth and far field pattern (FFP) of aperture antennas

The aperture antennas (AA) are used as element antennas in our experiment. As a kind of mature and well-studied structures, AAs exhibit a flat response feature within its pass-band. According to its datasheet, the AA used in our experiment keeps a flat response from 14.2 to 26.5 GHz. The transmission bandwidth is measured using a vector network analyzer (VNA) as shown in

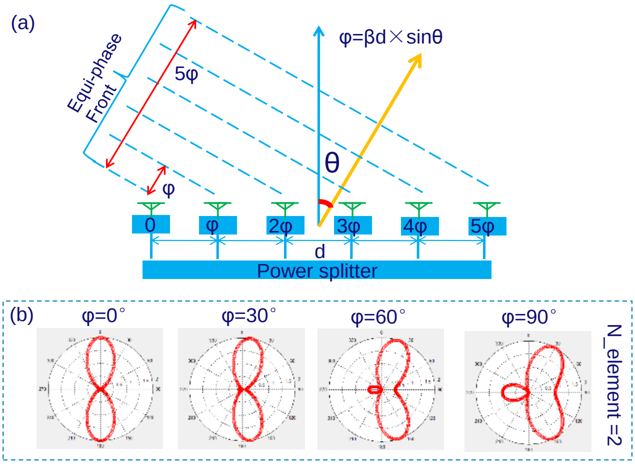

Figure 6.1 Principle of array factor and beam steering: (a) illustration of array factor derivation; (b) beam steering enabled by phase shift (or delay).

Figure 6.2. Since the frequency range of the employed VNA is from 130 MHz to 20 GHz, the frequency response beyond 20 GHz is not presented. Based on the response curve, the flatness is within 4 dB in its pass band. In the antenna array, the mutual coupling measured is less than -30 dB, which results in low cross-talk and accurate beam-steering. Moreover, the aperture antennas are semi-omni-directional, which is suitable for large coverage applications. The simulated far field pattern (FFP) of an AA used in our experiment is depicted in Figure 6.3. The simulated frequency is 19 GHz. The 3-D FFP of AA is depicted in Figure 6.3(a) and the different colors present different antenna gains (dBi). It covers the whole hemisphere with a small deviation. The antenna array is oriented in the x-axis of the element antennas, thus the 2-D FFP on the x-z plane should be investigated, which is shown in Figure 6.3(c). Its gain difference of the element AA will introduce the gain imbalance to the array synthesized FFA according to Eq. (6.1). As shown in Figure 6.3(c), the 3 dB angle width of the 2-D FFA in x-z plane is 80˚ (-40˚ ~ 40˚). It means that the maximum 3 dB received power difference occurs in a range of 80˚. This is acceptable for indoor scenarios. The gain difference induced received power imbalance will be observed experimentally in the following.

B) Array Factor and Beam-steering

As shown in Figure 6.1(a), the array factor can be expressed as:

$$AF(\theta) = \sum_{n=1}^{N} I_n \exp(-j\beta n d \sin\theta) \tag{6.2}$$

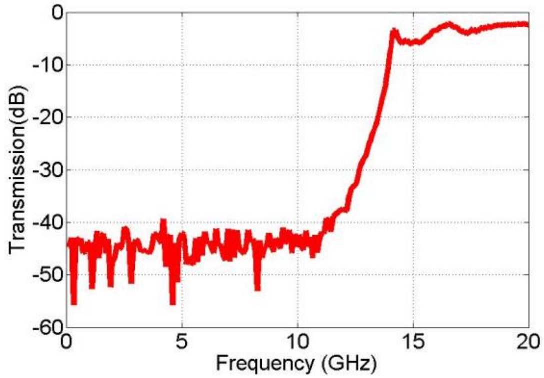

Figure 6.2 The measured transmission curve vs. frequency for aperture antenna used in the experiment.

where $I_n=exp(jn\varphi)$ denotes progressive φ radian phase shifts of each radiators. In the OTTD-RBS system, φ can be further expressed as: $\varphi=t/T_c$, where t is the delay controlled by the OTTD scheme, and T_c is the period of the carrier frequency. β is the propagation constant of the radiated microwave carrier, and can be expressed as: $\beta= 2\pi/\lambda$, where λ is the wavelength of the radiated microwave carrier. θ denotes the scanning angle and d denotes the distance between two radiators. Thus the main lobe of the beam (maximum of $AF(\theta)$) in space can be controlled by adjusting the progressive phase shift of the excitation signals to each individual element. The main lobe of $AF(\theta)$ can be achieved when the phase shifts are equal to the propagation induced phase delays, namely $\varphi=\beta d\times sin\theta$. An intuitive understanding is that the beam directs to one destination where all signals from different radiators arrive with the same phase

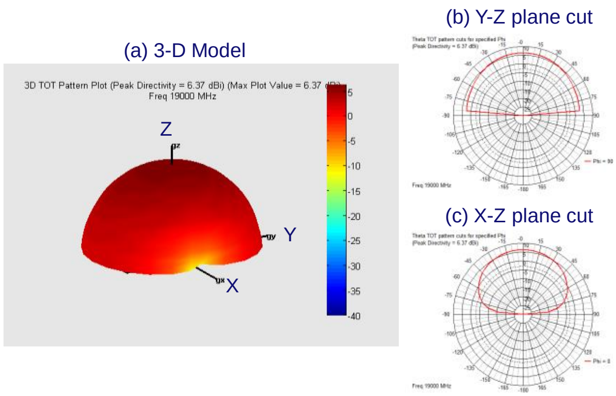

Figure 6.3 (a) 3-D far field pattern (FEP) of aperture antenna; (b) 2-D FEP (Y-Z plane), (c) 2-D FEP (X-Z plane) of aperture antenna.

(or "at the same time" for true time delay). As an example shown in Figure 6.1(b), the pattern of a two-radiator (ideal omni directional antennas) array antenna with different phase shifts in between is simulated. The wavelength in the simulation is 15.8 mm (19 GHz) and the distance between the elements is 7.9 mm. It can be seen that the main lobes of the beam change when the phase shift changes.

C) Phase shift RBS and true time delay RBS

As shown in Figure 6.4(a), for traditional PS schemes, the phase of the microwave carrier (19 GHz) is shifted before its data modulation. For the OTTD scheme shown in Figure 6.4(b), the microwave carrier is modulated by data and then is modulated on an optical carrier. The optical signal is then split and delayed by an OTTD before its conversion to an electrical signal via a photodiode (PD). PS schemes are more practical than TTD schemes in electrical domain because phase control can be done by many methods without additional loss. The beam skew in a PS scheme is investigated by a 1-D array of 2 and 8 element omnidirectional antennas at 19 GHz with 5 GHz bandwidth IF signal modulated. The 1-D array is linear with 0.5λ element distance and 76° element phase shift. As shown in Figure 6.4(c), the patterns of the frequency component at 14 GHz, 19 GHz and 24 GHz are plotted as the red dash line, the black solid line and the blue dash line correspondingly. It is obvious that the beams direct at different angles for different frequencies. This is so-called 'beam squint' which will cause serious signal distortions. For the OTTD solution, the delay is set to 11.1 ps (equal to 76 ° phase shift at 19 GHz), and the patterns at 14, 19 and 24

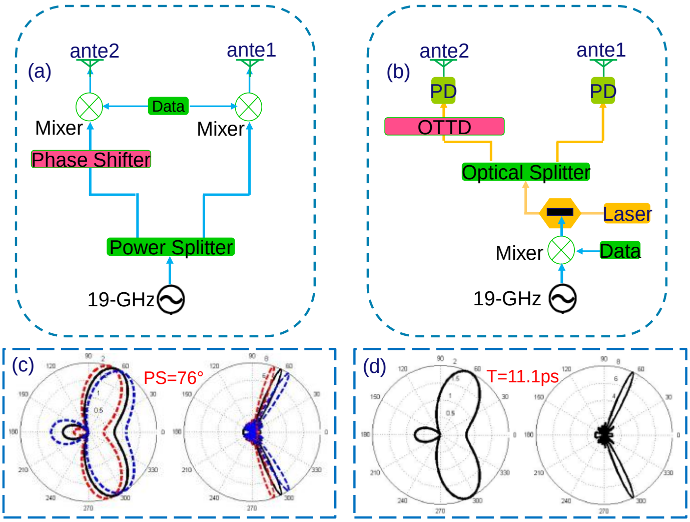

Figure 6.4 (a) Phase shifted PAA and (c) its FEP for for 14, 19, 24 GHz; (b) Optical true time delay PAA and (d) its FEP for 14, 19, 24 GHz.

GHz are the same as shown in Figure 6.4(d). It is clear that OTTDs are preferred for broadband applications.

6.2.2 Experimental results and discussion

Figure 6.5 shows the proof-of-concept experimental setup for the proposed OTTD-RBS in an OFDM-RoF system. A 3-dBm optical carrier at 1556.96 nm is generated from a commercial semiconductor laser diode with its spectrum shown in Figure 6.5(a) is modulated with a 19 GHz sinusoidal signal via a MZM (MZ-a) biased at its linear range to generate an optical mm-wave. The 19 GHz carrier is chosen because of the facility availability in our lab. The 1Gb/s OOK signal and 4Gb/s orthogonal frequency division multiplexing (OFDM) signal are modulated on the generated optical mm-wave via MZ-b one after another. The OOK signal is with a pseudorandom binary word length of 2^{15}-1. Details of OFDM signal is described below. An erbium-doped amplifier (OA) is used to compensate insertion losses of the MZMs in the transmitter. Please note that the OA can be omitted if an integrated transmitter is used. The resulting optical spectrum is shown in Figure 6.5(b). The optical signal is coupled to >50 m single mode fibre (SMF) before being split into two paths via an optical splitter. Short length fibres are used to make the setup appropriate for indoor networks. One path (Path-1) is directly connected to an optical receiver (PD-1) and the other path (Path-2) has an OTDL and a cascaded optical receiver (PD-2). PD-1/2 are of the same type, and each one has a 15 and 20 GHz 3- and 6-dB

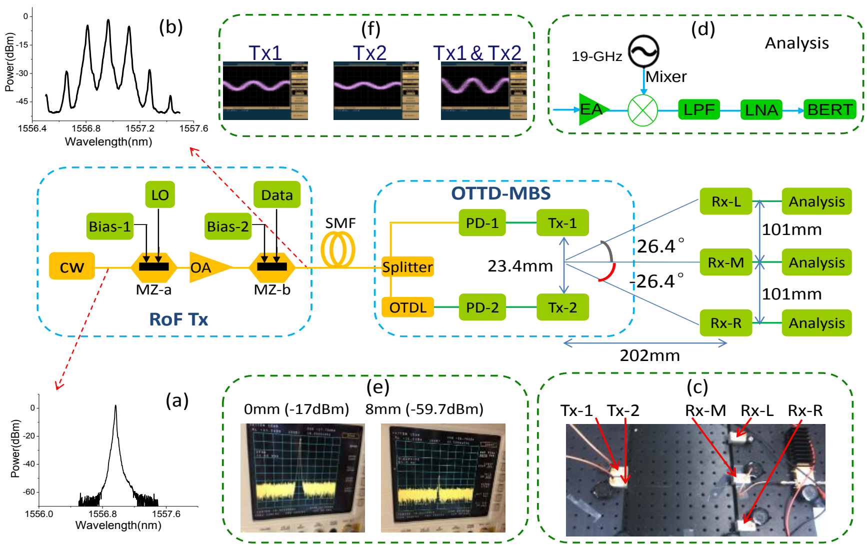

Figure 6.5 Experimental setup for proposed OTTD-RBS scheme in a RoF system.

bandwidth. The outputs of PD-1/2 are separately connected to two aperture antennas (Tx-1 and Tx-2 are separated by 23.4 mm) to transmit the data signals wirelessly. To receive the wireless signals, three aperture antennas, Rx-L/M/R, are used and located at a forward distance of 202 mm. The distance between the Rx antennas is 101 mm and therefore the receiving angle of Rx-L/R is $\pm 26.4\,°$ as shown in Figure 6.5. In a practical system, the antenna array and the optical tunable delay will be fixed at the ceiling center of a room. The microwave beam is then steered to the mobile user by tuning the optical tunable delay. Compact optical tunable delay schemes based on integrated photonic circuits can provide a solution for future practical applications. A photo of the antennas is shown in Figure 6.5(c). The received wireless signal is then analyzed to obtain the bit-error-ratio (BER) which is illustrated in the block 'analysis' in Figure 6.5(d). The signal is amplified by an electrical amplifier (EA), and then down converted by an electrical mixer and a 19 GHz local oscillator. After a 3 GHz low-pass filter and a low noise amplifier (LNA), the signal is retrieved for BER analysis.

The 4 Gb/s OFDM signal is generated from a Tektronix AWG 7122B at a sampling rate of 6 GSa/s. The size of the IFFT is 256 and the numbers of subcarriers used for data, pilots and high-frequency guard band (HFGB) are 192, 8, and 56, respectively. Note that the HFGB is used to suppress the out-of-band spectrum of the OFDM signal. Consequently, the spectrum occupation is 4 GHz for double sideband modulation. The subcarriers are arranged to satisfy the Hermitian symmetry for the real-valued IFFT output. The period of an OFDM symbol is 48 ns, and thus the symbol rate for each subcarrier is 20.83 MS/s. QPSK is employed for the data subcarrier modulation. The cyclic prefix is 1/8 of an OFDM period, which corresponds to 32 samples in every OFDM symbol. One training symbol is inserted in front of 160 data OFDM symbols for the symbol synchronization and channel estimation. The net bit rate of the OFDM signal is 3.975 Gb/s. The bit rate can go up to 8Gb/s within the same spectrum occupation if IQ modulation is employed. In the receiver, after synchronization, FFT operations are performed to demodulate and equalize the received signal using the channel response extracted from the training sequence and pilots. After de-mapping, the received data is retrieved for bit error ratio (BER) counting in an offline MATLAB program.

The simulated and measured received RF power curves for Rx-L/M/R, as a function of the delays are shown in Figure 6.6. The simulation is carried out using a phased array antenna design tool of MATLAB. Both the array factor and the pattern of the elements (aperture antennas) are taken into account. The measurements are carried out starting with OLD from 6 to 26 mm with a 2 mm step size. The maximum received powers of Rx-L/R are lower than the maximum power of Rx-M mainly due to the power non-uniformity of the

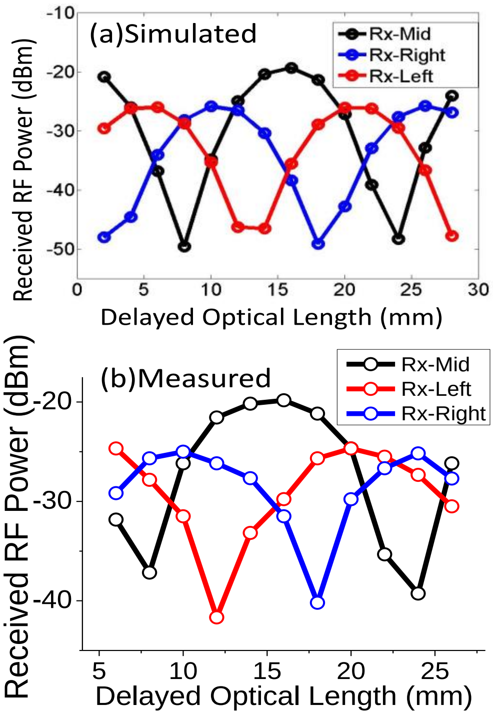

Figure 6.6 Power curves of Rx-L/M/R: (a) simulation, and (b) experiment.

aperture antennas. The power curves are periodic due to the periodicity of the phase shift as shown in Eq. (6.2). As expected, the power increases to a maximum when delays are close to an integer multiple of λ_{mm}. The peaks of Rx-L/R are symmetric around Rx-M's peak, due to the geometric symmetry. The measured results match with the simulated results very well. The contrast from peak to null is 19.4 and 29.3 dB for measured and simulated results

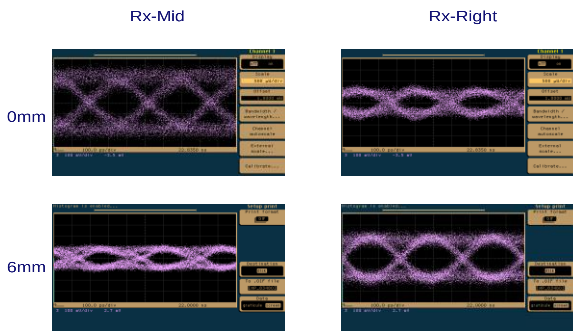

Figure 6.7 Eye diagrams of received OOK signal at Rx-M/R for 0 and 6 mm delays.

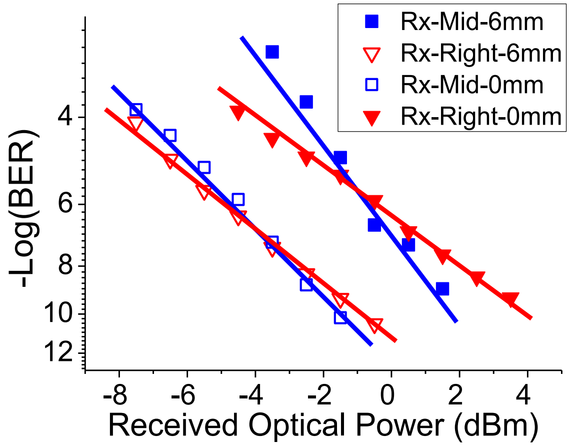

Figure 6.8 BER curves at Rx-M/R for 0 and 6 mm delays.

correspondingly. This is mainly due to the power imbalance between the Tx-1/2.

The broadband transmission of 1 Gb/s OOK signal with >2 GHz double sideband bandwidth based on the proposed OTTD-RBS setup is investigated. As shown in Figure 6.7, the eye diagrams at Rx-M/R are presented for both 0 and 6 mm delays. Shown in Figure 6.6(b), the microwave beam directs to Rx-M when delay is 0 mm, and the received power of Rx-R is >10 dB lower than that of Rx-M. Therefore the eye diagrams of Rx-M have larger openings than Rx-R's. When a 6 mm delay is applied, the microwave beam directs nearby Rx-R and away from Rx-M. The received power of Rx-M is >10 dB lower than Rx-R's. And thus the openings of Rx-R's eye diagrams are larger than Rx-M's. The BER curves are also measured for both cases as shown in Figure 6.8. The beam directing induced receiver sensitivity improvement at BER=10^{-10} is 3.8 dB for

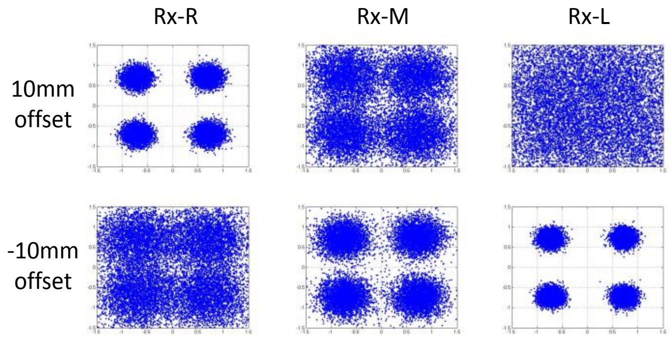

Figure 6.9 Constellations of the received OFDM signal at Rx-L/M/R for 10 mm and -10 mm delay.

Rx-M and 4.6 dB for Rx-R.

As shown in Figure 6.9, the constellations of the received 3.975 Gb/s OFDM signal at Rx-R/M/L are depicted for ±10 mm delays between Tx-1/-2. The negative delay is produced by moving the OTDL from Path-2 to Path-1. As shown in Figure 6.6(b), the microwave beam directs closely to Rx-R when the delay is 10 mm, and the received power of Rx-L is >8 dB lower than that of Rx-R. Therefore, the constellation of Rx-R converges better than the one of Rx-L. When the delay is moved to Path-1, and -10 mm delay is applied, the microwave beam directs nearby Rx-L caused by the geometric symmetry. The constellation of Rx-L is better than the one of Rx-R. Since the received power of Rx-M is in between Rx-L/R, its constellations convergence is therefore in the middle. The worst cases of received constellations at Rx-L/R are slightly different in terms of convergence. That is mainly due to the unequal received sensitivities of the two optical receivers.

The BER curves for Rx-M/R with ±10 mm delays are shown in Figure 6.10. The input power of the optical receivers is fixed at 1 dBm for all measurements. It can be seen that the beam-steering induced BER improvement at Rx-L/R is more than 4 orders of magnitude, which exhibits the significant spatial filtering effect. The spatial filtering feature of the PAAs depends on the number of antenna elements. Therefore, an improvement can be further obtained if more antenna elements are employed. The broadband transmission feature of OTTD is investigated by measuring the Welch power spectral density of the down converted received OFDM signals. The Welch power spectral density estimation can reduce the noise caused by the imperfect and finite signals. As shown in Figure 6.11, the OTTD-RBS does not introduce any notable frequency

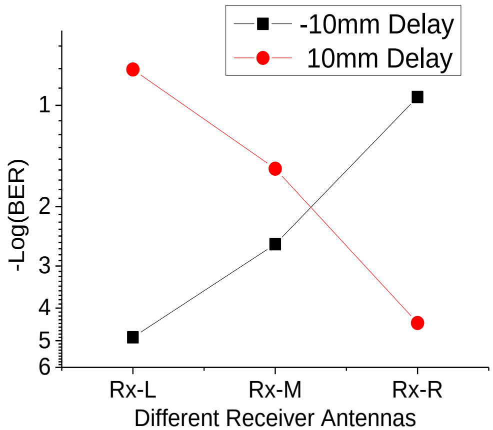

Figure 6.10 BER curves at Rx-M/R for ±10 mm delay.

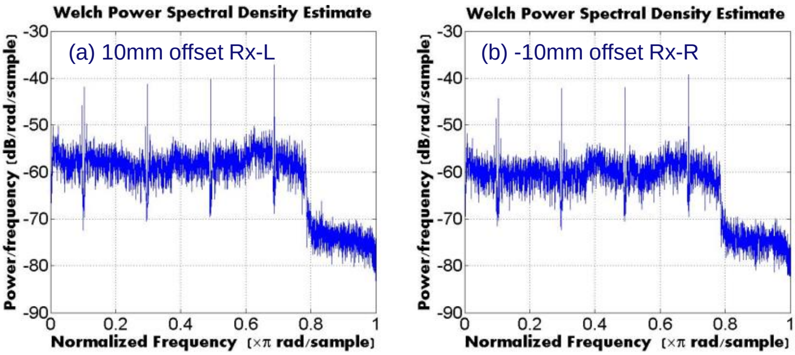

Figure 6.11 Welch power spectral density for the down converted OFDM of (a) Rx-L with 10 mm offset and (b) Rx-R with -10 mm offset.

fading to the received OFDM signal. Its feature of a flat transmission exhibits its capability for advanced modulation formats like OFDM.

6.2.3 Conclusion

A broadband optical true time delay for radio beam steering (OTTD-RBS) is proposed and experimentally demonstrated in an indoor radio-over-fibre network for the first time. For OOK signal, the beam directing induced receiver sensitivity improvement at BER=10^{-10} is 3.8 dB for Rx-M and 4.6 dB for Rx-R. 4.124-Gb/s wireless transmission is successfully demonstrated with 4 orders of magnitude bit error ratio improvement. Combining the spectrum efficiency of OFDM, the spatial filtering feature of OTTD-RBS, and the simple architecture to implement pico-cell networks, the proposed system can be an interesting solution for future broadband in-home networks.

6.3 40GHz ORBS-RoF system based on InP chip

Optical true-time-delay is widely used for broadband radio beam steering to avoid the beam squint problems [60, 62, 101-105]. Recently, RoF systems incorporating optical true-time-delay radio beam steering have been proposed for indoor networks [3-4]. However, current OTDLs based on bulk-optics components limit their further applications [106, 107]. Obviously an integrated solution is the key to future successful implementation. There are mainly two approaches to realize the integrated OTDLs, the first approach is based on physical length induced delay [62-64], and the second one is based on optical filtering induced group delay [65-69]. Generally, the first kind of integrated OTDLs are suitable for broadband applications with low angular resolution and the second kind matches the narrowband applications desiring higher angular resolutions (e.g. ground satellite communications).

In this section, the first beam-steered mm-wave RoF system based on a novel integrated tunable OTDL of the first kind is proposed and realized. It can find its applications in many fields such like indoor fibre-wireless networks, mm-wave communications and radar applications. Empowered by the novel OTDL chip, a series of advanced features are guaranteed. First, the antenna sites can be simplified with the remotely tunable OTDL chip. Second, the beam steering subsystem based on the integrated photonic circuit can be made compact with low power consumption and low cost compared with its discrete component counterpart. Third, the broadband (~60 GHz) wireless services can be transparently supported.

6.3.1 Brief introduction of the integrated InP SC-AWG-loop

The detailed operation principle of the engaged integrated InP SC-AWG-loop can be found in section 3.5. Here, only a brief introduction of its characterization is given.

The photo of fabricated integrated SC-AWG-loop is shown in Figure 6.12(a). Its fabrication done through Fraunhofer Heinrich Hertz Institute (FhG-HHI).

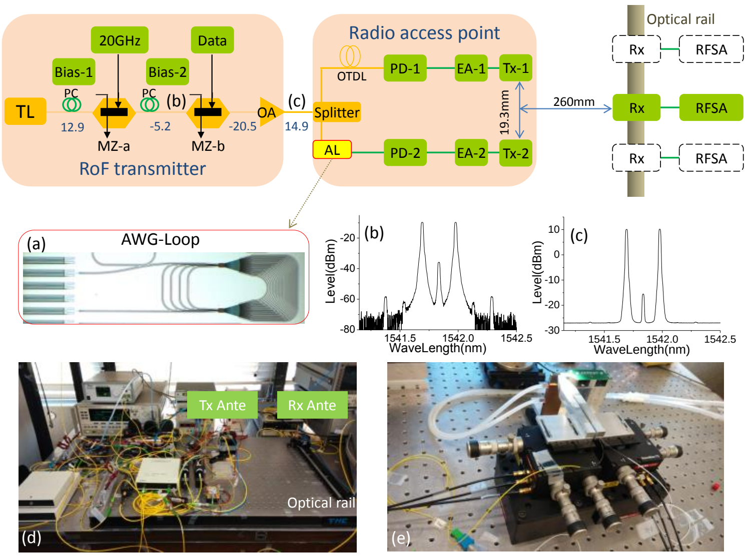

Figure 6.12 The experimental setup of 40 GHz radio beam steered RoF system, (a) the photo of the AWG-loop chip; (b)-(c) the measured optical spectrum; (d) the photo of the beam steered RoF system with antenna subsystem; (e) the photo of chip measurement subsystem.

The device is fabricated on a 3 inch InP wafer with 500 μm thickness (which will be thinned down to 250 μm after processing). There are three types of waveguides, which are: a low-index-contrast waveguide E200, a medium-index-contrast waveguide E600, and a high-index-contrast waveguide E1700. The E200 and E1700 are employed in our design. The E200 waveguide provides low loss which enables the low loss operation of the AWG free propagation region. E1700 waveguide provides the high density layout of the designs. The core component for the SC-AWG-loop is a spectral-cyclic 5-by-5 AWG. Its grating central wavelength λ_c is designed at 1550 nm and the grating order is designed to be 174. The free spectral range (FSR) is 8 nm (1000 GHz). The channel spacing (CS) is 1.6 nm (200 GHz). The waveguides connect four pairs of input and output to form the feedback loops with different delays. One pair of input and output of the AWG (In-0, Out-0) is used as the input and output of the AWG-loop and is connected to two spot size convertors (SSCs). The E1700 waveguides are used for all these connections. The maximum insertion loss of the SC-AWG-loop is 6.5 dB without SSC coupling loss. The footprint of the SC-AWG-loop is 2.6 mm by 1.2 mm. The maximum delay (Path-4) is designed to be 12.5 ps for π phase shift at 40 GHz. The designed delays of Path-1 to Path-4 are progressively increased from 0 ps to 12.5 ps. The measured delays are based on the time domain correlation method. The sampled signal travelled from Path-0 is used as a reference signal. The cross-correlation is performed between the other signals and the reference. As shown in Figure 6.13, the linear delays are exhibited for Path-1 to Path-4 with 12 ps delay, which is a little smaller than expected. The differences between the designed delays

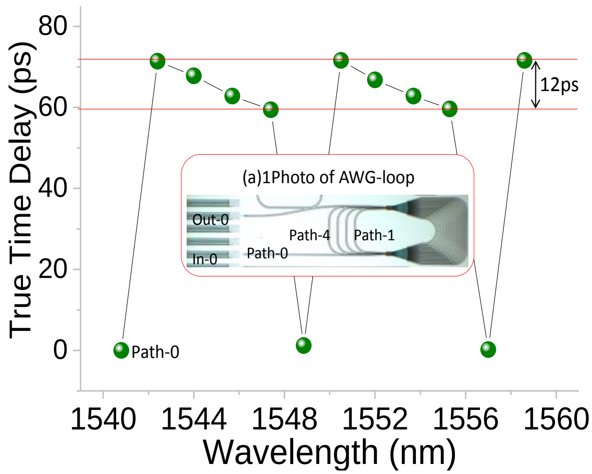

Figure 6.13 The measured delays of different delay channels of the AWG-loop.

and the measured ones for Path-1 to Path-4 are -0.5 ps, 0.1 ps, -0.76 ps and 0 ps from 1540 nm to 1548 nm. The delays of different wavelengths from Path-1 to Path-4 are 0.2 ps, -1 ps, 0 ps and 0.2 ps. The acceptable matches between the designed delays and measured ones demonstrate the high design accuracy.

6.3.2 Mm-wave beam steered radio over fibre system

The mm-wave beam steered RoF system is schematically shown in Figure 6.12. The data-carried optical mm-wave signal is generated in RoF transmitter and then delivered to the radio access point. The tuning of the optical carrier wavelength results the change of the differential delay between two photodiodes and finally make the mm-wave beam steering spatially.

The detailed experimental setup for proof-of-concept is described following. The 12.9 dBm optical carrier from a tunable laser passes to a MZM (MZ-a) via a PC. A 19 GHz clock signal is applied to the MZ-a biased at its null point for optical carrier suppression. In this way, the 38 GHz carrier frequency can be generated after optical-electrical conversion. The generated -5.2 dBm optical mm-wave is then modulated by the second MZM (MZ-b) after a PC. The 25 Msymbol/s QPSK signal at 500 MHz carrier frequency generated from a vector signal generator is applied on MZ-b. The -20.5 dBm resulted optical signal is then amplified to 14.9 dBm before 50 m single mode fibre delivery. The optical spectra after MZ-a and -b are shown respectively in Figure 6.12(b) and (c). The optical signal arrives in the radio access point and then it is split into two paths. One directly connects to a photodiode (PD-1) with a discrete tunable delay line to compensate the delay offset between two paths. The launched optical power of PD-1 is 8.7 dBm. The other passes through the integrated SC-AWG-loop by two cleaved single mode fibres for coupling. The photo of the fibre coupling system is shown in Figure 6.12(e). The output signal with 2.4 dBm power is amplified to 10.3 dBm and then launched into a photodiode (PD-2) for optical-electrical conversion. The converted signals are then amplified by two 40GHz band amplifier (EA-1 and EA-2). The outputs of EA-1/2 are separately connected to two identical 40 GHz aperture antennas (Tx-1 and Tx-2 are separated by 23.4 mm) to transmit the data signals wirelessly. To receive the wireless signals, a 40 GHz aperture antenna (Rx) is mounted on an optical rail. The Rx antenna can be moved along with an optical rail at a forward distance of 260 mm. The Rx antenna is directly connected to the radio frequency spectrum analyzer (RFSA). The center-to-center distance d between Tx-1/-2 is 1.93 cm. The measurement is carried out with different lateral distances moving along the optical rail. A photo of the whole RoF system including the antennas is shown in Figure 6.12(d). The received 38 GHz signal is then analyzed by the

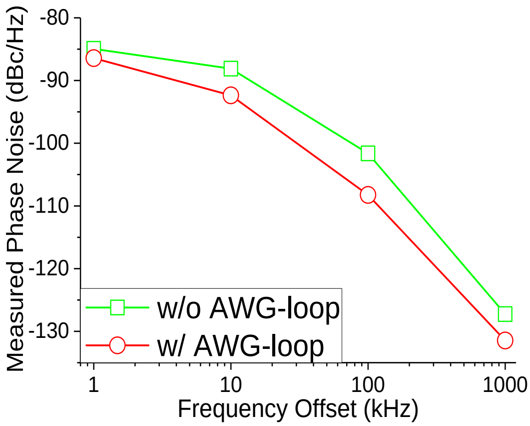

Figure 6.14 The measured phase noise delays of different delay channels of the AWG-loop.

RFSA to obtain the received power, phase noise and error vector magnitude of the QPSK signal.

6.3.3 Experimental results and discussion

The measured phase noise of the 38 GHz carrier frequency is shown in Figure 6.14. It indicates that the phase noise performance can be improved if the optical signal goes through the integrated SC-AWG-loop). This is mainly because the out-of-band noise is partially filtered due to the passband effect of the AWG.

The received power of the 38 GHz signal along the optical rail is measured as shown in Figure 6.15 to obtain the mm-wave beam profile and to observe the mm-wave beam steering. The center of two transmitter antennas (Tx-1/-2) and the origin of the optical rail are aligned. The measured received power versus the offset of the optical rail origin (referred as ‘X-axis offset’) is shown in Figure 6.15 with its simulation counterpart. The simulation is performed based on the basic expression of the array factor shown below:

$$AF(\theta) = \sum_{n=1}^{N} I_n \exp(-j\beta n d \sin\theta) \qquad (6.3)$$

The assumption behind Eq. (6.3) is that the forward distance is much longer than the element antenna distance *d*, which results the same arrival angle (θ) for Tx-1 and Tx-2. The additional phase compensation is added since the forward distance from the transmitter antennas (Tx-1/-2) is not that long. The engaged aperture antennas can be considered as semi-omni-directional antennas. Its far-field pattern covers the whole hemisphere with a small deviation. Thus the far-

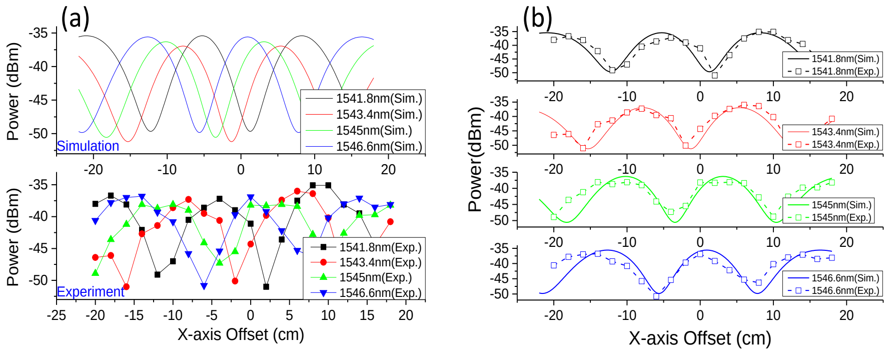

Figure 6.15 The received power versus x-axis offset for simulation and experiment, (a) the seperated figures for the simulated and the experimental results; (b) the one-by-one comparison between the simulated results and experimental ones for each delay.

field pattern of the aperture antennas is not taken into account in our simulation. In the simulation, the amplitude coefficients of the two antennas are set to 1 and 0.675 corresponding to the optical power launched to the photodiodes. The phase coefficients of the two antennas for the simulation are deduced from the measured delays of the integrated SC-AWG-loop. The peak of the simulated power curve is then normalized to the peak of the experimental results for all cases.

Figure 6.15(a) and (b) are based on the same data but with different presentations for illustration convenience. As shown in Figure 6.15(b), the simulated and experimental results are depicted one by one for all four wavelengths (delays). It can be seen clearly that the experimental results match well with the simulated ones in terms of peak/null locations and their periodicities. The difference between two results may be introduced by the inevitable mm-wave reflection in the real environment.

In Figure 6.15(a), the simulated and experimental results are separated to allow better illustration of the trends. The different wavelengths can select different paths (delays) of the integrated SC-AWG-loop, which results in different beam directions. As the wavelength increases from 1541.8 nm to 1546.6 nm, the delay decreases from 12 ps to 0 ps, which causes the beam peaks to move from the left side to the right side. There are more than one peak shown in the beam profiles for all delay (wavelength) cases. For phased array antennas, it is well known that the side lobes can be suppressed if the element antenna distance d is smaller than half of mm-wave wavelength (λ_{mm}). In our experiment, due to the bulk aperture antennas, the distance d is 1.93 cm much larger than the half of λ_{mm} (0.39 cm), thus the side lobes exist resulting more

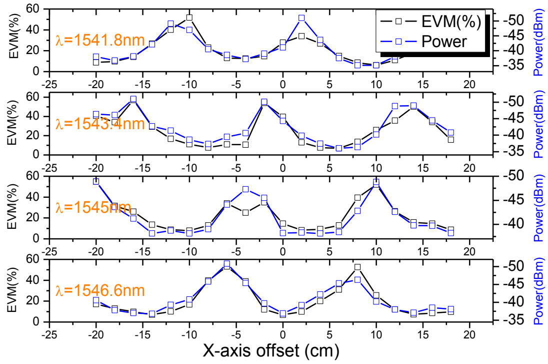

Figure 6.16 The measured error vector magnitude and power versus x-axis offset for the received 38 GHz signal.

than one peaks of the beam profiles. The power suppression ratios for all delays are more than 14 dB. This can be further improved if the power balance of PD-1/-2 can be conserved. The simulation well predicts such unbalance as shown in Figure 6.15(a). The experimental results show that the beam peaks of different delays are with slight differences. This may be due to the mechanism twist induced connection loosening. During the experiment, a coaxial cable connects the receiver antennas and the RFSA, whose loss is sensitive to the movement around the optical rail. After some movements, the connection loosens, resulting in the increased loss.

The error vector magnitude (EVM) of the 25 MS/s QPSK signal on the 38 GHz mm-wave is measured as shown in Figure 6.16 with the corresponding received power. Two curves are normalized to allow better visualization. The corresponding constellations are shown in Figure 6.17. The EVM curves agree

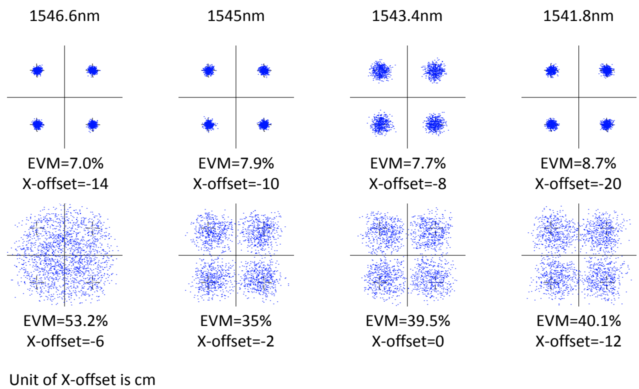

Figure 6.17 The measured constellations for received QPSK signal on 38 GHz carrier frequency.

well with the power curves, indicating that the beam steering induced power enhance improves the quality of the received QPSK signal. When the mm-wave beams direct to the receive antennas, the EVMs can be smaller than 9%, and the constellations are well converged as shown in the first line of Figure 6.17. For the nulls, the received power is reduced for 14 dB. Such low received power even cannot allow the demodulation of the QPSK signal. As shown in Figure 6.17, the constellation of the 1546.6 nm case with -6 cm x-axis offset demonstrates an unsuccessful demodulation of QPSK signal. The signal EVM can be reduced from around 40% to around 7%, indicating around 6 times quality enhancement. It also means that the power leaked to the other spatial channels can be significantly reduced to allow spatial filtering. The spatial filtering can relieve the heavy task of digital signal processing.

6.3.4 Conclusion

The 40 GHz millimeter-wave beam steering via a novel SC-AWG-loop is demonstrated in an indoor RoF system. Empowered by such novel integrated device, the 38 GHz mm-wave beam-steered RoF system is demonstrated for indoor applications. The beam steering induced 14dBm power improvement is observed with resulting in 6 times EVM performance enhancement. Its spatial filtering to reduce the power leakage is also discussed. Featured by the integrated OTDL, the proposed system exhibits its advantages as remote-tuning, compactness, and broadband service support.

6.4 Summary

Integrating mm-wave radio beam steering into the radio over fibre (RoF) system can provide a high capacity and energy efficient indoor fibre-wireless network. The 19 GHz optical radio beam-steered radio-over-fibre (ORBS-RoF) is proposed and investigated with aspects of RoF subsystem, optical true time delay subsystem and phased antenna array subsystem. Further, the 38 GHz ORBS-RoF system based on an integrated SC-AWG-loop is experimentally investigated. The beam steering induced 14 dBm power improvement is observed with resulting in 6 times EVM performance enhancement. Featured by the integrated OTDL, the proposed system exhibits its advantages as remote-tuning, compactness, and broadband service support.

Chapter 7 Conclusions and Suggestions for Future Work

7.1 Conclusions

The research reported in this thesis was done in the Dutch project Smart Optical Wireless Indoor Communication Infrastructure (SOWICI), which was part of the Smart Energy Systems program funded by the Dutch Organization for Scientific Research (NWO). The data volumes transported in indoor networks are growing fast. In particular for wireless connectivity, the data volumes may exceed those on the home access line, due to heavy home-internal traffic. SOWICI's goal is to conceive a novel indoor broadband communication infrastructure which provides communication services in the most reliable, cost-effective and energy-efficient way. To this end, this thesis describes a series of research activities ranging from research roadmap to concrete research activities, encompassing elementary circuit techniques to system integrations.

Inspired by the SOWICI proposal and Ref. [11], indoor fibre-wireless networks (IFiWiNs) are considered as a very powerful solution for the voracious bandwidth demand of indoor terminal users. As we discussed in Chapter 1, the these concerns for IFiWiNs are a versatile and efficient gateway to deal with all network functions, and the support for future services and service convergence. The research roadmap of this thesis is to fulfill the two mentioned requirements gradually. As a starting point, in Chapter 2, the gateway functions and architecture design of indoor fibre-wireless networks (IFiWiNs) are addressed in order to well address all network functions. As a core technique, optical radio beam steering techniques based on tunable optical true time delay were studied in Chapter 3, in operation principle level and at integrated implementation level as well. To efficiently steer radio beams, localization of radio devices is required. Two novel parallel optical phase detector schemes for radio devices localization were investigated in Chapter 4. To deliver control signals for routing and beam steering, a simple control channel is demanded in IFiWiNs. In Chapter 5, we studied two simple control signal delivery schemes for baseband data from optical access networks and for IF/RF data inside IFiWiNs. In Chapter 6, optical radio beam steered radio over fibre systems (ORBS-RoF) were experimentally investigated. The detailed technical conclusions are presented below.

Gateway function design

To efficiently deal with signals delivered, three main functions of IFiWiN gateways were described in Section 2.2, namely flexible-reach data delivery, convenient frequency up-conversion, and versatile indoor exchange functions. Three IFiWiN gateways were designed for three different application scenarios. A simplified remote up-conversion (RUC) scheme for the low residential density IFiWiNs was investigated in Section 2.3. A simple 60 GHz remote up-conversion scheme with electrical tones injection was proposed and experimentally demonstrated for low density IFiWiN. The proposed RUC scheme uses only one intensity modulator. Such scheme can provide both wired and wireless service without any additional device. Experimental results show that 2.5 Gb/s wired service in baseband and 2.5 Gb/s wireless service at 60 GHz were successfully delivered over 50 km SMF with a power penalty less than 0.3 dB. In section 2.4, the gateway for versatile indoor exchange functions with flexible-reach was studied. By sharing one SOA for up-conversion and wavelength conversion (for routing), a novel gateway for remote up-conversion and indoor exchange functions was proposed and experimentally demonstrated. A 5 Gb/s data signal carried by a 60 GHz mm-wave RoF channel was successfully delivered over 102 km SMF-28 with a power penalty less than 1.1 dB for both single channel (routing) and multiple-channels (multi-casting). Optical routing and multi-casting of 5 Gb/s data carried on a 60 GHz optical mm-wave have been demonstrated as well. In section 2.5, a gateway of ultra-broadband data delivery for dense indoor networks was proposed. Employing optical heterodyne (OH) and polarization multiplexing (PolMux) technique, a simple gateway was designed for flexible RF carrier frequency generation with two spatial channels for MIMO signals. Moreover, routing can be achieved by wavelength tuning. A 61.3 Gb/s MIMO-OFDM signal over 1 km SMF-28 fibre and 1 m wireless link at 40 GHz was delivered with a BER at the outer FEC threshold (less than $3.8\text{x}10^{-3}$) at -22 dB OSNR.

The three proposed schemes for different application scenarios all used simplified configurations compared with previous reported works. They were all verified experimentally with good performances.

Optical true time delay techniques for radio beam steering

The optical radio beam steering was explored in two-fold. At the operation principle level, a new optical true time delay concept named cyclic additional optical true time delay (CAO-TTD) was proposed and studied for flexible 1D beam steering and spectral filtering in Section 3.2. About 13dB spatial and spectral power suppression was achieved, which can be further improved by improving the power balance of the two transmitter antennas. At the implementation level, two compact, fabrication-tolerant photonic integrated circuit designs based on a SC-AWG-loop concept were realized and characterized. In Section 3.3, the first design based on a SOI platform was realized and measured. A linear phase shift across a 20 GHz spectral width for different wavelengths was obtained. The measured results show that the delay errors were less than 6.7% for a broad 23-nm operation spectrum. In Section 3.4, the second design was fabricated on a Indium Phosphide (InP) platform. The experimental results show less than 6.5 dB insertion loss of the integrated SC-AWG-loop excluding fiber-chip coupling loss. Five different delays from 0 ps to 71.6 ps by 8nm wavelength tuning were generated with less than 0.67 ps delay errors. A 2D version of this design is also fabricated and the measurement is not finished yet.

Both fabricated chips demonstrated that the AWG-loop design concept is a powerful and attractive solution in terms of compactness and delay/phase errors.

Radio devices localization based on optical approaches

Optical localization of radio devices was studied in Chapter 4 as an auxiliary function for radio beam steering. An optical approach can provide many advances such as ultra-low loss and huge bandwidth, which allows high accuracy, and immunity to electromagnetic interferences. Apart from previously reported serial optical delay detector, the novel parallel optical delay detector (PODD) schemes were proposed and investigated for angle-of-arrival measurement. A major advantage of such scheme is that the measurement accuracy can be monitored. Experimental results show that the measurement errors are less than 8.59° within the range from 0° to 160°. In Section 4.2, a PODD based on a parallel MZM was proposed. In Section 4.3, a phase modulation parallel optical delay detector for microwave angle-of-arrival measurement with accuracy monitoring was proposed using only one dual-electrode MZM. Phase shifts from 5° to 165° were measured with 3.1° measurement error.

With the capability of accuracy monitoring, and the robust parallel and simple structure, the two proposed schemes can be attractive solutions for optical angle-of-arrival measurements. The phase modulation PODD exhibited a better performance than the intensity modulation PODD in terms of complexity and measure accuracy.

Control channel

As discussed in Chapter 5, control signaling is important for realizing the dynamic network function and it only occupies limited bandwidth. For optical access networks, the gateway is considered as a remote node to pick up data from home access passive optical networks (PONs). The control signaling needs to be done in the gateway. It should be avoided to process the high speed baseband data (>10Gb/s). For the IF and RF signals, the control signaling delivery may come from the home control center and remote access nodes in each room for network functions. The challenge is to efficiently obtain the low speed control signaling from the mm-wave frequency carrier. In Chapter 5, the control signaling delivery for PON data is investigated in Section 5.1. A simple signaling insertion and detection scheme for a reconfigurable WDM-OFDM optical access networks was proposed. The signaling is synchronously inserted into OOFDM signals without any extra optical wavelength or high-speed logical operation. The experimental results show that, with 100km transmission, the OOK signaling data adds only 1.5 dB power penalty, demonstrating that this signaling insertion and detection scheme is well feasible. Furthermore, a solution for the IF/RF signal is studied in Section 5.2. A signaling insertion and detection scheme based on digital frequency multiplexing and pulse shaping for 12.7 Gb/s throughput in 60 GHz indoor fibre-wireless networks was demonstrated. The power penalty of signaling insertion was less than 0.8 dB.

Based on the achieved results, it was proved that the proposed schemes can provide reliable and low-cost signaling delivery channels for both baseband PON data and for 60 GHz indoor fibre-wireless network.

System demonstration

In Chapter 6, radio beam steered radio over fiber systems are demonstrated with bulk optical true time delay lines and integrated optical tunable delay lines. In Section 6.2, a broadband optical true time delay for radio beam steering (OTTD-RBS) was proposed and experimentally demonstrated in an indoor radio-over-fibre network for the first time. For OOK signal, the beam directing induced receiver sensitivity improvement at BER=10^{-10} was 3.8 dB for the receiver antenna in the middle and 4.6 dB for the receiver antenna on the right side. For the OFDM signal, 4.124-Gb/s wireless transmission was successfully demonstrated with 4 orders of magnitude bit error ratio improvement. In Section 6.3, 40 GHz millimeter-wave beam steering via a novel SC-AWG-loop was demonstrated in an indoor RoF system. Empowered by such novel integrated device, a 38 GHz mm-wave beam-steered RoF system was demonstrated for indoor applications. A beam steering induced 14dBm power improvement was observed resulting in 6 times EVM performance enhancement.

Both experiments exhibit the spatial filtering feature to improve receiver sensitivity and to reduce the wireless power leakage. Employing the integrated OTDL, the second system exhibits additional advantages such as remote-tuning, compactness, and broadband service support.

As one of three major implementers, I am proud for the insights gained from the SOWICI project. When I come back to its proposal written four years ago, the vision of future wireless services and the description of the challenges of indoor networks match exactly what people are currently talking about. Nowadays, people start to discuss the shape of 5G cellular services, and one of the most challenging parts is the 5G cellular coverage handicap of dense areas like indoor environments. This point is well addressed in SOWICI proposal and has now resulted in a concrete technology roadmap. We believe that the research results of SOWICI may provide a bundle of lavish solutions for the successful implementation of 5G cellular networks in indoor scenarios, which put very challenging demands and require dynamic picocell techniques (such as radio beam steering). I trust that the work described in this thesis, on basis of SOWICI proposal, can to some extent provide useful research results for future indoor fibre-wireless networks.

7.2 Future work

The SOWICI project opens a door for a series of fruitful research activities. Some have been done during my four years Ph.D and there are still some very interesting research topics as listed below:

1. A novel energy-efficient IFiWiN gateway design at the photonic integration level. The photonic integrated circuit can provide a much more flexible design of IFiWiN gateway different from bulk devices based version.

2. An implementation of two dimension integrated optical radio beam steering system.

3. Much of the saving of energy comes from an intelligent control and management function, which can be integrated in a dynamic bandwidth allocation scheme for pico- or femto-cells. Also ad-hoc solutions for coping with sudden upsurge of traffic demands should be studied in more detail for smart indoor communication networks.

4. Further work on integrated 2D OTTD structure, scaling up to high port counts and monolithic integration with photodiodes and antennas.

References

[1] Q. C. Li, N. Huaning, A. T. Papathanassiou, and W. Geng, "5G Network Capacity: Key Elements and Technologies," *Vehicular Technology Magazine, IEEE,* vol. 9, pp. 71-78, 2014.

[2] Cisco, "Cisco Visual Networking Index: Forecast and Methodology, 2013–2018 " *Available at http://www.cisco.com/c/en/us/solutions /collateral/service-provider/visual-networking-index-vni/white_paper_c11-520862.html*, 2014.

[3] T. S. Rappaport, F. Gutierrez, E. Ben-Dor, J. N. Murdock, Q. Yijun, and J. I. Tamir, "Broadband Millimeter-Wave Propagation Measurements and Models Using Adaptive-Beam Antennas for Outdoor Urban Cellular Communications," *Antennas and Propagation, IEEE Transactions on,* vol. 61, pp. 1850-1859, 2013.

[4] W. Roh, S. Ji-Yun, P. Jeongho, L. Byunghwan, L. Jaekon, K. Yungsoo, *et al.*, "Millimeter-wave beamforming as an enabling technology for 5G cellular communications: theoretical feasibility and prototype results," *Communications Magazine, IEEE,* vol. 52, pp. 106-113, 2014.

[5] A. M. J. Koonen, M. Popov, and H. Wessing, "Upper bound for energy efficiency in multi-cell fibre-wireless access systems," in *Optical Communication (ECOC 2013), 39th European Conference and Exhibition on*, 2013, pp. 1-3.

[6] V. Jungnickel, K. Manolakis, W. Zirwas, B. Panzner, V. Braun, M. Lossow*, et al.*, "The role of small cells, coordinated multipoint, and massive MIMO in 5G," *Communications Magazine, IEEE,* vol. 52, pp. 44-51, 2014.

[7] E. Larsson, O. Edfors, F. Tufvesson, and T. Marzetta, "Massive MIMO for next generation wireless systems," *Communications Magazine, IEEE,* vol. 52, pp. 186-195, 2014.

[8] T. S. Rappaport, S. Shu, R. Mayzus, Z. Hang, Y. Azar, K. Wang*, et al.*, "Millimeter Wave Mobile Communications for 5G Cellular: It Will Work!," *Access, IEEE,* vol. 1, pp. 335-349, 2013.

[9] C. H. Doan, S. Emami, A. M. Niknejad, and R. W. Brodersen, "Millimeter-wave CMOS design," *Solid-State Circuits, IEEE Journal of*, vol. 40, pp. 144-155, 2005.
[10] M. Dohler, "5G Ultra-High Capacity Network Design with rates 10x LTE-A," *https://www.youtube.com/watch?v=y764VAyJn84*, 2012.
[11] A. M. J. Koonen and E. Tangdiongga, "Photonic Home Area Networks," *Lightwave Technology, Journal of,* vol. 32, pp. 591-604, 2014.
[12] D. Wake, A. Nkansah, and N. J. Gomes, "Radio Over Fiber Link Design for Next Generation Wireless Systems," *Lightwave Technology, Journal of*, vol. 28, pp. 2456-2464, 2010.
[13] A. M. J. Koonen and L. M. Garcia, "Radio-Over-MMF Technique Part II: Microwave to Millimeter-Wave Systems," *Lightwave Technology, Journal of*, vol. 26, pp. 2396-2408, 2008.
[14] C. Gee-Kung, Y. Jianjun, and J. Zhensheng, "Architectures and Enabling Technologies for Super-Broadband Radio-over-Fiber Optical-Wireless Access Networks," in *Microwave Photonics, 2007 IEEE International Topical Meeting on*, 2007, pp. 24-28.
[15] Z. Cao, J. Yu, L. Chen, and Q. Shu, "Reversely Modulated Optical Single Sideband Scheme and Its Application in a 60-GHz Full Duplex ROF System," *Photonics Technology Letters, IEEE,* vol. 24, pp. 827-829, 2012.
[16] Z. Cao, J. Yu, M. Xia, Q. Tang, Y. Gao, W. Wang, *et al.*, "Reduction of Intersubcarrier Interference and Frequency-Selective Fading in OFDM-ROF Systems," *Lightwave Technology, Journal of,* vol. 28, pp. 2423-2429, 2010.
[17] Z. Cao, H. P. A. van den Boom, C. M. Okonkwo, E. Tangdiongga, and A. M. J. Koonen, "Simultaneous provision of wired service and dispersion-robust 60GHz wireless service in radio-over-fiber system based on remote up conversion with electrical tones injection," *Optics Communications*, vol. 311, pp. 346-349, 2013.
[18] Z. Cao, J. Yu, H. Zhou, W. Wang, M. Xia, J. Wang, *et al.*, "WDM-RoF-PON Architecture for Flexible Wireless and Wire-Line Layout," *Optical Communications and Networking, IEEE/OSA Journal of,* vol. 2, pp. 117-121, 2010.
[19] Z. Cao, H. P. A. van den Boom, E. Tangdiongga, K. Chandra, and A. M. J. Koonen, "Long Reach Hybrid Fiber-Wireless System With Remote Up-Conversion and Local Exchange," *Photonics Technology Letters, IEEE*, vol. 25, pp. 737-740, 2013.
[20] J. J. Vegas Olmos, T. Kuri, T. Sono, K. Tamura, H. Toda, and K. i. Kitayama, "Reconfigurable 2.5-Gb/s Baseband and 60-GHz (155-Mb/s)

Millimeter-Waveband Radio-Over-Fiber (Interleaving) Access Network," *Lightwave Technology, Journal of,* vol. 26, pp. 2506-2512, 2008.

[21] L. Chun-Ting, S. Po-Tsung, J. J. Chen, X. Wen-Qiang, P. Peng-Chun, and C. Sien, "Optical Millimeter-Wave Signal Generation Using Frequency Quadrupling Technique and No Optical Filtering," *Photonics Technology Letters, IEEE,* vol. 20, pp. 1027-1029, 2008.

[22] C. Lim, A. Nirmalathas, M. Bakaul, P. Gamage, L. Ka-Lun, Y. Yizhuo, *et al.*, "Fiber-Wireless Networks and Subsystem Technologies," *Lightwave Technology, Journal of,* vol. 28, pp. 390-405, 2010.

[23] L. Fan, C. Zizheng, L. Xinying, D. Ze, and C. Lin, "Fiber-Wireless Transmission System of PDM-MIMO-OFDM at 100 GHz Frequency," *Lightwave Technology, Journal of,* vol. 31, pp. 2394-2399, 2013.

[24] D. Wake, A. Nkansah, N. J. Gomes, G. de Valicourt, R. Brenot, M. Violas, *et al.*, "A Comparison of Radio Over Fiber Link Types for the Support of Wideband Radio Channels," *Journal of Lightwave Technology,* vol. 28, pp. 2416-2422, 2010/08/15 2010.

[25] D. Wake, A. Nkansah, N. J. Gomes, C. Lethien, C. Sion, and J.-P. Vilcot, "Optically Powered Remote Units for Radio-Over-Fiber Systems," *Journal of Lightwave Technology,* vol. 26, pp. 2484-2491, 2008/08/01 2008.

[26] N. Gomes, A. Nkansah, and D. Wake, "Radio-Over-MMF Techniques?Part I: RF to Microwave Frequency Systems," *Journal of Lightwave Technology,* vol. 26, pp. 2388-2395, 2008/08/01 2008.

[27] J. Capmany, B. Ortega, A. Martinez, D. Pastor, M. Popov, and P. Y. Fonjallaz, "Multiwavelength single sideband modulation for WDM radio-over-fiber systems using a fiber grating array tandem device," *Photonics Technology Letters, IEEE,* vol. 17, pp. 471-473, 2005.

[28] A. Nirmalathas, P. A. Gamage, C. Lim, D. Novak, and R. Waterhouse, "Digitized Radio-Over-Fiber Technologies for Converged Optical Wireless Access Network," *Lightwave Technology, Journal of,* vol. 28, pp. 2366-2375, 2010.

[29] J. J. Vegas Olmos, T. Kuri, and K. Kitayama, "Reconfigurable Radio-Over-Fiber Networks: Multiple-Access Functionality Directly Over the Optical Layer," *Microwave Theory and Techniques, IEEE Transactions on,* vol. 58, pp. 3001-3010, 2010.

[30] S. Po-Tsung, J. Chen, L. Chun-Ting, J. Wen-Jr, H. Han-Sheng, P. Peng-Chun, *et al.*, "Optical Millimeter-Wave Signal Generation Via Frequency 12-Tupling," *Lightwave Technology, Journal of,* vol. 28, pp. 71-78, 2010.

[31] C. W. Chow, C. H. Yeh, C. H. Wang, C. L. Wu, S. Chi, and L. Chinlon, "Studies of OFDM signal for broadband optical access networks," *Selected Areas in Communications, IEEE Journal on,* vol. 28, pp. 800-807, 2010.

[32] A. Chowdhury, C. Hung-Chang, H. Yu-Ting, and C. Gee-Kung, "Advanced System Technologies and Field Demonstration for In-Building Optical-Wireless Network With Integrated Broadband Services," *Lightwave Technology, Journal of,* vol. 27, pp. 1920-1927, 2009.

[33] J. J. Vegas Olmos, T. Kuri, T. Sono, K. Tamura, H. Toda, and K. I. Kitayama, "Wireless and Optical-Integrated Access Network With Peer-To-Peer Connection Capability," *Photonics Technology Letters, IEEE,* vol. 20, pp. 1127-1129, 2008.

[34] F. Shu-Hao, L. Cheng, and C. Gee-Kung, "Heterodyne Optical Carrier Suppression for Millimeter-Wave-over-Fiber Systems," *Lightwave Technology, Journal of*, vol. 31, pp. 3210-3216, 2013.

[35] C. W. Chow, C. H. Yeh, S. M. G. Lo, C. Li, and H. K. Tsang, "Long-reach radio-over-fiber signal distribution using single-sideband signal generated by a silicon-modulator," *Opt. Express,* vol. 19, pp. 11312-11317, 2011.

[36] T. Kuri, H. Toda, J. J. V. Olmos, and K. Kitayama, "Reconfigurable Dense Wavelength-Division-Multiplexing Millimeter-Waveband Radio-Over-Fiber Access System Technologies," *Lightwave Technology, Journal of*, vol. 28, pp. 2247-2257, 2010.

[37] C. Gee-Kung, A. Chowdhury, J. Zhensheng, C. Hung-Chang, H. Ming-Fang, Y. Jianjun, *et al.*, "Key Technologies of WDM-PON for Future Converged Optical Broadband Access Networks [Invited]," *Optical Communications and Networking, IEEE/OSA Journal of,* vol. 1, pp. C35-C50, 2009.

[38] J. J. Vegas Olmos, T. Kuri, and K. Kitayama, "Dynamic Reconfigurable WDM 60-GHz Millimeter-Waveband Radio-Over-Fiber Access Network: Architectural Considerations and Experiment," *Lightwave Technology, Journal of*, vol. 25, pp. 3374-3380, 2007.

[39] Z. Cao, J. Yu, F. Li, L. Chen, Q. Shu, Q. Tang, *et al.*, "Energy Efficient and Transparent Platform for Optical Wireless Networks Based on Reverse Modulation," *IEEE Journal On Selected Areas In Communications*, vol. 31, 2013.

[40] C. Zizheng, Y. Jianjun, C. Lin, and S. Qinglong, "Reversely Modulated Optical Single Sideband Scheme and Its Application in a 60-GHz Full Duplex ROF System," *Photonics Technology Letters, IEEE,* vol. 24, pp. 827-829, 2012.

[41] Z. Cao, J. Yu, F. Li, L. Chen, Q. Shu, Q. Tang, *et al.*, "Energy Efficient and Transparent Platform for Optical Wireless Networks Based on Reverse Modulation," *Selected Areas in Communications, IEEE Journal on,* vol. 31, pp. 804-814, 2013.

[42] Y. Jianjun, C. Gee-Kung, J. Zhensheng, A. Chowdhury, H. Ming-Fang, C. Hung-Chang, *et al.*, "Cost-Effective Optical Millimeter Technologies and Field Demonstrations for Very High Throughput Wireless-Over-Fiber Access Systems," *Lightwave Technology, Journal of,* vol. 28, pp. 2376-2397, 2010.

[43] M. Jianxin, J. Yu, Y. Chongxiu, X. Xiangjun, Z. Junying, and L. Chen, "Fiber Dispersion Influence on Transmission of the Optical Millimeter-Waves Generated Using LN-MZM Intensity Modulation," *Lightwave Technology, Journal of,* vol. 25, pp. 3244-3256, 2007.

[44] C. Zizheng, Y. Jianjun, L. Fan, C. Long, S. Qinglong, T. Qi, *et al.*, "Energy Efficient and Transparent Platform for Optical Wireless Networks Based on Reverse Modulation," *Selected Areas in Communications, IEEE Journal on,* vol. 31, pp. 804-814, 2013.

[45] Y. K. Seo, J. H. Seo, and W. Y. Choi, "Photonic frequency-upconversion efficiencies in semiconductor optical amplifiers," *Photonics Technology Letters, IEEE,* vol. 15, pp. 751-753, 2003.

[46] F. Aurzada, M. Scheutzow, M. Reisslein, N. Ghazisaidi, and M. Maier, "Capacity and Delay Analysis of Next-Generation Passive Optical Networks (NG-PONs)," *Communications, IEEE Transactions on,* vol. 59, pp. 1378-1388, 2011.

[47] P. J. Urban, A. M. J. Koonen, G. D. Khoe, and H. de Waardt, "Interferometric Crosstalk Reduction in an RSOA-Based WDM Passive Optical Network," *Lightwave Technology, Journal of,* vol. 27, pp. 4943-4953, 2009.

[48] M. J. Fice, A. Chiuchiarelli, E. Ciaramella, and A. J. Seeds, "Homodyne Coherent Optical Receiver Using an Optical Injection Phase-Lock Loop," *Lightwave Technology, Journal of,* vol. 29, pp. 1152-1164, 2011.

[49] L. A. Johansson and A. J. Seeds, "Generation and transmission of millimeter-wave data-modulated optical signals using an optical injection phase-lock loop," *Lightwave Technology, Journal of,* vol. 21, pp. 511-520, 2003.

[50] X. Li, J. Yu, Z. Dong, Z. Cao, N. Chi, J. Zhang, *et al.*, "Seamless integration of 57.2-Gb/s signal wireline transmission and 100-GHz wireless delivery," *Opt. Express,* vol. 20, pp. 24364-24369, 2012.

[51] L. Deng, M. Beltran, P. Xiaodan, Z. Xu, V. Arlunno, Z. Ying, *et al.*, "Fiber Wireless Transmission of 8.3-Gb/s/ch QPSK-OFDM Signals in

75–110-GHz Band," *Photonics Technology Letters, IEEE,* vol. 24, pp. 383-385, 2012.

[52] F. Li, Z. Cao, X. Li, Z. Dong, and L. Chen, "Fiber-Wireless Transmission System of PDM-MIMO-OFDM at 100 GHz Frequency," *Journal of Lightwave Technology,* vol. 31, pp. 2394-2399, 2013/07/15 2013.

[53] Z. Cao, F. Li, C. M. Okonkwo, H. P. A. van den Boom, M. Chen, B. Yang, *et al.*, "Synchronized signaling delivery for broadband 60 GHz in-building optical wireless network based on digital frequency division multiplexing and digital Nyquist shaping," *Optics Express,* vol. 21, pp. 270-275, 2013/01/14 2013.

[54] Z. Cao, F. Li, C. M. Okonkwo, H. P. A. van den Boom, E. Tangdiongga, Q. Tang, *et al.*, "A Synchronized Signaling Insertion and Detection Scheme for Reconfigurable Optical OFDM Access Networks," *Journal of Lightwave Technology,* vol. 30, pp. 3972-3979, 2012/12/15 2012.

[55] X. Liu and F. Buchali, "Intra-symbol frequency-domain averaging basedchannel estimation for coherent optical OFDM," *Optics Express,* vol. 16, pp. 21944-21957, 2008/12/22 2008.

[56] R. Mailloux, *Phased Arrya Antenna Handbook*: Artech House, 2005.

[57] M. Skolnik, *Radar Handbook*, 3 ed.: McGrawHill Publishing, 2001.

[58] I. Frigyes and A. J. Seeds, "Optically generated true-time delay in phased-array antennas," *Microwave Theory and Techniques, IEEE Transactions on,* vol. 43, pp. 2378-2386, 1995.

[59] W. Ng, A. A. Walston, G. L. Tangonan, J. J. Lee, I. L. Newberg, and N. Bernstein, "The first demonstration of an optically steered microwave phased array antenna using true-time-delay," *Lightwave Technology, Journal of,* vol. 9, pp. 1124-1131, 1991.

[60] O. Raz, S. Barzilay, R. Rotman, and M. Tur, "Submicrosecond Scan-Angle Switching Photonic Beamformer With Flat RF Response in the C and X Bands," *Lightwave Technology, Journal of,* vol. 26, pp. 2774-2781, 2008.

[61] B. Vidal, J. L. Corral, and J. Marti, "Optical delay line employing an arrayed waveguide grating in fold-back configuration," *Microwave and Wireless Components Letters, IEEE,* vol. 13, pp. 238-240, 2003.

[62] S. Yegnanarayanan, P. D. Trinh, and B. Jalali, "Recirculating photonic filter: a wavelength-selective time delay for phased-array antennas and wavelength code-division multiple access," *Optics Letters,* vol. 21, pp. 740-742, 1996/05/15 1996.

[63] F. M. Soares, F. Karouta, E. Smalbrugge, M. K. Smit, J. j. M. Binsma, J. Lopez, *et al.*, "An InP-based photonic integrated beamformer for phased-array antennas," in *Optical Amplifiers and Their*

Applications/Integrated Photonics Research, San Francisco, California, 2004, p. IFB2.

[64] R. G. Broeke, C. Jin, J. Chen, S. Sang-Woo, D. Yixue, N. K. Fontaine, *et al.*, "Optical-CDMA in InP," *Selected Topics in Quantum Electronics, IEEE Journal of*, vol. 13, pp. 1497-1507, 2007.

[65] Z. Leimeng, C. G. H. Roeloffzen, A. Meijerink, M. Burla, D. Marpaung, A. Leinse, *et al.*, "Novel Ring Resonator-Based Integrated Photonic Beamformer for Broadband Phased Array Receive Antennas—Part II: Experimental Prototype," *Lightwave Technology, Journal of*, vol. 28, pp. 19-31, 2010.

[66] L. Zhuang, C. G. H. Roeloffzen, R. G. Heideman, A. Borreman, A. Meijerink, and W. van Etten, "Single-Chip Ring Resonator-Based 1 × 8 Optical Beam Forming Network in CMOS-Compatible Waveguide Technology," *Photonics Technology Letters, IEEE*, vol. 19, pp. 1130-1132, 2007.

[67] M. S. Rasras, C. K. Madsen, M. A. Cappuzzo, E. Chen, L. T. Gomez, E. J. Laskowski, *et al.*, "Integrated resonance-enhanced variable optical delay lines," *Photonics Technology Letters, IEEE*, vol. 17, pp. 834-836, 2005.

[68] G. Lenz, B. J. Eggleton, C. K. Madsen, and R. E. Slusher, "Optical delay lines based on optical filters," *Quantum Electronics, IEEE Journal of*, vol. 37, pp. 525-532, 2001.

[69] C. K. Madsen and G. Lenz, "Optical all-pass filters for phase response design with applications for dispersion compensation," *Photonics Technology Letters, IEEE*, vol. 10, pp. 994-996, 1998.

[70] C. K. Madsen, "General IIR optical filter design for WDM applications using all-pass filters," *Lightwave Technology, Journal of*, vol. 18, pp. 860-868, 2000.

[71] A. Meijerink, C. G. H. Roeloffzen, R. Meijerink, Z. Leimeng, D. A. I. Marpaung, M. J. Bentum, *et al.*, "Novel Ring Resonator-Based Integrated Photonic Beamformer for Broadband Phased Array Receive Antennas—Part I: Design and Performance Analysis," *Lightwave Technology, Journal of*, vol. 28, pp. 3-18, 2010.

[72] H. Huang, S. R. Nuccio, Y. Yue, J. Yang, Y. Ren, C. Wei, *et al.*, "Broadband Modulation Performance of 100-GHz EO Polymer MZMs," *Lightwave Technology, Journal of*, vol. 30, pp. 3647-3652, 2012.

[73] M. Jarrahi, T. H. Lee, and D. A. B. Miller, "Wideband, Low Driving Voltage Traveling-Wave Mach-Zehnder Modulator for RF Photonics," *Photonics Technology Letters, IEEE*, vol. 20, pp. 517-519, 2008.

[74] H. Ito, S. Kodama, Y. Muramoto, T. Furuta, T. Nagatsuma, and T. Ishibashi, "High-speed and high-output InP-InGaAs unitraveling-carrier photodiodes," *Selected Topics in Quantum Electronics, IEEE Journal of,* vol. 10, pp. 709-727, 2004.

[75] E. Rouvalis, M. Chtioui, F. van Dijk, F. Lelarge, M. J. Fice, C. C. Renaud, *et al.*, "170 GHz uni-traveling carrier photodiodes for InP-based photonic integrated circuits," *Opt. Express,* vol. 20, pp. 20090-20095, 2012.

[76] R. K. Mohan, Z. W. Barber, C. Harrington, and W. R. Babbitt, "Frequency Resolved Angle and Time Difference of Arrival Estimation with Spatial Spectral Holography," 2010, p. OWF3.

[77] S. Pan, J. Fu, and J. Yao, "Photonic approach to the simultaneous measurement of the frequency, amplitude, pulse width, and time of arrival of a microwave signal," *Opt. Lett.,* vol. 37, pp. 7-9, 2012.

[78] B. Vidal, M. Á. Piqueras, and J. Mart į "Direction-of-Arrival Estimation of Broadband Microwave Signals in Phased-Array Antennas Using Photonic Techniques," *J. Lightwave Technol.,* vol. 24, p. 2741, 2006.

[79] X. Zou, W. Li, W. Pan, B. Luo, L. Yan, and J. Yao, "Photonic approach to the measurement of time-difference-of-arrival and angle-of-arrival of a microwave signal," *Opt. Lett.,* vol. 37, pp. 755-757, 2012.

[80] Q. Dayou, C. Neda, H. Junqiang, and W. Ting, "Optical OFDM Transmission in Metro/Access Networks," in *Optical Fiber Communication Conference*, 2009, p. OMV1.

[81] Y. Jianjun, D. Ze, X. Xin, X. Yan, S. Sheping, G. Chao, *et al.*, "Generation, transmission and coherent detection of 11.2 Tb/s (112×100Gb/s) single source optical OFDM superchannel," in *Optical Fiber Communication Conference and Exposition (OFC/NFOEC), 2011 and the National Fiber Optic Engineers Conference*, 2011, pp. 1-3.

[82] X. Xin, L. Zhang, B. Liu, and J. Yu, "Dynamic λ-OFDMA with selective multicast overlaid," *Opt. Express,* vol. 19, pp. 7847-7855, 2011.

[83] Q. Dayou, N. Cvijetic, H. Junqiang, and W. Ting, "108 Gb/s OFDMA-PON With Polarization Multiplexing and Direct Detection," *Lightwave Technology, Journal of,* vol. 28, pp. 484-493, 2010.

[84] E. Giacoumidis, J. L. Wei, X. L. Yang, A. Tsokanos, and J. M. Tang, "Adaptive-Modulation-Enabled WDM Impairment Reduction in Multichannel Optical OFDM Transmission Systems for Next-Generation PONs," *Photonics Journal, IEEE*, vol. 2, pp. 130-140, 2010.

[85] R. P. Giddings, E. Hugues-Salas, B. Charbonnier, and J. M. Tang, "Experimental Demonstration of Real-Time Optical OFDM

Transmission at 11.25 Gb/s Over 500-m MMFs Employing Directly Modulated DFB Lasers," *Photonics Technology Letters, IEEE,* vol. 23, pp. 51-53, 2011.

[86] S. L. Jansen, I. Morita, T. C. W. Schenk, and H. Tanaka, "121.9-Gb/s PDM-OFDM Transmission With 2-b/s/Hz Spectral Efficiency Over 1000 km of SSMF," *Lightwave Technology, Journal of,* vol. 27, pp. 177-188, 2009.

[87] Y. Jianjun, D. Ze, S. Yufeng, C. Nan, C. Lin, and C. Gee-Kung, "400 Gb/s optical packet switching node design with coherent detection," in *Optical Fiber Communication Conference and Exposition (OFC/NFOEC), 2011 and the National Fiber Optic Engineers Conference*, 2011, pp. 1-3.

[88] D. Ze, Y. Jianjun, T. Xiangfeng, and J. Wei, "432Gbit/s O-OFDM QPSK signal transmission over 400km SMF-28 with EDFA-only amplification," in *Optical Fiber Communication Conference and Exposition (OFC/NFOEC), 2011 and the National Fiber Optic Engineers Conference*, 2011, pp. 1-3.

[89] B. Skubic, C. Jiajia, J. Ahmed, C. Biao, L. Wosinska, and B. Mukherjee, "Dynamic bandwidth allocation for long-reach PON: overcoming performance degradation," *Communications Magazine, IEEE,* vol. 48, pp. 100-108, 2010.

[90] B. Skubic, C. Jiajia, J. Ahmed, L. Wosinska, and B. Mukherjee, "A comparison of dynamic bandwidth allocation for EPON, GPON, and next-generation TDM PON," *Communications Magazine, IEEE,* vol. 47, pp. S40-S48, 2009.

[91] J. A. Lazaro, C. Bock, V. Polo, R. I. Martinez, and J. Prat, "Remotely amplified combined ring-tree dense access network architecture using reflective RSOA-based ONU," *J. Opt. Netw.*, vol. 6, pp. 801-807, 2007.

[92] P. J. Urban, F. M. Huijskens, G. D. Khoe, A. M. J. Koonen, and H. de Waardt, "Reconfigurable WDM/TDM Access Network Providing 10-Gb/s/λ Over 27-km SSMF With Colorless ONU," *Photonics Technology Letters, IEEE,* vol. 21, pp. 1758-1760, 2009.

[93] P. J. Urban, B. Huiszoon, R. Roy, M. M. de Laat, F. M. Huijskens, E. J. Klein, *et al.*, "High-Bit-Rate Dynamically Reconfigurable WDM-TDM Access Network," *Optical Communications and Networking, IEEE/OSA Journal of,* vol. 1, pp. A143-A159, 2009.

[94] T. Koonen, "Fiber to the Home/Fiber to the Premises: What, Where, and When?," *Proceedings of the IEEE*, vol. 94, pp. 911-934, 2006.

[95] Z. Cao, J. Yu, W. Wang, L. Chen, and Z. Dong, "Direct-Detection Optical OFDM Transmission System Without Frequency Guard Band," *Photonics Technology Letters, IEEE,* vol. 22, pp. 736-738, 2010.

[96] R. C. DiPietro, "An FFT based technique for suppressing narrow-band interference in," in *Acoustics, Speech, and Signal Processing, 1989. ICASSP-89., 1989 International Conference on*, 1989, pp. 1360-1363 vol.2.

[97] C. Zizheng, Y. Jianjun, W. Wenpei, C. Lin, and D. Ze, "Direct-Detection Optical OFDM Transmission System Without Frequency Guard Band," *Photonics Technology Letters, IEEE,* vol. 22, pp. 736-738, 2010.

[98] J. Armstrong, "OFDM for Optical Communications," *Lightwave Technology, Journal of,* vol. 27, pp. 189-204, 2009.

[99] Z. Cao, F. Li, H. P. A. van den Boom, E. Tangdiongga, and A. M. J. Koonen, "Optical true-time-delay microwave beam-steering with 1 Gb/s wireless transmission for in-building networks," in *Optical Communication (ECOC 2013), 39th European Conference and Exhibition on*, 2013, pp. 1-3.

[100] Z. Cao, F. Li, A. C. F. Reniers, C. W. Oh, H. P. A. van den Boom, E. Tangdiongga, *et al.*, "Spatial Filtering in a Broadband In-Home OFDM Radio-Over-Fiber Network," *Photonics Technology Letters, IEEE,* vol. 26, pp. 575-578, 2014.

[101] Y. Jianping, Y. Jianliang, and L. Yunqi, "Continuous true-time-delay beamforming employing a multiwavelength tunable fiber laser source," *Photonics Technology Letters, IEEE,* vol. 14, pp. 687-689, 2002.

[102] L. Jofre, C. Stoltidou, S. Blanch, T. Mengual, B. Vidal, J. Marti, *et al.*, "Optically Beamformed Wideband Array Performance," *Antennas and Propagation, IEEE Transactions on,* vol. 56, pp. 1594-1604, 2008.

[103] B. Vidal, T. Mengual, C. Ibanez-Lopez, and J. Marti, "Optical Beamforming Network Based on Fiber-Optical Delay Lines and Spatial Light Modulators for Large Antenna Arrays," *Photonics Technology Letters, IEEE,* vol. 18, pp. 2590-2592, 2006.

[104] M. A. Piqueras, G. Grosskopf, B. Vidal, J. Herrera, J. M. Martinez, P. Sanchis, *et al.*, "Optically beamformed beam-switched adaptive antennas for fixed and mobile broad-band wireless access networks," *Microwave Theory and Techniques, IEEE Transactions on,* vol. 54, pp. 887-899, 2006.

[105] B. Vidal, J. L. Corral, M. A. Piqueras, and J. Marti, "Optical delay line based on arrayed waveguide gratings' spectral periodicity and dispersive media for antenna beamforming applications," *Selected Topics in Quantum Electronics, IEEE Journal of,* vol. 8, pp. 1202-1210, 2002.

[106] Z. Cao, F. Li, A. Reniers, C. W. Oh, H. van den Boom, E. Tangdiongga, *et al.*, "Spatial Filtering in a Broadband In-Home OFDM Radio-Over-

Fibre Network," *Photonics Technology Letters, IEEE,* vol. PP, pp. 1-1, 2014.

[107] Z. Cao, R. Lu, Q. Wang, N. Tessema, Y. Jiao, H. P. A. van den Boom, *et al.*, "Cyclic additional optical true time delay for microwave beam steering with spectral filtering," *Optics Letters,* vol. 39, pp. 3402-3405, 2014/06/15 2014.

[108] X. Li, Z. Cao, J. Zhang, F. Li, and G.-K. Chang, "Ultra-high-speed fiber-wireless-fiber link for emergency communication system," in *Optical Fiber Communication Conference*, 2014, p. M3D. 6.

Acronyms

AA	Aperture Antenna
ABC	Automatic Bias Control
AF	Array Factor
AOA	Angle-Of-Arrival
ASE	Amplified Spontaneous Emission
ATT	Optical Attenuator
AW	Arrayed Waveguide
AWG	Arbitrary Waveform Generator
AWG	Arrayed waveguide grating
AWG-loop	Arrayed Waveguide Grating Feedback Loop
BB	Baseband
BER	Bit Error Rate
BERT	Bit Error Rate Tester
BII	Beating Induced Interference
BS	Base Station
BS	Beam Steering
BTB	Back-To-Back
BW	Bandwidth
CA	Carrier Aggregation
CAO-TTD	Cyclic Additional Optical True Time Delay
CAPEX	Capital Expenditures
CF	Cleaved Single Mode Fibre
Cir	Optical Circulator
CO	Central Office
CODL	Compensation Optical Delay Line
CoMP	Coordinated Multipoint
CS	Central Station
CS	Channel Spacing

CW	Continuous Wave
DAC	Digital To Analog Converter
DBA	Dynamic Bandwidth Allocation
DC	Direct Current
DCA	Dynamic Channel Allocation
DEMUX	De-Multiplexer
DE-MZM	Dual-Electrode Mach-Zehnder
DFB	Distributed Feed Back
D-FDM	Digital Frequency Division Multiplexing
DMOC	Data Modulated Optical Carrier
DSP	Digital Signal Processing
EA	Electrical Amplifier
ECL	External Cavity Laser
EDFA	Erbium Doped Fibre Amplifier
EM	External Modulation
EMI	Electromagnetic Interference
EOM	Electro-Optical Modulator
ER	Extinction Ratio
ETI	Electrical Tone Injection
EVM	Error Vector Magnitude
FBG	Fibre Bragg Grating
FFP	Far Field Pattern
FFT	Fast Fourier Transform
FGC	Fibre Grating Coupler
FGI	Frequency Guard Interval
FPR	Free Propagation Region
FSR	Free Spectral Range
FTTH	Fibre-To-The-Home
Full HD	Full High Definition
FV-FDM	Full-Vector Finite Difference Method
FWM	Four Wave Mixing
GW	Gateway
HA1/2-R	Receiver Horn Antennas
HA1/2-T	Transmitter Horn Antennas
HCC	Home Communication Controller
HetNets	Heterogeneous Networks
HFGB	High Frequency Guard Band
HPF	High Pass Filters
ICI	Inter Carrier Interference

IFFT	Inverse Fast Fourier Transform
IFiWiNs	Indoor Fibre-Wireless Networks
IIR	Infinite Impulse Response
IM	Intensity Modulator
IM-PODD	Intensity Modulation parallelel optical delay detector
ISFA	Intra-Symbol Frequency-Domain Averaging
ISM	Industrial, Scientific, And Medical
IE	Indoor Exchange
LFD	Low Frequency Detection
LFCIE	Low Frequency Channel Insertion and Extraction
LNA	Low Noise Amplifier
LO	Local Oscillator
LPF	Low Pass Filter
LTE	Long Term Evolution
MD	Mobile Device
MIMO	Multiple-Input Multiple-Output
MMF	Multimode Fiber
mm-wave	Millimeter-Wave
MUX	Multiplexer
MZM	Mach-Zehnder Modulator
NG-PON	Next Generation Passive Optical Network
NLoS	Non-Line-Of-Sight
O/E	Optical-Electrical Convertor
OAN	Optical Access Network
OBPF	Optical Band-Pass Filter
OC	Optical Coupler
ODL	Optical Delay Line
ODN	Optical Delay Network
ODW	Optical Data Wavelength
OFDM	Orthogonal Frequency Division Multiplexing
OH	Optical Heterodyne
OLO	Optical Local Oscillator
OMI	Optical Modulation Index
OMW	Optical Mm-wave
ONF	Optical Notch Filter

ONU	Optical Network Unit
OOFDM	Optical Orthogonal Frequency Division Multiplexing
OOK	On-Off Keying
OPEX	Operational Expenditure
ORBS-RoF	Optical Radio Beam Steered Radio Over Fibre Systems
OTTD	Optical True Time Delay
OTTD-RBS	Optical True Time Delay Radio Beam Steering
PAA	Phased Array Antenna
PBC	Polarization Beam Combiner
PBS	Polarization Beam Splitter
PC	Polarization Controller
PD	Photodiode
PM-PODD	Phase Modulation Parallel Optical Delay Detector
P-MZM	Parallel Mach-Zehnder Modulator
PODD	Parallel Optical Delay Detectors
POF	Plastic Optical fiber
PolMux	Polarization Multiplexing
PolMux-OH	Polarization Multiplexing And Optical Heterodyne
PON	Passive Optical Networks
PS	Phase Shift
PSR	Power Suppression Ratio
QPSK	Quadrature Phase Shift Keying
RAP	Remote Access Point
RFSA	Radio Frequency Spectrum Analyzer
RLPF	Rectangular Low-Pass Filter
RN	Reconfigurable Nodes
RoF	Radio-Over-Fibre
ROP	Received Optical Powers
RSOA	Reflective Semiconductor Optical Amplifier
RTO	Real Time Oscilloscope
RUC	Remote Up-conversion
Rx	Receivers
SC-AWG-loop	Spectral-Cyclic Arrayed Grating Waveguide Feedback Loop

SMF	Single-Mode fiber
SOA	Semiconductor Optical Amplifier
SoI	Silicon-On-Insulator
SOWICI	Smart Optical Wireless In-Home Communication Infrastructure
SRO	Scientific Research Objectives
SSC	Spot Size Convertor
TDM	Time Division Multiplexing
TDOA	Time Difference Of Arrival
TL	Tunable Laser
TS	Training Sequence
TTD	True Time Delay
TU	Terminal User
VHT	Very High Throughput
VNA	Vector Network Analyzer
VOA	Variable Optical Attenuator
WDM	Wavelength Division Multiplexing
WDM-TDM	Wavelength Division Multiplexing And Time Division Multiplexing
WLAN	Wireless Local Area Networks
XGM	Cross Gain Modulation

List of Publications

Journals

1. Z. Cao, F. Li, Y. Liu, J. Yu, Q. Wang, C.W. Oh, Y. Jiao, N.C. Tran, H.P.A. van den Boom, E Tangdiongga, and A.M.J. Koonen, "61.3-Gbps Hybrid Fibre-Wireless In-Home Network Enabled by Optical Heterodyne and Polarization Multiplexing" IEEE/OSA Journal of Lightwave Technology, vol.32, 3227-3233， 2014.
2. Z. Cao, R. Lu, Q. Wang, N. Tessema, Y. Jiao, H. P. A. Van den Boom, E. Tangdiongga, A. M. J. Koonen, "Cyclic additional optical true time delay for microwave beam steering with spectral filtering" OSA Optics Letters, vol. 39, 3402-3405, 2014.
3. Z. Cao, H. P. A. Van den Boom, E. Tangdiongga, A. M. J. Koonen," Interleaved and Partial Transmission Interleaved Optical Coherent OFDM" OSA Optics Letters, vol. 39, pp. 2179-2182, 2014.
4. Z. Cao, Q. Wang, R. Lu, H. P. A. Van den Boom, E. Tangdiongga, A. M. J. Koonen, "Phase modulation parallel optical delay detector for microwave angle-of-arrival measurement with accuracy monitored" OSA Optics Letters, vol. 39, pp.1497-1500, 2014
5. Z. Cao, F. Li, A. Reniers, C. W. Oh, H. van den Boom, E. Tangdiongga, and A. M. J. Koonen, "Spatial Filtering in a Broadband In-Home OFDM Radio-Over-Fibre Network," Photonics Technology Letters, IEEE, vol. PP, pp. 1-1, 2014.
6. Z. Cao, G. Wen, F. Li, Q. Shu, J. Yu, and L. Chen, "Unbalanced impairments compensation for low cost direct detection OFDM-PON systems," Optics Communications, vol. 310, pp. 35-41, 2014.
7. Z. Cao, J. Yu, F. Li, L. Chen, Q. Shu, Q. Tang, and L. Chen, "Energy Efficient and Transparent Platform for Optical Wireless Networks Based on Reverse Modulation," IEEE Journal on Selected Areas in Communications, vol. 31, pp. 804-814, 2013.

8. Z. Cao, F. Li, C. M. Okonkwo, H. P. A. van den Boom, M. Chen, B. Yang, S. Zou, E. Tangdiongga, L. Chen, and A. M. J. Koonen, "Synchronized signaling delivery for broadband 60 GHz in-building optical wireless network based on digital frequency division multiplexing and digital Nyquist shaping," Optics Express, vol. 21, pp. 270-275, 2013.
9. Z. Cao, H. P. A. van den Boom, C. M. Okonkwo, E. Tangdiongga, and A. M. J. Koonen, "Simultaneous provision of wired service and dispersion-robust 60GHz wireless service in radio-over-fibre system based on remote up-conversion with electrical tones injection," Optics Communications, vol. 311, pp. 346-349, 2013.
10. Z. Cao, G. Wen, L. Chen, Q. Shu, and L. Chen, "Comparison of interpolation methods for pilot aided estimation in direct-detection optical OFDM system," Microwave and Optical Technology Letters, vol. 55, pp. 2604-2608, 2013.
11. Z. Cao, H. P. A. van den Boom, E. Tangdiongga, K. Chandra, and A. M. J. Koonen, "Long Reach Hybrid Fibre-Wireless System With Remote Up-Conversion and Local Exchange," Photonics Technology Letters, IEEE, vol. 25, pp. 737-740, 2013.
12. Z. Cao, H. P. A. van den Boom, L. Rongguo, W. Qing, E. Tangdiongga, and A. M. J. Koonen, "Angle-of-Arrival Measurement of a Microwave Signal Using Parallel Optical Delay Detector," Photonics Technology Letters, IEEE, vol. 25, pp. 1932-1935, 2013.
13. Z. Cao, J. Yu, L. Chen, and Q. Shu, "Reversely Modulated Optical Single Sideband Scheme and Its Application in a 60-GHz Full Duplex ROF System," Photonics Technology Letters, IEEE, vol. 24, pp. 827-829, 2012.
14. Z. Cao, F. Li, C. M. Okonkwo, H. P. A. Van den Boom, E. Tangdiongga, Q. Tang, J. Tang, J. Yu, L. Chen, and A. M. J. Koonen, "A Synchronized Signaling Insertion and Detection Scheme for Reconfigurable Optical OFDM Access Networks," *Journal of Lightwave Technology,* vol. 30, pp. 3972-3979, 2012.
15. Z. Cao, L. Zou, L. Chen, and J. Yu, "Impairment Mitigation for a 60-GHz OFDM Radio-Over-Fibre System Through an Adaptive Modulation Technique," IEEE/OSA Journal of Optical Communications and Networking, vol. 3, pp. 758-766, 2011.
16. Z. Cao, J. Yu, M. Xia, Q. Tang, Y. Gao, W. Wang, and L. Chen, "Reduction of Intersubcarrier Interference and Frequency-Selective Fading in OFDM-ROF Systems," Journal of Lightwave Technology, vol. 28, pp. 2423-2429, 2010. (Invited paper)

17. Z. Cao, J. Yu, W. Wang, L. Chen, and Z. Dong, "Direct-Detection Optical OFDM Transmission System Without Frequency Guard Band," Photonics Technology Letters, IEEE, vol. 22, pp. 736-738, 2010.
18. Z. Cao, J. Yu, H. Zhou, W. Wang, M. Xia, J. Wang, Q. Tang, and L. Chen, "WDM-RoF-PON Architecture for Flexible Wireless and Wire-Line Layout," IEEE/OSA Journal of Optical Communications and Networking, vol. 2, pp. 117-121, 2010.
19. Z. Cao, J. Yu, Q. Tang, G. Zeng, and L. Chen, "Long-reach 60-GHz radio-over-fibre system based on turbo-coded OFDM," Chinese Optics Letters, vol. 8, pp. 1024-1027, 2010.
20. Z. Cao, J. Yu, W. Wang, Q. Tang, and L. Chen, "Low-cost 60-GHz radio-over-fibre architecture compatible with wavelength-division-multiplexing passive optical networks by employing directly modulated laser and frequency quadruple techniques," Optical Engineering, vol. 49, pp. 065005-065005-3, 2010.
21. C. Oh, F. Huijskens, Z. Cao, E. Tangdiongga, and A. Koonen, "Toward multi-Gbps indoor optical wireless multicasting system employing passive diffractive optics," Optics letters, vol. 39, pp. 2622-2625, 2014.
22. L. Chen, J. He, Y. Liu, L. Chen, and Z. Cao, "Comparison of interpolation algorithms for pilot-aided estimation of orthogonal frequency division multiplexing transmission in reversely modulated optical single sideband system," Optical Engineering, vol. 53, pp. 056108-056108, 2014.
23. M. Chen, J. He, Z. Cao, J. Tang, L. Chen, and X. Wu, "Symbol synchronization and sampling frequency synchronization techniques in real-time DDO-OFDM sy[108]stems," Optics Communications, vol. 326, pp. 80-87, 2014.
24. Q. Tang, J. He, Z. Cao, F. Li, J. Xiao, and L. Chen, "Polarization-time-block-code in IM/DD PolMux-OFDM transmission system," *Optics Communications,* vol. 315, pp. 295-302, 2014.
25. F. Li, J. Zhang, Z. Cao, J. Yu, X. Li, L. Chen, Y. Xia, and Y. Chen, "Transmission and reception of Quad-Carrier QPSK-OFDM signal with blind equalization and overhead-free operation," *Optics Express,* vol. 21, pp. 30999-31005, 2013.
26. F. Li, Z. Cao, X. Li, Z. Dong, and L. Chen, "Fibre-Wireless Transmission System of PDM-MIMO-OFDM at 100 GHz Frequency," *Journal of Lightwave Technology,* vol. 31, pp. 2394-2399, 2013.
27. D. Ze, L. Xinying, Y. Jianjun, C. Zizheng, and C. Nan, "8x9.95-Gb/s Ultra-Dense WDM-PON on a 12.5-GHz Grid With Digital Pre-Equalization," *Photonics Technology Letters, IEEE,* vol. 25, pp. 194-197, 2013.

28. H. Chen, J. Yu, J. Xiao, Z. Cao, F. Li, and L. Chen, "Nonlinear effect mitigation based on PAPR reduction using electronic pre-distortion technique in direct-detection optical OFDM system," *Optical Fibre Technology,* vol. 19, pp. 387-391, 2013.
29. J. Xiao, J. Yu, Z. Cao, F. Li, and L. Chen, "Flipped-exponential Nyquist pulse technique to optimize the PAPR in optical direct detection OFDM system," *Optics Communications,* vol. 286, pp. 176-181, 2013.
30. Q. Tang, J. Yu, Z. Cao, J. Xiao, X. Li, M. Fall, and L. Chen, "Joint adaptive code rate technique and bit interleaver for direct-detection optical OFDM system," *Optical Fibre Technology,* vol. 19, pp. 35-39, 2013.
31. Q. Shu, L. Chen, Z. Cao, and L. Chen, "Frequency domain pilot interval allocation optimization for compatible single-sideband modulation orthogonal frequency division multiplexing transmission with direct detection," *Optical Engineering,* vol. 52, pp. 045006-045006, 2013.
32. G. Wen, J. Xiao, Z. Cao, F. Li, L. Chen, X. Li, and M. Chen, "Experimental investigation of pilot power allocation in direct-detected optical orthogonal frequency division multiplexing system," *Optical Engineering,* vol. 52, pp. 015009-015009, 2013.
33. X. Li, J. Yu, Z. Dong, Z. Cao, N. Chi, J. Zhang, Y. Shao, and L. Tao, "Seamless integration of 57.2-Gb/s signal wireline transmission and 100-GHz wireless delivery," *Optics Express,* vol. 20, pp. 24364-24369, 2012.
34. X. Jiangnan, Y. Jianjun, L. Xinying, T. Qi, C. Hongxian, L. Fan, C. Zizheng, and C. Lin, "Hadamard transform combined with companding transform technique for PAPR reduction in an optical direct-detection OFDM system," *Optical Communications and Networking, IEEE/OSA Journal of,* vol. 4, pp. 709-714, 2012.
35. J. Xiao, J. Yu, X. Li, Q. Tang, H. Chen, F. Li, Z. Cao, and L. Chen, "Hadamard Transform Combined With Companding Transform Technique for PAPR Reduction in an Optical Direct-Detection OFDM System," *Journal of Optical Communications and Networking,* vol. 4, pp. 709-714, 2012.
36. F. Li, Z. Cao, G. Wen, J. Xiao, J. Yu, and L. Chen, "Optimization of pilot interval design in direct-detected optical OFDM system," *Optics Communications,* vol. 285, pp. 3075-3081, 2012.
37. F. Li, J. Yu, Z. Cao, J. Xiao, H. Chen, and L. Chen, "Reducing the Peak-to-Average Power Ratio With Companding Transform Coding in 60 GHz OFDM-ROF Systems," *Journal of Optical Communications and Networking,* vol. 4, pp. 202-209, 2012.

38. X. Wang, J. Yu, Z. Cao, J. Xiao, and L. Chen, "SSBI mitigation at 60GHz OFDM-ROF system based on optimization of training sequence," *Optics Express,* vol. 19, pp. 8839-8846, 2011.
39. Q. Tang, L. Chen, J. Xiao, and Z. Cao, "Experiment on 60-GHz MMW transmission performance in an optical fibre andwireless system," *Chinese Optics Letters,* vol. 9, p. 050601, 2011.
40. Y. Gao, J. Yu, J. Xiao, Z. Cao, F. Li, and L. Chen, "Direct-Detection Optical OFDM Transmission System With Pre-Emphasis Technique," *Journal of Lightwave Technology,* vol. 29, pp. 2138-2145, 2011.
41. F. Li, J. Yu, J. Xiao, Z. Cao, and L. Chen, "Reduction of frequency fading and imperfect frequency response with pre-emphasis technique in OFDM-ROF systems," *Optics Communications,* vol. 284, pp. 4699-4705, 2011.
42. J. He, Z. Cao, L. Chen, and S. Wen, "Full-duplex radio-over-fibre system with quadrature-amplitude-modulation photonically generated orthogonal frequency-division multiplexing signals," *Optical Engineering,* vol. 49, pp. 065003-065003-5, 2010.
43. L. Chen, J. Lu, Z. Dong, Z. Cao, S. Wen, and J. Yu, "Polarization insensitive all-optical up-conversion for ROF systems based on parallel pump FWM in a SOA," *Optics Express,* vol. 17, pp. 6962-6967, 2009.
44. J. Lu, L. Chen, Z. Dong, Z. Cao, and W. Shuangchun, "Polarization Insensitive Wavelength Conversion Based on Orthogonal Pump Four-Wave Mixing for Polarization Multiplexing Signal in High-Nonlinear Fibre," *Lightwave Technology, Journal of,* vol. 27, pp. 5767-5774, 2009.
45. Z. Dong, Z. Cao, J. Lu, Y. Li, L. Chen, and S. Wen, "Transmission performance of optical OFDM signals with low peak-to-average power ratio by a phase modulator," *Optics Communications,* vol. 282, pp. 4194-4197, 2009.

International Conferences

46. Z. Cao, A. M. J. Koonen, Y. Jiao, Q. Wang, Henrie P. A. Van den Boom, E. Tangdiongga, "In-home Fibre Wireless Networks Incorporating Optical Microwave Beam Steering: System Architecture and Integrated Device," presented at the Progress In Electromagnetics Research Symposium 2014, Guangzhou, China, 2014.(Invited talk)
47. Z. Cao, Q. Wang, N.Tessema, X. Parareda, H.P.A. van den Boom, E. Tangdiongga, and A.M.J. Koonen " Electrically-Controlled Optical Phase Shifter for Broadband Radio Orbital Angular Momentum Mode

Generation " in Optical Communication (ECOC 2014), 40th European Conference and Exhibition on, Cannes, 2014.

48. Z. Cao, A. M. J. Koonen, R. Lu, Y. Jiao, Q. Wang, H. P. A. van den Boom, and E. Tangdiongga, " An Integrated Step-Wise Optical Tunable True-Time-Delay System for the Microwave Beam Steering Towards In-Home Devices ", OECC/ACOFT 2014, 2014, Accepted.
49. Z. Cao, Q. Wang, R. Lu, A. Reniers, H. Boom, E. Tangdiongga, A. M. J. Koonen, " Microwave Beamsteering with Tunable Spectral Filtering Using Cyclic Additional Optical True Time Delay ", Optical Fibre Communication Conference/National Fibre Optic Engineers Conference 2014 (OFC2014), 2014, p. TH3D.2.
50. Z. Cao, H. Boom, M. Chen, E. Tangdiongga, L. Chen, and A.M.J. Koonen, "Angle-of-arrival Measurement of a Microwave Signal Based on Parallel Optical Delay Detector with Accuracy Monitored," in Optical Fibre Communication Conference/National Fibre Optic Engineers Conference 2013 (OFC2013), Anaheim, California, 2013, p. OTh3D.6.
51. Z. Cao, F. Li, H. P. A. van den Boom, E. Tangdiongga, and A. M. J. Koonen, "Optical true-time-delay microwave beam-steering with 1 Gb/s wireless transmission for in-building networks," in Optical Communication (ECOC 2013), 39th European Conference and Exhibition on, 2013, pp. 1-3.
52. Z. Cao, F. Li, P.A. Gamage, C. M. Okonkwo, H.P.A. van den Boom, M. Chen, S. Zou, B.Yang, E. Tangdiongga, L. Chen, A.M.J. Koonen "Synchronized Signaling Delivery for Very High Throughput 60GHz In-Building Optical Wireless Network Based on Digital Frequency Division Multiplexing and Digital Nyquist Shaping," in European Conference and Exhibition on Optical Communication (ECOC2012), Amsterdam, 2012, p. P6.11.
53. Z. Cao, C. M. Okonkwo, H. P. A. Van den Boom, B. Yang, S. Zou, M. Huang, E. Tangdiongga, and A. M. J. Koonen, "A simple and low cost remote-up-conversion scheme using only one optical modulator and its application in a 60GHz radio-over-fibre system," in Networks and Optical Communications (NOC), 2012 17th European Conference on, 2012, pp. 1-4.

54. X. Li, Z. Cao, J. Zhang, F. Li, and G.-K. Chang, "Ultra-high-speed fibre-wireless-fibre link for emergency communication system," in Optical Fibre Communication Conference, 2014, p. M3D. 6.
55. B. Yang, S. Zou, E. Tangdiongga, X. Jin, Z. Cao, C. Okonkwo, H. Chen, and T. Koonen, "A Lightwave Centralized and Dispersion Immune Bidirectional mm-Wave over Fibre Scheme for Access Networks," in *European Conference and Exhibition on Optical Communication*, Amsterdam, 2012, p. P6.07.
56. S. Zou, H. Chen, F. Huijskens, Z. Cao, E. Tangdiongga, and T. Koonen, "Demonstration of Fully Functional MIMO Wireless LAN Transmission over GI-MMF for In-building Networks," in *Optical Fibre Communication Conference/National Fibre Optic Engineers Conference 2013*, Anaheim, California, 2013, p. JTh2A.08.
57. S. Zou, C. Okonkwo, Z. Cao, N.-C. Tran, E. Tangdiongga, and T. Koonen, "Dynamic Optical Routing and Simultaneous Generation of Millimeter-Wave Signals for In-Building Access Network," in *Optical Fibre Communication Conference*, Los Angeles, California, 2012, p. OTh3G.6.
58. S. Zou, H. Chen, F. Huijskens, Z. Cao, E. Tangdiongga, and T. Koonen, "Demonstration of fully functional MIMO wireless LAN transmission over GI-MMF for in-building networks," in *Optical Fibre Communication Conference and Exposition and the National Fibre Optic Engineers Conference (OFC/NFOEC),* 2013, pp. 1-3.

Regional Conferences

59. Z. Cao, H.P.A. van den Boom, E. Tangdiongga, and A. M. J. Koonen. "Parallel optical delay detector for angle-of-arrival measurement of a microwave signal with accuracy monitoring", In X.J.M. Leijtens & D. Pustakhod (Eds.), Conference Paper : Proceedings of the 18th Annual Symposium of the IEEE Photonics Benelux Chapter, 25-26 November 2013, Technische Universiteit Eindhoven, (pp. 135-138). Eindhoven: Technische Universiteit Eindhoven.
60. Z. Cao, Y. Jiao, H.P.A. van den Boom, E. Tangdiongga, and A. M. J. Koonen. " Independent group delay and amplitude manipulation based on a micro-ring resonator for optical microwave beam-steering", Proceedings of the 17th Annual Symposium of the IEEE Photonics Society Benelux Chapter colocated with 'Workshop on random fibre lasers', 29-30 Novembre 2012, Mons, Belgium, Piscataway: IEEE Service Center.

61. Z. Cao, Y. Jiao, H.P.A. van den Boom, E. Tangdiongga, and A. M. J. Koonen. "A compact design of micro-ring resonator chains for optical phase manipulation", In P. Bienstman, G. Morthier, G. Roelkens & et al. (Eds.), Oral : Proceedings of the 16th Annual symposium of the IEEE Photonics Benelux Chapter, 01-02 December 2011, Ghent, Belgium, (pp. 121-124). Ghent, Belgium: Unversiteit Gent.

Patents

1. Optically Controlled Radio Beam Steering System. (US Provisional Patent, Application No. 61/928237)
2. OFDM radio-over-fiber systems with millimeter wave generation based on optical carrier suppress. (Chinese Patent, Publication No. CN101567745 A)
3. High frequency optical millimeter wave generation based on single sideband and wavelength reuse. (Chinese Patent, Publication No. CN101521962 B)

Acknowledgments

Four years ago in 2011, I was fortunate to start my Ph. D research in Eindhoven. During my four-year project, I am lucky to receive lots of help from many kind and generous people. Now, when I sat down to remember and type, it is joyful to write down these stories. It helps me to remark my life in marginalia of the elapsed times. Thanks for all Dutch tax payers (through NWO) from whom I am financially supported to finish my Ph. D research.

First of all, I would like to express my sincerest appreciation to my first promoter prof. Ton Koonen, who significantly influences my research career and partially shapes the way I think. In 2011, he gave me the opportunity to pursue my PhD studies in the ECO group. Since then, he always tried to find enough time to guide me and also proposed useful ideas to my research. These ideas make the thesis thicker than it should be. He always positively encourages me to deeply understand the research problems and to creatively obtain the good ideas. In our discussion, usually one part is for solving technical problems, and the other is to let me know how he could shape his opinion or idea. Without such careful guidance, I cannot be independent that fast. I appreciate all the knowledge and confidence I gained under his guidance.

The help and contributions from my co-promoter, dr. E. Tangdiongga are indispensable for my Ph. D. Dr. E. Tangdiongga is the second one who I 'overloaded', especially in the initial stage of my Ph. D. When I met with some challenging problems in either experimental setups or in theoretical analysis, he can always provide some useful information. His advices do help me to avoid some unnecessary detours approaching my Ph. D project. I also sincerely thank my daily supervisor ir. H.P.A. van der Boom for his generous time and energy to support me. Whenever I knock on his door, he always tries to keep enough time for our discussion.

The contributions from my defense committee are highly appreciated. All committee members, Prof. Hequan Wu, Prof. Ping Zhang (on behalf of Prof. Wu), Prof. J. Capmany, Dr. N. Gomes, Prof.dr.ir. M. K. Smit, and Prof.dr.ir. A. B. Smolders provide in-depth comments for improving the quality of this thesis.

Prof. Hequan Wu from Perking University, China carefully reviewed this thesis and provided a series of important comments and suggestions even when he was ill. Due to health reason, Prof. Hequan Wu kindly invited Prof. Ping Zhang from Beijing University of Post and Telecom, China to represent himself for the defense ceremony. Prof. Ping Zhang was so kind to respond rapidly and kindly helped to review this thesis and attend my Ph. D defense. About one year ago, Prof. J. Capmany kindly supported me for the application of graduate student fellowship from IEEE Photonics Society 2014. Prof. M. K. Smit kindly helped me to follow the regular research activities in PHI group.

During my four-year research, I frequently discussed with Dr. Chigo Okonkwo, Dr. Oded Raz, Dr. Nicola Calabretta, Dr. Patty Stabile, and Prof. Kevin William. Most discussion resulted in better technical choices and smarter designs. In the very initial stage of my Ph. D, Dr. Okonkwo helped me to initiate my experimental activities while Dr. Raz inspired me a lot in optical radio beam steering fields. Dr. Calabretta always provides good ideas once I met some practical experimental difficulties. Dr. Stabile helped me to build up the chip measurement test bed and also provided lots of assistance in our clean room. Prof. William taught me a lot about integrated photonic circuits.

My knowledge on integrated photonic circuit design started since JEPPIX training course in 2011. During that course, I met a lot of kind colleagues and professors from OED (now PHI) group. I bothered most of them with technical problems. Dr. Xaveer Leijtens taught me planar photonic circuit modelling in the JEPPIX course and in the following days, he provided a lot of useful knowledge support and technical discussion to help me overcome many academic difficulties. He always explains technical issues in an easy and relaxed way with his symbolic smiles. Dr. Erwin Bente opened the door for my understanding of semiconductor lasers from basic theory to practical measurement setup. His JEPPIX course is very interesting with many funny cartoons. First known through JEPPIX courses, Drs. Barry Smalbrugge helped me a lot to set up the integrated photonic circuit measurement test bed from 2011 to recent. Such help covers the chip mount, chip wire-bonding, water cooling systems and current injection setups.

In SOWICI project meetings, there are many active and smart scholars contribute to SOWICI project, which make our project meeting quite interesting. I enjoyed such brainstorm with them. I would like to thank Prof. Ignas Niemegeers, Prof. Sonia Heemstra de Groot, Prof. Gerard Smit, Dr. Venkatesha Prasad, Dr. Georgios Karagiannis, Dr. Anthony Lo, Mr. Kishor Chandra, Mr. Tom Bruintjes, and Qing Wang.

I would like to thank all ECO group members for their kind help, support and joyful daily life made by them. It is so happy to spend four year together with you all! I would like to express my appreciations to Dr. Huug de Waardt, who always help me to cope with practical lab issues; Prof. Harm Dorren and Prof. Antonio Liotta, for many inspired discussions near my office and the coffee machine; Dr. Rongguo Lu, Qing Wang, Prometheus DasMahapatra, Netsanet Tessema, Joanne Oh, Xavier Parareda, Xinran Zhao, and Zhongbiao Chen for their useful discussion, kind help and assistance for my lab works; ing. Frans Huijskens, and ing. Johan van Zantvoort for kind help on practical lab issues; Jose Hakkens, Jolanda Levering and Brigitta van Uitregt-Dekkers for warm assistance on every administrative matters; Dr. Hejie Yang, Dr. Pingxiang Duan and Dr. Jun Luo for nice assistance when I first time arrived in The Netherlands for my Ph. D interview; Dr. Nguyen Tran, Dr. Nikolaos Sotiropoulos, Dr. Abhinav Rohit, and Dr. Prasanna Gamage for their kind encourage and support during my Ph. D. I would like to thank my current officemates Prof. Yoshinobu Maeda, Hedde Bosman, Stefano Galzarano, Dr. Roy van Uden, Fulong Yan, and Shihuan Zou for the easy and funny daily life they make. I am equally thankful to the other ECO colleagues, Dr. Piet Kuindersma, Dr. Georgios Exarchakos, Dr. Jon Kjellman, Simone Cardarelli, Michele Chincoli, Diptanil Debbarma, Federico Forni, Roshan Kotian, Robbert van der Linden, Decebal Mocanu, Ketemaw Mekonnen, Gonzalo Guelbenzu de Villota, and Maria Torres Vega who together make the delight atmosphere. I would like to thank my former ECO colleagues, Dr. Haoshuo Chen, Dr. Aaron Albores-Mejia, Dr. Fausto Gomez-Agis, Dr. Jing Zhao, Dr. Karen Solis-Trapala, Dr. Rui Zhang, Dr. Solomon Abraha, Dr. Stefano Di Lucente, Dr. Vincent Sleier, and Dr. Vlado Menkovski. I really enjoyed the time we spent, worked and travelled together in Eindhoven and abroad, as well as the reunion time in the conferences. My special appreciation goes to my colleagues Xinran Zhao, Zhongbiao Chen and Netsanet Tessema who helped me to deal with the formation and checking of this thesis.

I also want to express my appreciations to all colleagues from the PHI group from whom I gained huge knowledge on integrated photonics circuits. Dr. Yuqing Jiao constantly helps and supports me since I started my research on integrated photonics circuits. Dr. Giovanni Gilardi and Dr. Sylwester Latkowski helped me to build up my lateral coupling system and the high-speed measurement setup for active integrated photonics circuit. Dr. Rui Santos, Weiming Yao and Valentina Moskalenko gave me a lot of patient discussions and useful suggestions for chip design and measurement. Dr. Jing Zhao, Dr. Katarzyna Ławniczuk and Dr. Luc Augustin helped me with my first AWG laser design.

For antenna design and measurement, I frequently discussed with and got support from ing. Ad Reniers, Mr. Mojtaba Zamani, Dr. Matti Herben and Dr. Mingda Huang from the EM group. For high-speed RF measurement, I want to thank Qian Ma, Yu Pei, and Chuang Lv for their useful discussions.

During my Ph. D, I gained a lot of knowledge and kind support from Arjen Bakker, Sesilia Kriswandhi, Dr. Remco Stoffer from Phoenix Software, Dr. Ronald Broeker from Bright Photonics, Dr. Francisco Soares from Fraunhofer Heinrich Hertz Institute, and Arne Leinse from Lionix regarding chip design and measurement. I would like to thank Dr. Jianjun Yu from ZTE US Optics Labs for his patient guidance for my career development, technical discussions, and kind support for carrying out my experiment in his lab. I want to express my appreciation to Dr. Jian Zhao from Tyndall institute, for his patient discussion in digital signal processing, and kind guidance for my career development.

I would also like to thank the "Chinese community" in ECO group: Chenhui Li, Teng Li, Wang Miao, Qing Wang, Fulong Yan, Xiu Zheng, and Shihuan Zou, as well as Yuqing Jiao, Longfei Shen, Weiming Yao and Dan Zhao from the PHI group, Lu Huang from the EM group for the happy moments we experienced together. Special thanks go to Wang Miao and his wife Shuli Wang for their indispensable help before and after my daughter Alicia’s birth.

I would like to thank Dr. Kangbo Lv, Dr. Jiang Zhou, our nice India neighbor Nidhi and Varun, and friends outside The Netherlands including Dr. Leimeng Zhuang from Monash University, Dr. Fan Li from ZTE US Optics Labs, Lianyan Li from Ghent University, Yuquan Wang from Royal Institute of Technology, for the delight moment they brought to me. Particularly, I would like to thank Dr. Delei Chen, for his encourage and support in my very difficult season, and for the joyful time he brought to me and my family during the whole four years.

I keep the last lines for my unique appreciations for my wife Qiaoqi (Sharon) Zhang, my daughter Alicia Cao, my parents, my parents in law, and all my relativities and friends.

Curriculum Vitae

Zizheng Cao received his Bachelor of Science degree on electronic information science and technology from Hunan Normal University, Changsha, China. He obtained his Master of Engineering on telecom engineering (awarded "Outstanding thesis of master degree" of Hunan Province, 2010) from Hunan University, Changsha, China. He is currently working towards his Ph.D. degree at Eindhoven University of Technology, Eindhoven, The Netherlands, supervised by Prof. Ton Koonen. Funded by NWO project "SOWICI", since April 2011, he worked on energy efficient access/indoor optical networks empowered by integrated optics, low-complexity digital signal processing, and flexible optical network design. In SOWICI, broadband optical mm-wave beam steering systems based on integrated photonic radio beamformers were built for hybrid fibre-wireless networks. Furthermore, the energy efficient and broadband operations in such networks are optimized by dedicated physical optical layer designs and implementation of advanced DSPs. These research activities produce a series of interesting scientific results.

Zizheng Cao has published 15 first-author peer-reviewed IEEE/OSA journal articles, including an invited paper in Journal of Lightwave Technology. He also has an invited talk about integrated optical radio beam steering systems in PIERS 2014. By March 2015, his research articles have been cited for 585 times, with H-index of 14 and 'i10' factor of 18 (source from google scholar). His research interests include modeling and design of integrated photonics circuits, microwave photonics, advanced DSP, and physical layer design of optical network. He is a student member of the IEEE Photonics Society. He serves as an active reviewer for many top journals, including Journal of Lightwave Technology, Photonics Technology Letters, Photonics Journal, Journal of Optical Communications and Networking, Optics Communications, Optics Express, and Optics Letters. He is one of the recipients of Graduate Student Fellowship of IEEE Photonics Society 2014. In 2014, he is ranked in the first place and is awarded a 16000.0 euro Lionix Integrated Photonics Design prize for a multi-project-wafer run. He holds two granted Chinese patents and one US provisional patent.